Multimaterial Multifunctional Fiber Devices

by

Fabien Sorin

B.Sc. Theoretical Physics
Ecole Polytechnique, Palaiseau, France, 2000
M.Sc. Theoretical Physics
Ecole Polytechnique, Palaiseau, France, 2002

SUBMITTED TO THE DEPARTMENT OF MATERIALS SCIENCE AND
ENGINEERING IN PARTIAL FULFILLMENT OF THE REQUIREMENTS FOR THE
DEGREE OF

DOCTOR OF PHILOSOPHY IN MATERIALS SCIENCE AND ENGINEERING
AT THE
MASSACHUSETTS INSTITUTE OF TECHNOLOGY
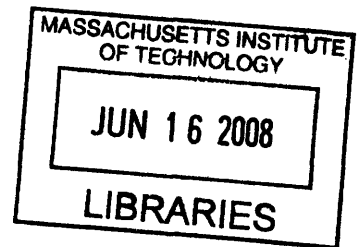
FEBRUARY 2008

Signature of Author:

Department of Materials Science and Engineering
October, 19, 2007

Certified by:

Yoel Fink
Associate Professor of Materials Science
Thesis Supervisor

Accepted by:

Sam Allen
Chair, Departmental Committee on Graduate Students

Multimaterial Multifunctional Fiber Devices

by

Fabien Sorin

ABSTRACT:

Optical fibers and semiconductor devices differ significantly in their properties and their processing approaches. The latter require an assembly of metal, insulator and semiconductor materials into complex geometries with small feature sizes (sub 100 nm), while maintaining high quality interfaces. Sophisticated logic and detection functions are realized through the integration of many such devices onto a chip. Conventional optical fibers have been restricted to insulating materials, much simpler cylindrically symmetric structures and larger feature sizes (order of a micrometer). Consequently a single fiber operates as a single optical transport device. Indeed the notion of integration has been foreign to optical fibers. Their processing however is much simpler compared to semiconductor devices as it utilizes a macroscopic perform to microscopic fiber fabrication approach. This process can efficiently yield highly uniform long and flexible fibers amenable to the formation of large area assemblies and woven fabrics. In this thesis, it is established that in-principle sophisticated semiconductor devices can be produced using simple preform-to-fiber thermal drawing techniques: In the first chapter a new materials processing paradigm is introduced where for the first time metals, insulators and semiconductors are thermally co-drawn in intimate contact and prescribed geometries. The second chapter focuses on unifunctional fiber devices and in particular the unique features of 1D distributed photodetecting fibers. The concept of fiber device integration is then established by demonstrating optic, electronic and optoelectronic functionalities within a single fiber. In a third chapter a model for understanding the influence of geometric and structural changes on the performance of fiber photodetectors is derived. It is demonstrated in particular that similarly to the evolution of semiconductor devices, the reduction of the materials feature dimensions inside the fiber significantly impacts the fiber performance characteristics. This in turn enables an increase in device density integrated into a single fiber. Unprecedented angular and spectral resolutions are achieved using this approach as described in chapter four. Finally, the first field effect is observed in a thermally drawn semiconductor metal insulator fiber. This paves the way to further integration of ever more complex electronic functionalities inside fiber devices.

Thesis Supervisor: Yoel Fink
Title: Thomas B. King Associate Professor of Materials Science

A mes parents, Ghislaine et Françis.

Acknowledgments

My deep thanks go first to my advisor Prof. Yoel Fink. Little would have been possible without his amazing guidance throughout my PhD program. His profound knowledge in diverse disciplines, his innovative thinking and his great ability to generate enthusiasm made my research work very exciting, rich and rewarding. I also would like to thank Prof. John Joannopoulos and Prof. Francesco Stellacci, my committee members, for their constant support and critical comments.

This work could not have been accomplished without the dedicated work of my research group. In particular I am grateful to Dr. Ayman Abouraddy from whom I learned a lot, especially in the art of writing scientific papers, and enjoyed fruitful discussions; Ofer Shapira whose help at different stages of my project was key; Dr. Mehmet Bayindir from who, in an unconventional way, I learned a great deal; Dursen Saygin-Hinczewski for her important help during numerous fiber drawings; Dr. Shandon D. Hart, Dr. Gilles Benoit and Dr. Ken Kuriki for their help to get me started in the lab; Nicholas Orf, Jeff Viens, Dr. Sylvain Danto and Zachary for their help in glass making and thermal evaporation. Matt Spencer for his great work on the integrated fiber devices grid. I would also like to thank the reminder of the group for their assistant and support: Sasha Stolyarov, Dr. Peter Rakich, Dr. Zheng Wang, Jerimy Arnold, Dr. Burak Temelkuran, Dana Shemuly, and Dr. Shunji Egusa. This research was greatly benefited from the collaboration with other research groups, in particular I would like to thank Prof. Thuller for letting me use his monochromator, Dr. Aimee Rose, Dr. Larry Takiff, and Kristin Mulherin from Nomadic, for providing the organic materials and their work in our joint project of Fiber-based explosive detectors. I would also like to acknowledge the support of DARPA, the ARO, the ONR, the AFOSR, the Center for Materials Science and Engineering (CMSE) and The Institute of Soldier Nanotechnology (ISN).

This period of time was joyful and pleasant thanks to many of my friends here in Cambridge and in France. Especially my longstanding frends Albert, Julien, Mac, Uriel and Mikael, Ofer, Sasha, Sylvain and the MIT group, the 110 Pleasant street crew, the MIT Aikido club especially Sensein Dick Stroud, Mike, Daryl, Sioux etc…

Contents

Introduction

Optical fibers, as conduits for optical communications, are used in a myriad of applications and configurations. They have also been used in sensing applications, although in configurations that do not include electrical currents and potentials except in external circuitry [1,2]. Part of the success of this technology relies on the attracting features of the fiber drawing technique. It is inexpensive, simpler than the elaborate wafer-based techniques used to produce planar semiconducting devices [3-5], and yields extended lengths of highly uniform fibers with well-controlled geometries and good optical transport characteristics [6]. However, this technique has been restricted so far to particular materials [7-9] and larger features [10-14]. In particular, the difficulty of integrating conducting materials inside fiber devices has precluded the incorporation of any electrical or electronic functionality in fibers. Indeed, the combination of conductors, semiconductors, and insulators in well-defined geometries and prescribed sizes, while forming intimate interfaces, is essential to the realization of practically all functional electronic and optoelectronic devices. In my thesis work, co-workers and I have developed a new material processing paradigm to combine materials with widely disparate electrical and optical properties into a single fiber, achieve sub-micrometer features and realize arbitrary geometries over extended fiber lengths. This provides us with a new opportunity to deliver novel semiconductor device functionalities at fiber-optic length scales, uniformity and cost. It also represents an alternative low-cost technique for producing large area woven structures of arbitrary size and geometry, made out of lightweight, flexible and yet mechanically tough devices, capable of complex functionalities such as sensing light, heat or chemicals. These findings can have a significant impact on fields like large area optic and optoelectronic systems, sensing technologies, functional fabrics and even clean energy.

Identifying materials with widely disparate optic and electronic properties while compatible for co-drawing is not a simple task. The first chapter of this thesis describes how we have been able to select and incorporate metallic elements into the fiber to be co-drawn with the insulating and semiconducting materials that composed the Photonic Bandgap fibers. In the second chapter we present the first Metal-Insulator-Semiconductor

(MIS) optoelectronic: one-dimensional (1D) distributed photodetectors. We demonstrate how we integrated optic, electronic and optoelectronic functionalities in a single fiber by surrounding the photoconducting core with a photonic bandgap mirror that enables the selection of the wavelength at which the device will operate. We also highlight the tremendous advantage of having a 1D distributed photodetector, by describing fiber assemblies for which the long length, light weight, and flexibility of the fibers are key. The third chapter focuses on a careful analysis of the photoconducting fiber devices and, in particular, how the device characteristics scale with the geometrical parameters of the fiber. This study will naturally lead us to consider how we can improve the performance using a thin-film structure instead of a solid-core as the active photoconductive element in the fiber device. One of the aspects of thin-film structures is their amenability to dense integration of further optoelectronic devices in the same fiber. Chapter four presents how with two thin-films structure integrated in a single fiber device, spectral as well as angular resolution can be achieved. Finally, Chapter five of this thesis highlights new results that represent the cornerstone of a new generation of fiber devices. The first field effect inside fiber constituents is demonstrated which paves the way toward multimaterial and multifunctional fiber devices with functionalities of increasing complexity.

I. Materials Selection and Fabrication

The emerging field of microstructured optical fibers relies on the controlled fabrication of sub-micron features in a fiber drawn in the viscous fluid state. While these fibers may be comprised of a single material combined with air holes [11,14], our strategy is to produce multi-material 'composite' fibers [15,16] consisting of materials having different optical and electrical properties [17-20]. The process of drawing fiber from a solid-structure preform that is heated and deformed in the viscous state has been well-established through the development of the fiber telecommunications industry, and enables the rapid fabrication of kilometer-scale continuous lengths of fiber with precise dimensional tolerances. However, we desire to employ unconventional materials and achieve much smaller feature sizes, and the general choice of this process creates significant constraints from the standpoint of materials compatibility. We first consider Photonic Bandgap fibers (PBG) whose role is to guide light and into which no metal is incorporated. Afterwards, the special case of fibers containing metal will be discussed.

I.1. PBG optical fibers

I.1.a. Materials selection

The main requirement for the fabrication of fibers that include cylindrical multilayer structures and that exhibit photonic bandgaps is the use of two materials having a high index-of-refraction contrast in order to enhance the photonic bandgap effects and minimize EM penetration depth [21]. However, only materials with very similar thermo-mechanical properties can be thermally drawn in a controlled and reliable way. The challenge is then to find materials with extremely different optical properties yet very similar thermo-mechanical properties. The main requirements in the materials used in these fibers are summarized below:

- The materials should be amorphous in nature, as well as 'glassy' (i.e., not easily crystallized at high processing temperatures), since the viscosity of a glassy

material varies quasi-continuously between the solid and liquid states, in contrast to a crystalline material. In general, materials should be glassy in order to be drawn at reasonable speeds in a furnace-tower process with self-maintaining structural regularity. Thus, our materials (or, at the very least, the majority component) must not simply be amorphous when deposited or made into a preform, but must remain amorphous and not crystallize when cycled through their softening and drawing temperatures.

- The selected materials should exhibit low optical absorption over a common wavelength band, such that the mirror penetration depth is smaller than the absorption length.
- The materials must be above their respective softening points at overlapping temperatures to enable fiber co-drawing.
- The materials should have compatible viscosities at the processing temperatures of interest.
- The materials should exhibit good adhesion/wetting in the viscous and solid states, without cracking, even when subjected to thermal quenching. It is generally understood that the degree of intimate contact between the two surfaces at the molecular scale is a crucial factor in increasing the short-range Van der Waals interactions that promote solid-state adhesion [22]. Thus, it is advantageous that both materials will be processed at a temperature at which they are both quasi-molten so that this molecular surface interpenetration may be enhanced.

Since glassy materials are desirable for efficient fiber drawing, our materials choices are restricted to the following categories: chalcogenide glasses, oxide glasses, halide glasses, and polymeric thermoplastics. Chalcogenides are high-index inorganic glasses that contain one or more of the chalcogen elements (sulfur, selenium, and tellurium) and generally contain no oxygen. Chalcogenide glasses have been explored in such applications as infrared lenses because of their transparency at longer wavelengths (up to 17 μm or longer). Chalcogenides have also been explored for usage in active optical devices due to their nonlinear optical properties and their ability to incorporate laser dopants into some compositions. They tend to have softening temperatures in a

range between 100-500°C and refractive indices between 2.2 and 3.5. Due to their high refractive index and infrared transparency, this is a particularly important class of materials in multilayer PBG fiber manufacture.

In selecting a low-index component as the second material for these PBG fibers, it is of principal concern to match the thermal properties of the chalcogenide glass. Oxide glasses, including high-purity silica (SiO_2), borosilicate glass, soda-lime-silicate (Na, Ca containing silicates) glasses, and phosphate and silicate laser glasses tend to be highly transparent from the visible regime to about 2.5 µm wavelength, are very resistant to chemical attack, and are easy to process. Unfortunately, for the purposes of drawing our multilayer PBG fibers, very few of these glasses are suitable since most of them have very high softening temperatures, making them incompatible with chalcogenide glasses in a thermal co-deformation process. Halide glasses are low-index (1.3 – 1.5) inorganic glasses that are based on halogen elements (most fluorine) but their compositions must often be complex in order to avoid crystallization (devitrification).

Thermoplastic polymers tend to have lower softening temperatures than typical chalcogenide glasses; however a few candidates have been identified with thermal properties that are in some ways comparable to chalcogenides. Disadvantages of polymeric materials that may need to be addressed include their thermal stability and optical absorption. Nevertheless, the wide variety of polymers available, the feasibility of processing them in film form, and their excellent mechanical toughness makes these materials our principal candidates for combination with chalcogenide glasses in composite PBG fibers.

Various high-index chalcogenide glasses and low-index polymers were identified as potential candidates based on their optical properties, overlapping thermal softening regimes, and their amenability to film processing. Adhesion and viscosity matching were then initially tested by thermal evaporation of a chalcogenide glass layer on top of a polymer film or rod and elongation of this composite laminate structure at elevated temperatures. Early attempts were unsuccessful because the various polymer substrates used had significantly lower extensional viscosities than the chalcogenide glasses, causing the glass film to break apart into small pieces during the drawing process. Ultimately, the choice of high-temperature polymers, such as poly(ether-sulfone) (PES)

and poly(ethyleneimine) (PEI), and simple chalcogenide glasses like arsenic triselenide (As_2Se_3) and arsenic trisulfide (As_2S_3), resulted in excellent thermal co-deformation without film-cracking or delaminating. These materials have a large difference in their refractive indices and overlapping transparency windows, verified through spectroscopic ellipsometry measurements. An additional advantage in choosing As_2Se_3 for this application is that not only is it a stable glass, but it is a stoichiometric compound that can be readily deposited in thin films through thermal evaporation or sputtering, without dissociation [23].

I.1.b.   Preform preparation and composite-fiber drawing

We now discuss the fabrication of the structured preform consisting of multiple, thick, alternating layers of our selected materials (a chalcogenide glass and an organic polymer) in intimate contact with each other. Thus, we desire to arrange the films in a multilayer cylindrical geometry with high uniformity, at a high deposition speed. The thin-film deposition technique that we chose was thermal evaporation of the chalcogenide glass onto free-standing, commercially-obtained polymer films, allowing us to deposit layers of the chalcogenide glass at high deposition rates. The chalcogenide-coated PES film can then be 'rolled' into a cylindrical multilayer structure, potentially forming many layers via a single deposition step. The large-area coated film can be wrapped on top of a PES rod by hand, and a mirror structure with twenty or more layers is fabricated necessitating only one or two vapor deposition steps. To create a hollow fiber, the coated film is wrapped around a hollow silicate glass tube and consolidated through heating in a vacuum oven at 255-265 C. The silicate tube is then removed from the preform core by etching with hydrofluoric acid. The resulting fiber preform is then drawn into extended lengths of fiber in a furnace set to ~280-300 C, using the tower draw procedure utilized in the fiber-optic industry. During the draw process, the mirror layers are reduced in thickness by a factor of ~20-100 so that the PBG of the final mirrored product is located in the near-to-mid-IR. The nominal positions of the PBGs are determined by laser monitoring of the fiber outer diameter (OD) during the draw process.
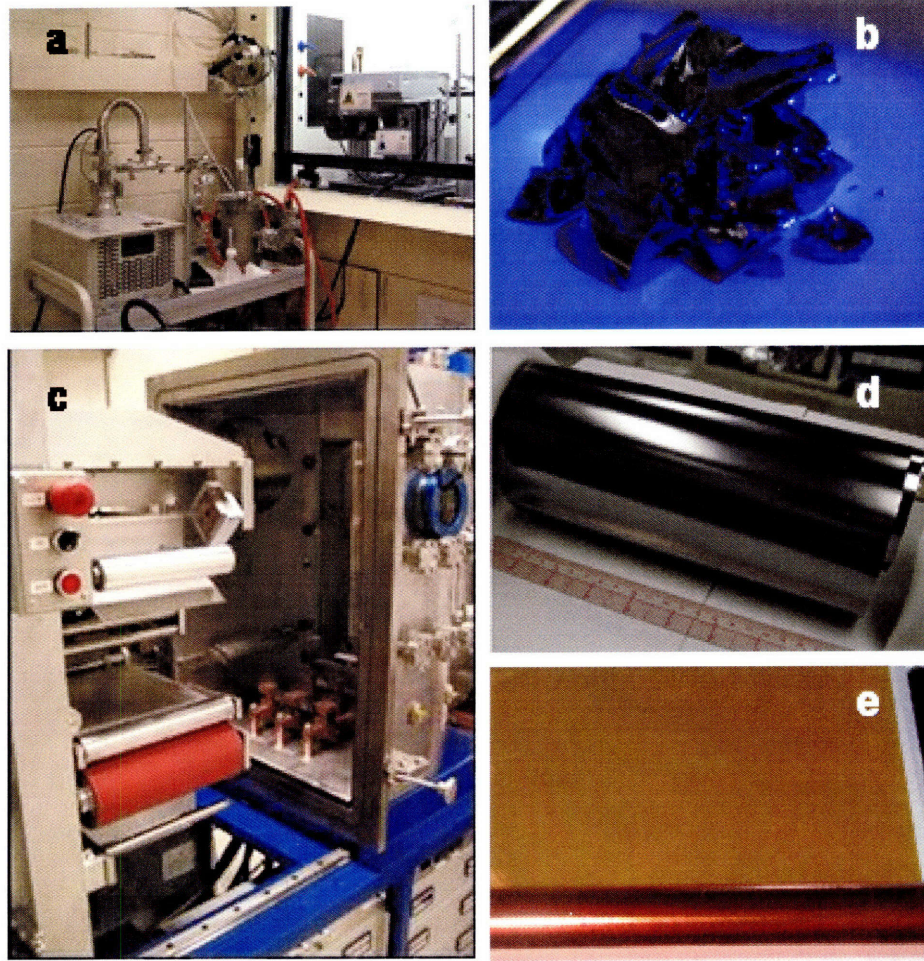
Figure I-1. (a) Glass fabrication apparatus. (b) Example of a chalcogenide glass (As2Se3). (c) Thin-film evaporation system. (d) As2Se3 on PES, and (e) As2S3 on PES.

Figure I-1 and Figure I-2 show some of the processing equipment used in preform fabrication and fiber drawing. The process starts with chalcogenide glass synthesis using standard sealed-ampoule techniques [23,24,25], beginning with pure elements placed in a fused quartz ampoule in a nitrogen atmosphere. The sealed ampoule is then heated in a "rocking furnace" that physically mixes the elements according to a prescribed heating schedule, at the end of which the ampoule is quenched in air or water. The chalcogenide glass synthesis line and rocking furnace are shown in Figure I-1(a), while a sample of As_2Se_3 glass produced is shown in Figure I-1(b). Once the glass is synthesized, it is no longer sensitive to oxygen at room temperature and may thus be easily transported to a thermal evaporation system for film deposition. In the past we have used a basic Ladd
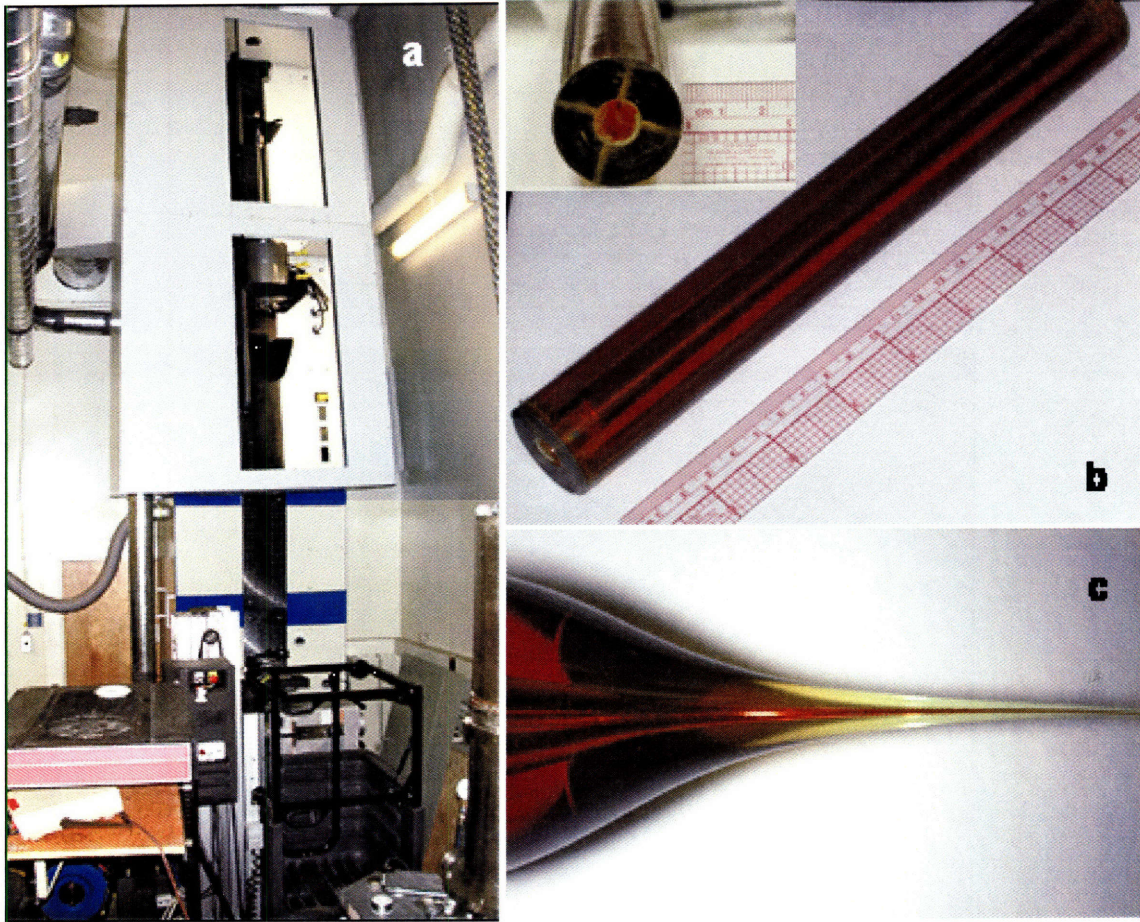
Figure I-2. (a) Optical fiber thermal draw tower. (b) Preform after consolidation (inset shows a cross section of the preform). (c) Photograph of the neck-down region of a fiber preform after drawing

vacuum evaporator (Ladd Research Industries model 30000), but now rely on a more complex thermal evaporation system (Systems Design and Fabrication, Inc.) intended specifically for the coating of large-area polymer films with chalcogenides. This system consists of a feed roll of polymer film, two deposition areas designed to coat both sides of the film, and a take-up roll designed to wrap up the coated polymer, and is shown in Figure I-1(c). Two examples of chalcogenide-coated polymers thin films are shown in Figure I-1(d) (As_2Se_3 on PES) and Figure I-1(e) (As_2S_3 on PEI).

The draw tower, shown in Figure I-2(a), consists of a motorized down-feed mechanism that lowers the preform into the furnace and a motorized capstan that draws the fiber at a controlled rate. This combination of controlled down-feed speed and controlled capstan drawing speed determine the fiber diameter according to mass flux conservation (assuming that the density remains constant). The diameter of the fiber is

monitored using laser diameter monitors (Beta LaserMike) directly below the furnace, as well as at the base of the tower near the final collection point. The drawing line of the fiber also includes a three-wheel fiber tension measuring device (Tension Measurement Inc. model SM9640P). The diameter monitoring system can be set into a feedback loop so that the monitors control the capstan draw speed based on a preset diameter and a control algorithm. If the preform is well-consolidated, the trapped gases between the rolled polymer layers are removed, causing the PES layers to transform from a reflective, silvery state to a transparent amber, as shown in Figure I-2 (b). The neck-down region of the preform after drawing is shown in Figure I-2 (c).

The end result of this fabrication process is 10's to 100's of meters of uniform and flexible fiber as shown in Figure I-3(a). A scanning electron microscope (SEM) micrograph of a fiber having a fundamental PBG in the visible (Figure I-3 (b)) as well as PBG structures of layers with different thicknesses is shown in Figure I-3 demonstrating the excellent uniformity of the multilayer structure. Figure I-3 (e) shows the transmission spectra of fibers of different bandgap, illustrating the scalability of this technique where smaller feature sizes enable the transmission of smaller wavelengths.

I.2. Metal-insulator-semiconductor optoelectronic fibers

The fabrication approach that we adopt for metal-containing fibers is extremely similar to what have just been presented, as it also relies on first preparing a large-scale macroscopic version of the required device in the form of a 'preform' that is then reduced to the desired size through the process of thermal drawing as described in Figure I-4. This process obviously places constraints on the metals that may be utilized, in addition to those already described for the other components. Nevertheless, a set of materials with widely disparate electrical, optical, and thermal properties have been identified and successfully incorporated into fiber-based devices [17-20].
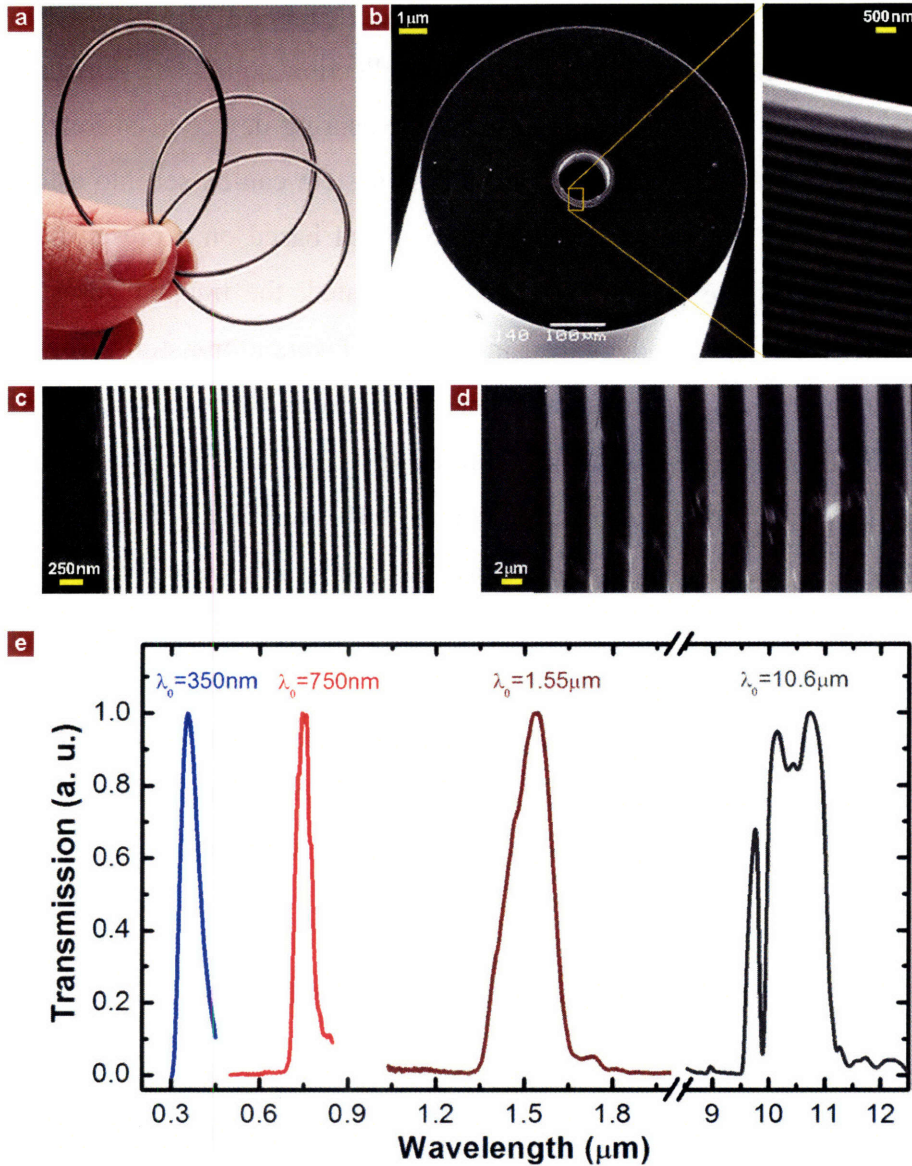
Figure I-3. (a) Flexible PBG fiber. (b) SEM micrograph of a PBG fiber with magnification of the PBG structure region. (c) and (d) SEM micrographs of PBG structures of layers with different thicknesses. (e) transmission spectra for PBG fibers with different bandgaps

I.2.a.   Materials selection

The fundamental idea that enabled the controlled incorporation of metal into optical fibers was to violate the first rule of selection for materials described in the previous section: the metallic component is not amorphous, but flows during the draw process as the melt of a crystalline material. The main criterion of selection is then that the melting temperature is low enough so that the metallic electrode melts at the

temperature of drawing. For the Chalcogenide glasses and the high temperature thermoplastics, the same criteria of selection apply. Different metallic materials, alloys or eutectics can then be identified, such as Sn (T_M = 232 °C), Sn(96%)-Ag(4%) (T_M = 221-229 °C) or Pb(38%)-Sn(62%) (T_M = 183 °C).

Depending on the application, other physical properties of the metals can be part of the selection process, such as the work function or the formation of a Schottky junction with a particular glass. Avoiding compound formation between the molten metal and the soft glass during the drawing process is also essential. In early attempts, indium was found to interact with the arsenic of As_2Se_3 to form the InAs semiconductor. This crystalline compound crystallizes and is an obstacle for a successful draw and so should be avoided.

Other types of conducting materials can be considered. Progress is being made in the processing of amorphous metals with thermal properties that come close to being compatible with our simple and inexpensive fiber fabrication technique [26,27]. Similarly, conducting polymers are a class of amorphous materials that attract much interest and that may have strong potential for use in fibers. Amorphous conducting materials would enable better control during the draw process an access to smaller feature sizes and a larger variety of geometries for the metallic like element in the fiber. The use of these materials is not addressed in this thesis but constitutes an intriguing direction of research for further development of optoelectronic fiber technology.

It is important to note that polymers and glasses can be engineered to change their drawing temperatures and adapt them to particular metallic elements required in the fiber device.

I.2.b.   Preform preparation and composite-fiber drawing

The desired shape and position of the metallic elements integrated in a fiber-based device will depend on its final application. Nevertheless, some general rules apply to the production of all metal-containing fiber preforms; therefore, a technique differing from that described earlier has been developed. Our first approach to introduce metallic elements was to evaporate thin layers of indium or tin on PES sheets, in the same manner that glasses were evaporated to form the PBG structure described above. This technique
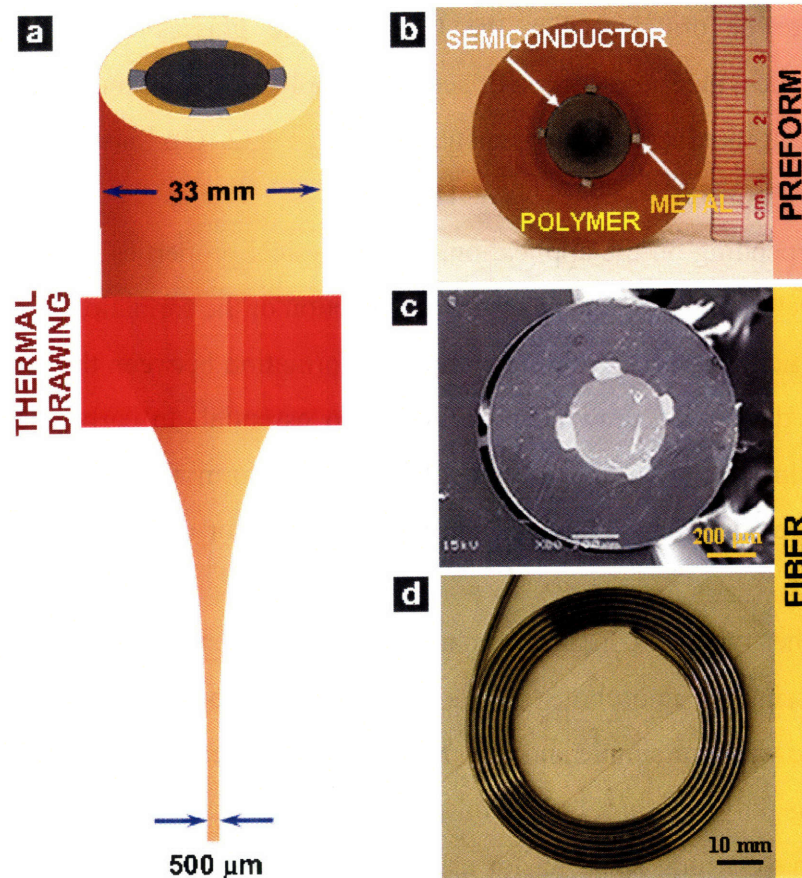
Figure I-4. A new fabrication technique by fiber drawing. (a) A macroscopic preform containing metallic, semiconducting, and insulating elements drawn thermally to kilometer-long functional devices. (b) A preform consisting of a photoconductive core made of a chalcogenide glass (As-Se-Te-Sn), surrounded by a polymer (PES) cladding. The core is contacted by four metal (Sn) electrodes that run along the length of the preform. (c) An SEM micrograph of the fiber cross section demonstrating that the preform geometry has been preserved during the drawing process. (d) Image of 1-meter long fiber. The bright region along the fiber is one of the metallic electrodes. Owing to the thick polymer cladding, the fiber is flexible and tough.

proved to be very challenging for one simple reason: the viscosity of metallic elements being very low as they melt, the capillary break-ups are drastically facilitated, which resulted in a breakdown of the metallic layer as can be seen in Figure I-5. Replacing the thin layer by a bulk metallic ring helped but here again, the liquid will try to lower its surface energy by converging into single or multiple cylinders. The great stress associated with these capillary break-ups can deform the polymer, as is apparent in Figure I-7. Thus, the drawing of a metallic layer or ring is a challenging task and alternative electrode shapes had to be investigated.
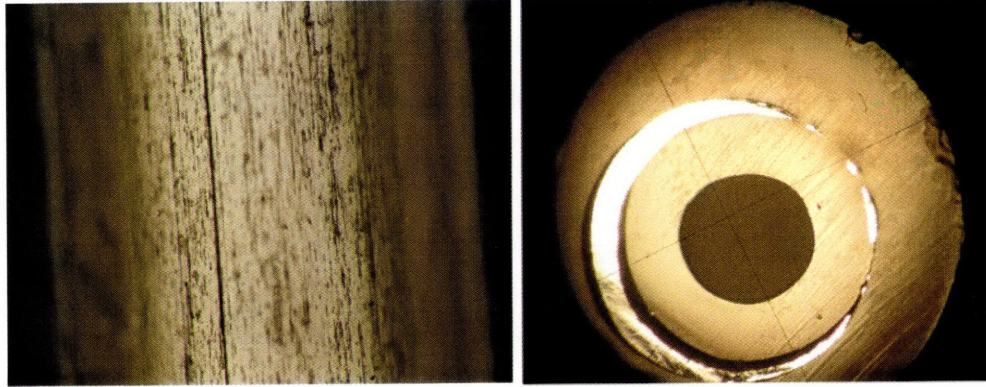
Figure I-5. (Left) Picture of the side of a fiber with a thin-film indium layer that broke up into thin cylinders and drops during the draw process. (Right) Cross section picture of a polymer fiber with a ring metallic electrode. Here again, in an effort to lower its surface energy the liquid metal tends to form a cylinder rather than a ring (see text).

Metallic electrodes with a rectangular shape have several advantages: they have limited surface area so the capillary break-up is reduced and can be compensated for if proper tension is applied to the fiber during the drawing process. They enable a good contact between the metal and the semiconducting glass, and are simple to prepare and to roll into the preform. They also minimally perturb the heat distribution in the preform during the draw process. All of the fiber devices presented in this thesis contain electrodes with this particular geometry. The overall fabrication procedure can then be appreciated by considering the example of a preform with a chalcogenide-glass rod core contacted by four metallic electrodes and encapsulated in a polymer cladding, as shown in Figure I-6. Also shown is the fabrication of thin-film fibers (presented in a later section). The fabrication process begins with the preparation of a polymer tube with an inner diameter exactly matching the outer diameter of the glass rod, and a thickness equal to that of the metallic electrodes. Next, pieces of the polymer tube, with the same shape as the electrodes, are cut out, and the glass rod is then slid into the tube. After cleaning the electrodes by scratching away the outside oxide layer and washing them with flux, we place the electrodes into the prepared openings. A protective polymer cladding is then wrapped around the structure. In this way, the metal electrodes are completely enclosed between the polymer and the glass rod, preventing leaks when it melts during drawing. The principal challenge here is to prepare the preform in such a way as to encapsulate the metal as hermetically as possible, so as to prevent it from flowing out when it melts and to retain the cross-sectional geometry of the preform inside the resulting fiber. The
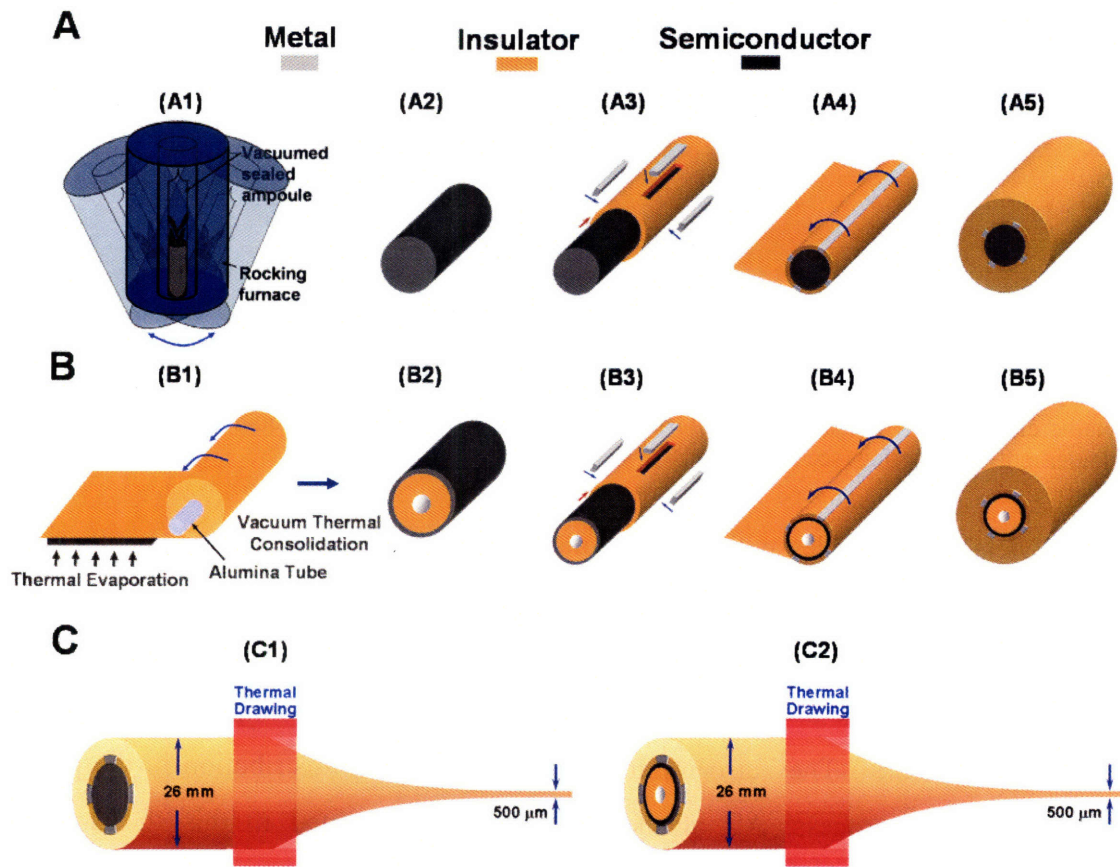
Figure I-6. Fabrication steps for producing solid-core and thin-film fiber devices from a macroscopic preform. (a). Producing a solid-core fiber device. A chalcogenide rod (a2) is slid into a polymer tube where rectangular spaces have been cut to place the Sn electrodes (a3). The structure is then encapsulated in a polymer cladding (a4) and consolidated to obtain a macroscopic preform (a5) (see text). (b) Producing a thin-film fiber device. Chalcogenide glass is thermally evaporated on a polymer sheet (b1) that is rolled and consolidated to obtain a polymer tube with an outer layer of controlled thickness of glass (b2). The structure is then encapsulated in a polymer cladding (b4) and consolidated to obtain a macroscopic preform (b5) (see text). (c) Thermal drawing of macroscopic preforms yields the mesocopic solid-core and thin-film fiber devices (see text).

preform is then consolidated under vacuum conditions at a high temperature (typically $260C^{\circ}$ and 10^{-3} Torr).

The conditions required for the successful thermal drawing of a preform containing metallic elements are quite different from those for the optical fibers described earlier, which contain only polymers and glasses. First, the rectangular metal electrodes also have a tendency to break up into cylinders, and by doing so apply a local stress on the surrounding polymer. Drawing at a low tension results in the polymer deforming

accordingly, and the designed preform structure is lost as can be seen in Figure I-7. Here, different failures such as capillary break-up of the electrode, electrodes deforming the polymer or even disappearing, are a result of low tension.
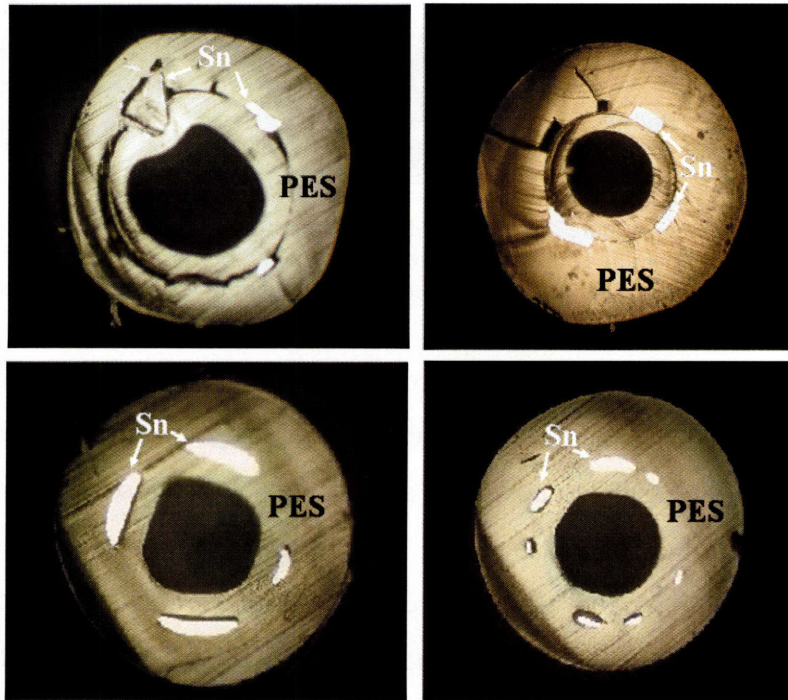
Figure I-7. Four examples of failures that can occur during the processing of rectangular metallic electrodes inside a polymer-based fiber device.

Second, the required drawing temperatures tend to be higher when metals are included, due to the altered temperature distribution in the preform created by the presence of the metal. Since metals are good heat conductors, when the preform is heated up in a furnace, the electrodes drive the heat to the top of the preform away from the center of the furnace, thus effectively acting as a heat 'shield'. In Figure I-8, we show simulations of the temperature distribution of the preform cross section in the middle zone inside the furnace. Three cases are considered: a polymer fiber without metal, a metallic ring placed close to the core, and a metallic ring close to the surface of the preform. It is apparent in Figure I-8 that the metal far from the center of the preform acts as a heat shield, reducing the temperature of the preform. A higher temperature is therefore required to draw the preform. Raising the temperature too high, however, affects the other key parameter we discussed earlier, namely the fiber tension.
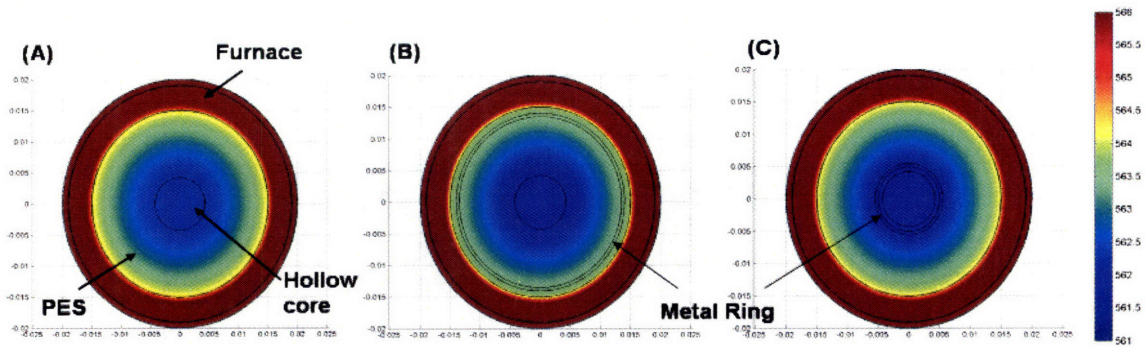
Figure I-8. Study of the temperature distribution of a preform cross section inside the draw tower furnace. (a) No metallic ring. (b) Metallic ring close to the outside of the preform. (c) Metallic ring close to the center of the preform. A colder fiber is obtained when the metallic ring is on the outside of the preform.

Here again, the rectangular electrode has a significant advantage over its ring counterparts, as it reduces the heat shield effect. Moreover, placing the metallic elements close to the fiber core results in a twofold advantage: (1) the closer they are placed to the center, the less of a heat shield they will be for the rest of the preform, as apparent in Figure I-8, and the large radial temperature gradient, deleterious for a successful draw, is lowered; and (2) less stress will be generated in the fiber since the metal flows down the neck at a small angle when closer to the preform center. The fiber is consequently less likely to break up during the drawing process.

To summarize, when rectangular electrodes are properly encapsulated and drawing parameters such as the temperature, drawing, and down-feed speeds are set such that a high tension is maintained throughout the drawing process, metallic elements can be successfully integrated inside a fiber device. A cross section of the preform used to produce a fiber device is shown in Figure I-4(c), and is seen to contain metallic, semiconducting, and insulating materials combined in intimate contact and in prescribed geometry. One can easily observe that the geometry of the preform has been well-preserved after size reduction (Figure I-4(b)). It is important to note that the device demonstrates little functionality at the length scale of the preform, but that at the length scale of the fiber, the device becomes functional, and the result is kilometer-long functional fiber devices (Figure I-4(d)). In fact, it is conceivable that all of the basic components of modern electric and optoelectronic devices (such as junctions and

transistors) could potentially be incorporated into fiber-based devices, using this simple, low-cost technique, at a length scale out of the reach of traditional electronics.

We explained in this first section our simple and inexpensive thermal drawing approach to producing fibers containing materials with disparate optical and electrical properties. We now turn to the first optoelectronic fiber device we fabricated using this novel technique.

II. One-dimensional (1D) distributed photodetecting fiber devices

The first device built using the novel drawing technique described above was a 1D distributed photodetecting fiber [17,18]. After describing the basic principle of this new device, we will show how a higher level of integration can be achieved by incorporation of a PBG mirror structure that enables the selection of the wavelength at which the device will operate. We will then focus on how this seemingly trivial change in dimension leads to far-reaching consequences. Specifically, fiber assemblies with unprecedented properties will be presented and a lensless imaging system will be described.

II.1. A 1D distributed photoconductor

A well-known characteristic of crystalline semiconductors is the change of their electrical conductivity under optical illumination due to the transition of electrons from the valence band to the conduction band through the absorption of photons having sufficient energy. Although the lack of long-range order in amorphous media, such as chalcogenide glasses, renders the Bloch theorem (and thus the crystal momentum k), irrelevant, the energy-band diagram is still a useful conceptual tool that may be used as an approximation to describe the density of electronic states. Amorphous materials possess an energy bandgap between the valence and the conduction bands, but in contrast to intrinsic crystalline semiconductors, the density of states is not zero in the gap [28]. Indeed, the random electronic potential in any amorphous structure is responsible for an exponentially decaying density of states that extends out of the conduction and valence bands into the bandgap, called Urbach's tail, corresponding to localized states below the mobility edge. Moreover, defect states, such as dangling bonds, that can be present at energies generally corresponding to the center of the gap, are responsible for the characteristic properties of chalcogenide glasses such as p-type conductivity and the pinning of the Fermi level [29].

(A) **(B)** **(C)**
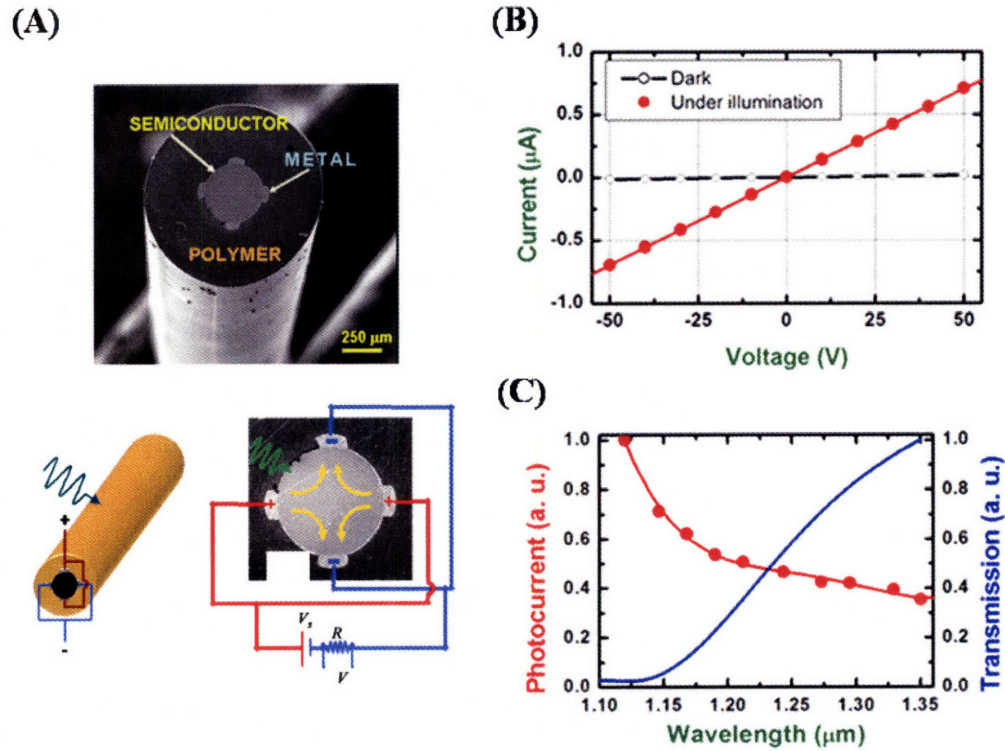
Figure II-1. Metal-semiconductor-metal (MSM) fiber photodetectors. (a) A MSM fiber SEM micrograph and schematics that show the device connected to an external circuitry through four metallic electrodes running all along the fiber length. (b) Measured current-voltage characteristics of the MSM fiber photodetector in the dark and under illumination (c) Measured photocurrent sweeping wavelength of tunable OPO while keeping the optical power constant. Blue curve is corresponding to transmission through bulk Sn-doped AST chalcogenide glass.

When light impinges on an amorphous semiconductor, such as that in the fiber core described above, holes from the valence band, as well as from localized states inside the bandgap, can gain sufficient energy by absorption of a photon in transit to an extended state in the conduction band, a process not dissimilar from what occurs in the case of the crystalline compound. It is interesting to note, however, that there is no sharp energy edge for excitation of electron-hole pairs in amorphous semiconductors, due to the non-zero density of states in the gap. These materials are therefore sensitive to light over a wide range of wavelengths, and are also suitable for sub-bandgap detection, which has important consequences for our fiber-based photodetectors. Returning to the above described fiber device, when the metal electrodes are connected to an external circuit and a voltage is applied, as can be seen on the schematic of Figure II-1(a), a current determined by the conductivity of the glass in the dark will flow. The fiber undergoes a

change in electrical conductivity when externally illuminated since electron-hole pairs are created, driven apart by the electric field, that contribute to the current flowing through the fiber.

In order to confirm the fidelity of the metal-semiconductor contact and characterize its photoconductive properties, we first measured the current-voltage (I-V) curve of the device with the metal electrodes connected to an external circuit as shown in Figure II-1(a). The measured I-V curves in the dark and while the fiber is externally illuminated are plotted in Figure II-1(b), revealing clear ohmic response in both cases. Next, we characterized the broad-band photoconductive response of the device fiber (the red curve in Figure II-1(c). A 50-volt DC voltage was applied to the fiber and the current was measured using a pico-ampere meter (Yokogawa/Hewlett Packard 4140B). The fiber is illuminated externally with a laser beam from a tunable, synchronously pumped optical parametric oscillator (Mira OPO, Coherent). The optical transmission of a bulk AST-Sn glass sample (12-mm diameter and 5-mm length) was obtained via an FTIR measurement (blue curve in Figure II-1(c)). The spectral photoconductive response is commensurate with the optical transmission measurement. Note that changing the chemical composition of the glass core can change the spectral characteristics of the photoconductive response.

In the next section, we show how integrating an optical filter inside the fiber device allows us to modulate and control this spectral response without interfering with the glass composition.

II.2. Integrated spectroscopic optoelectronic fibers

We have worked thus far with photoconducting fibers having a simple geometry that can detect light from any direction at any point along its entire length. In this section, we go a step further into the integration of different functionalities into optoelectronic fiber devices by showing the ability to select at what wavelength the device will be operational. We presented in the first section how materials were selected and how optical fibers were drawn. We also showed that constructing fibers with metallic elements required very similar materials and fabrication techniques. Since both types of
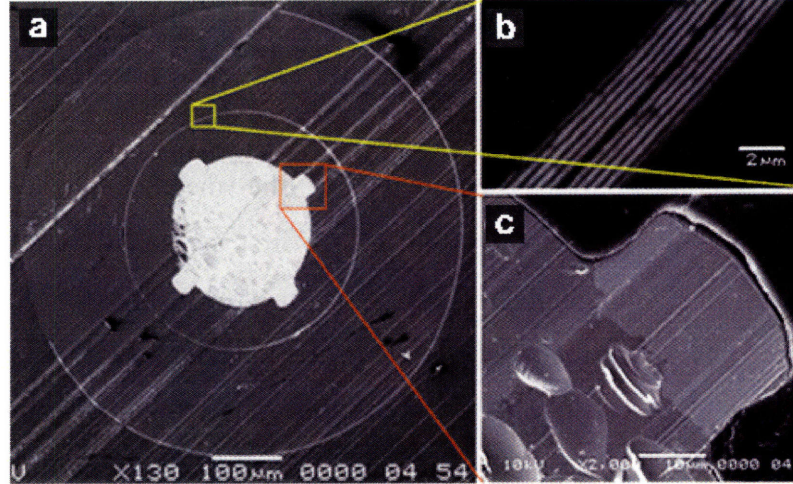
Figure II-2. Integrated optoelectronic device fiber. (a) SEM micrograph of the entire cross section of a 650-μm thick device fiber with 200-μm chalcogenide glass core surrounded by a PES cladding. The core region is surrounded by a resonant cavity structure. The bright regions on the polymer-glass interface are the Sn metal electrodes, which are continuous along the whole fiber length. (b) A magnified micrograph showing the resonant optical cavity structure. (c) A magnified micrograph demonstrating the excellent quality of the semiconductor-metal interface.

fibers were produced using the same set of materials and fabrication techniques, it is natural to attempt combining both functionalities into a single *hybrid* fiber.

The device that we present here is a narrowband, tunable optical detector based on the design shown on Figure II-2. The fiber core is a photoconductive chalcogenide glass cylinder, contacted with metal electrodes, that produces a change in current upon external illumination under suitable bias conditions. A single- (radial) mode cylindrical-shell optical cavity is introduced in the optical path, shielding the photoconducting core from ambient illumination sources. Upon *external* illumination, when the wavelength of the radiation matches that of the cavity resonance, we observe an electric response from the fiber core thus establishing the *spectroscopic* functionality of the fiber.

Introducing a defect into a 1D photonic crystal can result in resonant tunnelling at a frequency inside the PBG. Figure II-3 shows one such example for a finite structure consisting of 16 alternating layers of indices 2.82 and 1.62, thicknesses $0.365a$ and $0.635a$, with a defect in the middle having an index of 2.82 and thickness of $0.73a$, where a is the multilayer period. The photonic band structure is essentially similar to that of an infinite 1D photonic crystal except for the appearance of a cavity mode (thin blue line) inside the PBG region where photonic states are normally not allowed. The reflectivity at

$k = 0$ (normal incidence to the structure) is also shown, revealing that a frequency near the center of the stop has zero reflectivity, and thus tunnels past the 1D multilayer structure.

The preform of this spectroscopic fiber consists of an $As_{40}Se_{50}Te_{10}Sn_5$ (AST-Sn) rod, having a diameter of 12 mm and a length of 18 cm, contacted by four Sn conduits, and surrounded by a quarter-wave As_2Se_3/PEI multilayer mirror structure with a $\lambda/2$ PEI cavity and a protective PES cladding. The multilayer structure in the three fibers consists of three bilayers, As_2Se_3 and PEI, a $\lambda/2$ PEI cavity, followed by three more bilayers. The preform (20 mm in diameter and 30 cm in length) was consolidated in a three-zone horizontal tube furnace while being rotated along its axis. Subsequently, the preform was drawn in a three-zone vertical tube furnace at a top zone temperature between 185 and $230^{\circ}C$ and a middle zone temperature $295^{\circ}C$ with a tension of 500 grams. A capstan speed of about 0.7-3 m/min produces a fiber of a diameter between 1200 μm and 500 μm and a length of several hundred meters. Figure II-3(a) shows SEM micrographs of the spectroscopic fiber cross section. An enlargement of the resonant cavity structure is shown in Figure II-3(b), while an enlargement of the metal-semiconductor interface demonstrating the intimate contact is shown in Figure II-3(c).
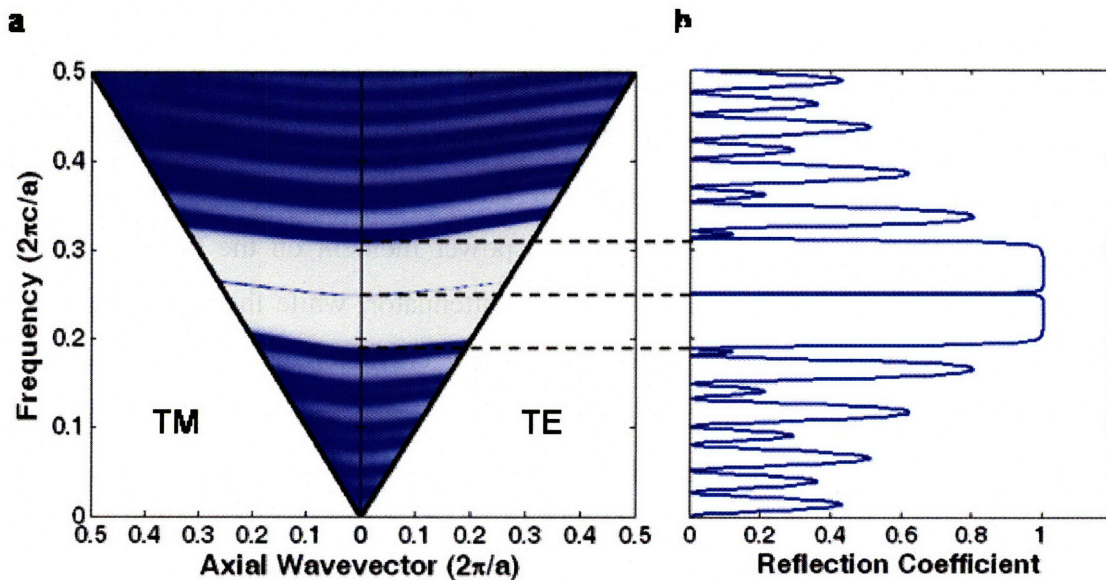
Figure II-3. Band diagram of a finite 1D photonic crystal structure consisting of alternating N layers of materials having indices of and thicknesses. The 1D structure contains a defect of thickness and index. Blue areas correspond to allows states while white corresponds to forbidden states. The right panel shows the reflectivity along the $k = 0$ line in the band diagram, corresponding to normal incidence in the structure.

The resonance wavelength and photonic bandgap are both determined by the outer diameter of the fiber. From the collection of fabricated fibers, we selected three with a wide range of diameters (and, therefore, a wide range of resonant wavelengths), of 870, 890, and 920 μm, which have calculated resonance wavelengths of 1.26, 1.29, and 1.33 μm, respectively. For the 920-μm fiber, for example, the thicknesses of As_2Se_3 and PEI layers are 117 and 204 nm, respectively. The reflectivity of the optical-cavity structure was measured for single fibers having these diameters with an FTIR spectrometer (Nicolet/SpectraTech NicPlan infrared microscope and Fourier transform infrared spectrometer [Magna 860]), and are displayed in Figure II-4(a). The FTIR spectra agree well with the calculated spectra when averaging over the range of angles admitted by the microscope objective (0 to 35°, numerical aperture of 0.58) is taken into consideration, leading to a reduction in the apparent quality factor of the cavity mode.

In order to characterize the optoelectronic response of our integrated device fiber, it is useful to measure both the electrical photocurrent and the optical reflectivity simultaneously. This can be achieved by externally illuminating the three aforementioned fibers with an OPO laser beam and measuring the back-reflected light though a beam splitter, while simultaneously monitoring the generated photocurrent in the photosensitive core. For optical characterization, we used a Verdi10 (Coherent) to pump a Ti-S femtosecond laser (Mira 900, Coherent) that was then down-converted using a synchronously pumped OPO (Mira OPO, Coherent). The OPO beam was focused onto the outer surface of the fiber using a ×5 microscope objective (NA=0.1), and the back-reflected light from the fiber was directed through a beam splitter to an InGaAs photodetector (Newport 818-IG). The optical power incident on the fiber surface was maintained at 30 mW, using a variable optical attenuator, while the wavelength of the laser beam was swept. For simultaneous electrical characterization, we measured the current flowing through the fiber electrodes using a pico-ampere meter (Yokogawa / Hewlett Packard 4140B). The DC voltage difference applied to the two fiber electrodes was 50 volts. At each wavelength, the incident optical power was adjusted, the electrical current was recorded, and the back-reflected light power measured.
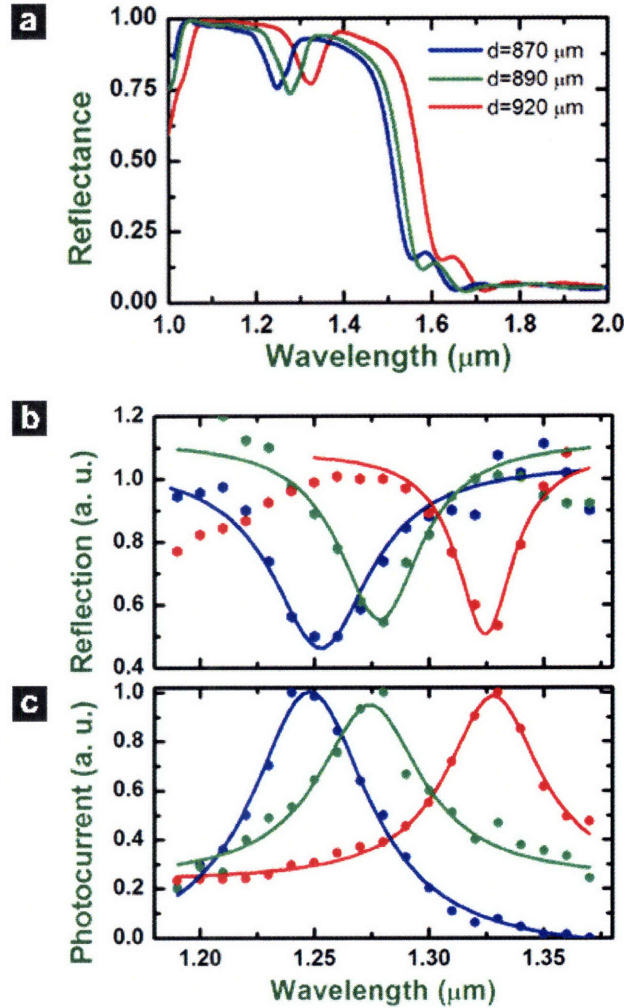
Figure II-4. Spectrometric fibers. (a) Broad-band FTIR spectra of device fibers with 870, 890, and 920-μm outer diameters. (b) Measured back-reflected light power from the same three device fibers when illuminated with a tunable OPO laser beam. (c) Simultaneously measured photocurrents through the device fibers.

In Figure II-4(a) and (b), we display the measurement results of the back-reflected light from the three different fibers as the wavelength of the laser beam is swept. Concurrently, in Figure II-4(c) we plot the results of photocurrent measurements of these fibers. At the resonance wavelength, the back-reflection is diminished, and the light reaches the photoconductive core. Consequently, the corresponding photocurrent is enhanced. This integrated optoelectronic fiber functions as a narrowband photodetector, with the detected wavelength tuned through the fiber outer diameter.

The striking originality of this new type of light-sensing device, besides its low cost and simplicity of production, resides in its geometry. It is the first one-dimensional

distributed photodetector that detects light incident on it from any direction at any point along its entire length, which may extend to hundred of meters. In the next section we show how we can take advantage of this original feature by building fiber assemblies.

II.3. Two- and three-dimensional fiber assemblies

II.3.a. Fiber grids and spheres

The 1D distributed nature of the new fiber devices presented so far has an inherent advantage compared to its 0D photodetecting device counterpart. Producing a photodetecting line with current point photodetectors (of dimensionality 0) would require a large number of devices, and the price of their assembly would scale with the detection length required. An inherent disadvantage of a distributed 1D photodetector such as our fiber, however, is that no information about the location of the incident beam along the fiber is obtained. This may be overcome by constructing two-dimensional (2D) assemblies of fibers to localize a point of illumination in a plane. One striking advantage of the 1D nature of this new type of device is revealed when one realizes that a desired resolution of $N \times N$ pixels per unit area would require N^2 point (dimensionality zero) detection elements. A fabric woven out of linear 1D fibers, on the other hand, provides a grid structure which in turn can be used to localize an illumination point on a surface, but with detection elements of only order N. Moreover, by overlapping layers of this fabric, one could even ascertain the direction of incoming illumination.

To demonstrate this capability, we arranged the photo-sensitive fibers on a square grid we call a 'fiber web'. Low-density fiber webs are typically transparent as can be seen in Figure II-5(a). The fiber is first drawn in long lengths, typically extending over tens of meters, and is then cut into smaller pieces. The electrical contacts for each fiber piece are established individually and the electrical contacts for the fiber are then connected to an external electronic circuit. The flexibility of these fibers allows them to be woven into a 2D web. The intersection points of the horizontal and vertical fibers represent points at which a beam location may be determined, as a traditional optical point detector would do. However, the use of fiber webs enables this to be achieved on an unprecedented area scale compared to traditional optical arrays. A photograph of such a web contacted to
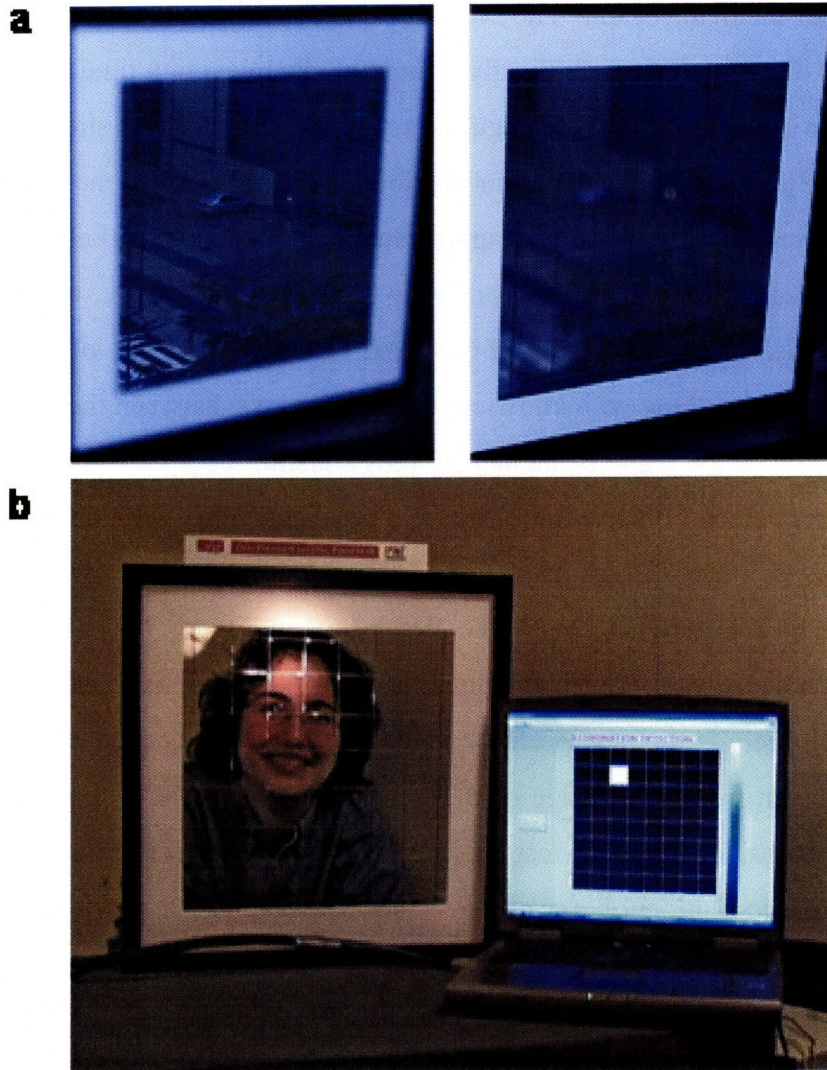
Figure II-5. (a) A transparent 2D fiber web. (b) A 2D fiber web used to track a point of illumination in real time.

appropriate circuitry is shown in Figure II-5 (a). This web is made of 16 photodetecting fiber elements arranged into an 8×8 square grid which extends over a clear area of 30×30 cm^2. Denser arrays can be built and yet be transparent as shown in Figure II-6(a). When light is incident on any of the fibers, a photocurrent is generated which is monitored by a PC. When no light is incident on the web, the electrical signals obtained from the fibers assume their 'dark' values. The program creates a 'virtual grid' that is displayed on a computer screen (Figure II-5 (b)), and in this case will be uniformly black. The horizontal (vertical) fiber that undergoes the maximum change determines the vertical (horizontal)

coordinate of the incident beam. The voltage drops on the fibers are monitored continuously, and the refresh rate is typically limited by the relaxation time of the fibers.

Dr. Ayman Abouraddy and colleagues have made an extensive study on 2D and 3D fiber meshes [30]. He demonstrated that the localization as well as the direction of a light beam can be reconstructed with the appropriate use of such constructs. Since these sparse arrays are essentially transparent, one may arrange, for example, two planar 2D arrays in cascade as shown in Figure II-6(b) and the determination of the point of incidence on both arrays (along with knowledge of the distance between the webs) allows for the determination of the angle of incidence, thus constituting a vector beam detector. Although an optical detector obstructs the path of a ray since light detection is, in general, a destructive process, nevertheless, an optical array made sufficiently sparse will offer little disturbance to the incident field. The first array in Figure II-6(b) registers the location of the incident beam, which continues its path, only slightly perturbed, to the second web which records the new position of the beam. One may then easily compute the angle of the beam from knowledge of the two locations and the distance d between the planes of the webs. The angular resolution of this arrangement is determined by the ratio of the spatial resolution of a web to d, and the angular bandwidth (numerical aperture) is limited by the ratio of the size of the array to d.

As is the case with any detection system, the finite size of the above-described planar fiber webs, however, limits the numerical aperture for light detection. For example, when detecting the direction of a beam of light, a light ray incident with a sufficiently large angle on the first array may not intersect with the second. Dr. Ayman Abouraddy et. al. [30] showed that the flexible geometric nature of this novel detection approach allows one to design an omnidirectional light detection through the construction of an optical array having a different topology, such as a closed-surface sphere. In this case, any ray of light (except for tangential beams) incident on the array must intersect the array again at exit. Such an array, as shown in Figure II-6(c), provides directional detection over a full 4π solid angle. Figure II-6(c) displays several distinctive features of our approach. The fibers are mechanically tough, yet very flexible, such that the array is almost self-supporting from a mechanical standpoint. Furthermore, the array is sufficiently sparse, and the fibers are sufficiently thin that the array is rendered nearly transparent and a beam

of light can traverse it with little impediment. Note that each fiber is an omnidirectional detector in the sense that it detects an incident light beam regardless of the relative angle between it and the beam. This is in sharp contrast with traditional optical detectors that can, at best, detect light incident from one-half of ambient space. Nevertheless, the fiber is not able to determine the angle of incidence, a task that is accomplished by arranging a multiple fibers into an array. The distribution of the detected electrical signals from the fibers is shown in Figure II-6(d) for the incident light beams shown in Figure II-6(c), clearly demonstrating the reconstruction of the beam path in three dimensions.
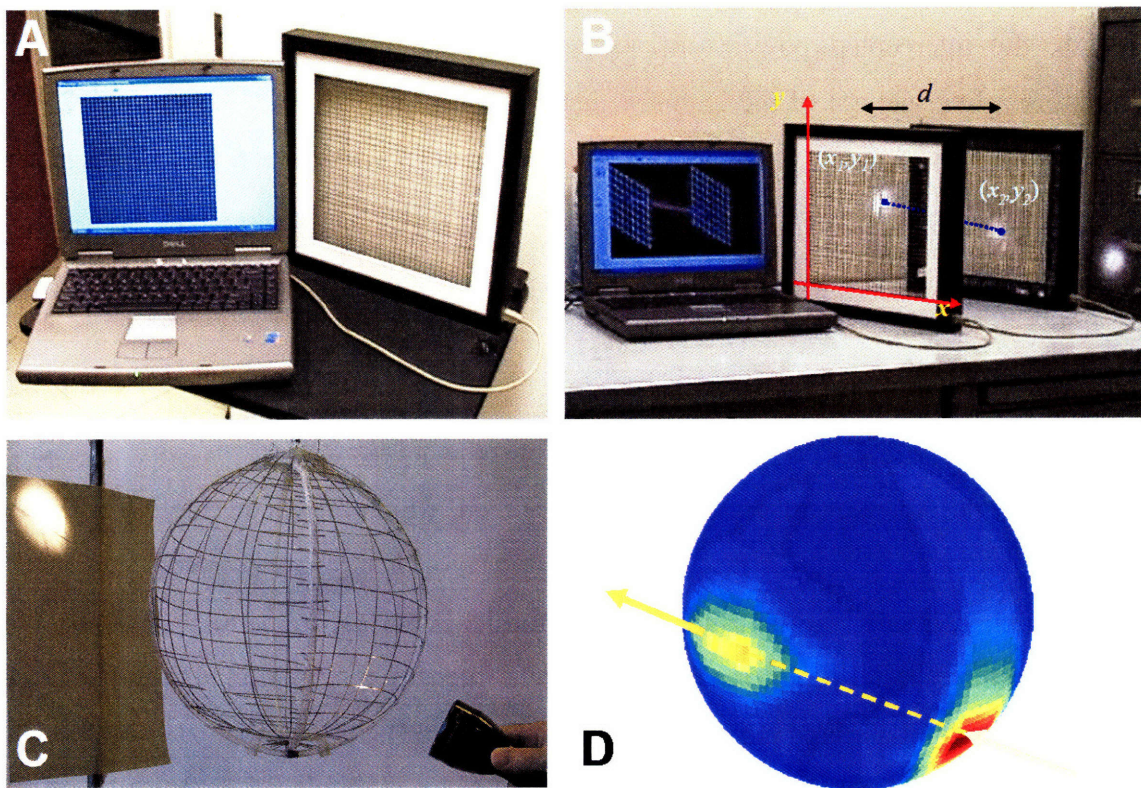
Figure II-6. (a) 2D planar fiber web that is capable of detecting a point of illumination. (b) Two planar fiber webs can determine the direction and location of a beam of light. (c) A closed spherical fiber web is an omnidirectional photodetector which detects the direction of the beam throughout a solid angle of 4π. The spherical web is sufficiently transparent to see through and for a beam of light to traverse unimpeded. (d) The distribution of the electrical signals detected by the fibers for the incident light beam seen in (c). The arrow indicates the direction of the beams, and the dotted portion of each arrow corresponds to the beam's path inside the sphere.

A lens-less imaging system developed by Dr. Ayman Abouraddy and Dr. Ofer Shapira [30-32] using the two parallel arrays described above is now described in more details. This will help to understand the lensless imaging system presented in chapter 4.

II.3.b. Lensless imaging system

The planar fiber web we presented can do more sophisticated tasks than just locating a point of illumination. It can indeed detect an arbitrary optical intensity distribution. Since each fiber detects the incident intensity distribution along its whole length, the intercepted power (and, consequently, the electrical signal produced) is therefore a line integral of the intensity distribution along the fiber. A fiber, of length L and diameter Δ ($\Delta \ll L$) placed along the line $x\cos\theta + y\sin\theta = t_1$ in an optical field having a two-dimensional intensity distribution $I(x,y)$, as illustrated in Figure II.7a, generates a photocurrent that is proportional to the intercepted optical power $P_\theta(t_1)$, given by

$$P_\theta(t_1) = \iint_{\text{fiber area}} dxdy\, I(x,y) \approx \Delta \iint dxdy I(x,y)\delta(x\cos\theta + y\sin\theta - t_1)$$

where t_1 is the intercept of the fiber with the t axis, which makes an angle θ with the x axis.

Consequently, the measurements performed by a set of parallel photodetecting fibers form a 'parallel projection' of the incident intensity distribution, a term used in the literature on computerized axial tomography (CAT) [33]. In that context it refers to the measurements performed by a linear array of point detectors placed on one side of a 2D object of interest, when a linear array of point sources (e. g., X-rays) is placed on the opposite side of the object. In our case, each fiber records the line integral of the intensity distribution of the optical field along its length. An example of a parallel projection produced by a fiber web is shown in Fig. II.7b, where a 32×32 fiber web (of dimensions 24×24 cm^2) intercepts an image of a letter 'E' and the two orthogonal projections obtained by the rows and columns of the web are displayed. The image is produced by a
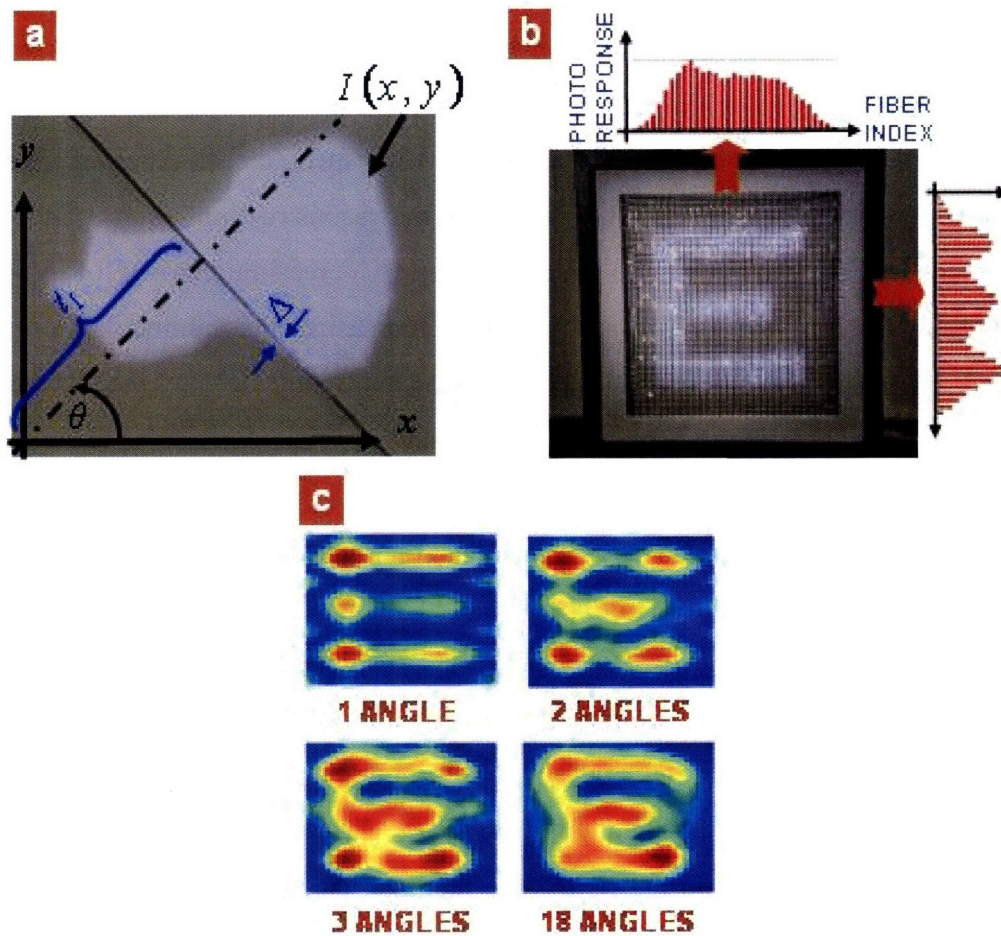
Figure II.7: Reconstructing an arbitrary optical intensity distribution with a planar fiber web. a, A photodetecting fiber of thickness Λ detects the line integral of the arbitrary incident optical intensity distribution, $I(x,y)$. b, An image of the letter 'E' is projected onto a 32×32 fiber web of dimensions 24×24 cm^2. The detected electrical signals from the web rows and columns (constituting 2 orthogonal projections) are also shown. The image of the letter 'E' seen here is formed on a white sheet placed behind the transparent web. c, Reconstructions of the incident intensity distribution, obtained using the backprojection algorithm, are shown with increasing number of projections. These projections are obtained by rotating the object transparency. 1 angle: 0°; 2 angles: 0°, 45°; 3 angles: 0°, 30°, 60°; and 18 angles: 0° to 85° in 5° steps.

white-light lamp (Xe-Hg) illuminating a transparency with dimensions 14×14 mm^2 placed at a distance of 1.2 m from the web. No lens is needed to form an image of the object transparency in this case because of the large dimensions (relative to the wavelength of light) used, highlighting the unique advantage of a detector array having such a large area.

These two apparently different arrangements (CAT and our fiber webs) are, surprisingly, mathematically isomorphic, allowing us to import the theoretical foundations of CAT for use in the problem at hand. In particular, we employ the

backprojection algorithm (Radon transform) [33], commonly used in CAT, to reconstruct an estimate of the impinging optical intensity distribution. In the case of fiber webs there are several strategies to achieve this: (1) rotating the fiber web; (2) using adjacent or interleaved fiber webs, each rotated by an angle with respect to each other; or (3) rotating the object that is imaged. In Fig. II.7c we show the reconstruction results of the image, obtained using the backprojection algorithm, with increasing number of projections recorded by rotating the object transparency. Increasing the number of projections acquired improves the fidelity of the reconstructed image to the incident intensity distribution.

While a single planar fiber web can detect the intensity of an incident optical field, two such webs can be used to detect both the field amplitude and phase, which constitute a complete representation of a scalar optical field. The effect of any optical device may then be simulated on a digital computer by manipulating this information about the field. The ability to reconstruct the field enables *lensless* imaging of an object by detecting the diffracted intensity image and then using *phase retrieval algorithm* [34-39] in order to gain complete information on the field. We then can calculate numerically the field in any other plane by using the Fresnel transform. The idea proceeds as follows. We use two planar fiber webs, located at two distinct diffraction planes, and obtain the incident 2D intensity distributions from both (by means of the CAT algorithm outlined above); we then implement the phase retrieval algorithm to retrieve the phase of the wave front; knowing the complex field at the first web, we can 'back-propagate' the wave front computationally until an estimate of the object is obtained.

The feasibility of this approach was demonstrated by producing an estimate of the amplitude and phase of an optical wave front produced by a letter 'E' having an overall size of 750×750 μm^2 (with features size of 150 μm; the object was a chrome mask on a glass substrate) illuminated with laser light having a wavelength of 830 nm. The 2D intensity distribution data obtained by a fiber web at two different locations in the far-field of the object is depicted in Fig. II.7b. We implemented the phase retrieval algorithm on the two obtained intensity distributions to reconstruct the object wave front. We define

an error metric $\Theta = \int d\mathbf{r} \sum_{n=1,2} \left(|G_n(\mathbf{r})|^2 - I_n(\mathbf{r}) \right)^2$ describing the distance between an estimate

$|G_n|^2$ and a measured intensity distribution I_n in both diffraction planes, $n = 1,2$. The distributions in the two diffraction planes are related to the object field distribution $g(x,y)$ through the Fresnel transform $\Im$, $G_n(u,v) = \Im\{g\}(u,v)$. The Nyquist frequency for such system is $1/L$, where L is the size of g (in one dimension) and the sampling rate corresponds to fiber spacing $< 2\pi d/kL$, where λ is the wavelength and d is the distance between the object and the array. The array size sets a cutoff for the spatial frequencies and therefore determines the sharpness of the reconstructed image. The phase retrieval algorithm used requires the minimization over the metric Θ with respect to the set of two-dimensional variables $\{g(n,m)\}$, where n and m are discretized spatial coordinates. The minimization is performed iteratively by repeating the following steps: (1) Calculate G_n in both planes using the previous estimate of g (an initial guess for g is needed in the first iteration). (2) Calculate Θ and its partial derivatives with respect to $g(n,m)$. (3) Using the gradient-search method, find the next estimate of g (with smaller error). These steps are repeated until the change in the error metric is limited by the system noise.

A Gaussian beam, from a Ti:Sapphire laser tuned to a wavelength of 830 nm, is incident perpendicularly on an amplitude mask with the letter 'E', generating a Fresnel diffraction pattern 12 cm away from the mask with size of $\sim$ 1 mm, and a Fraunhofer diffraction pattern 80 cm away with size of $\sim$ 6.5 mm. In this proof-of-principle experiment, we magnified those patterns to match the array size. We implemented the above described phase retrieval algorithm using an optimization routine from MATLAB©, and optimized the error function to obtain the reconstructed field at the plane of the mask. The iterative process converged after less than 20 iterations to an error of less than 1%. Having an estimate of the amplitude and phase of the field in one plane, one can use to propagate the field to *any* other plane, and a "focused" image is observed at a distance that matches the location of the object We compared these results to a theoretical model that numerically propagates the field from the object, using the object distribution modulated by the incidencet laser beam (as captured by a Vidicon camera) and taking into consideration the 32×32 discretization of the diffracted fields at the measurement planes. The calculated images and the reconstructed fields are given in Fig II.7.c.
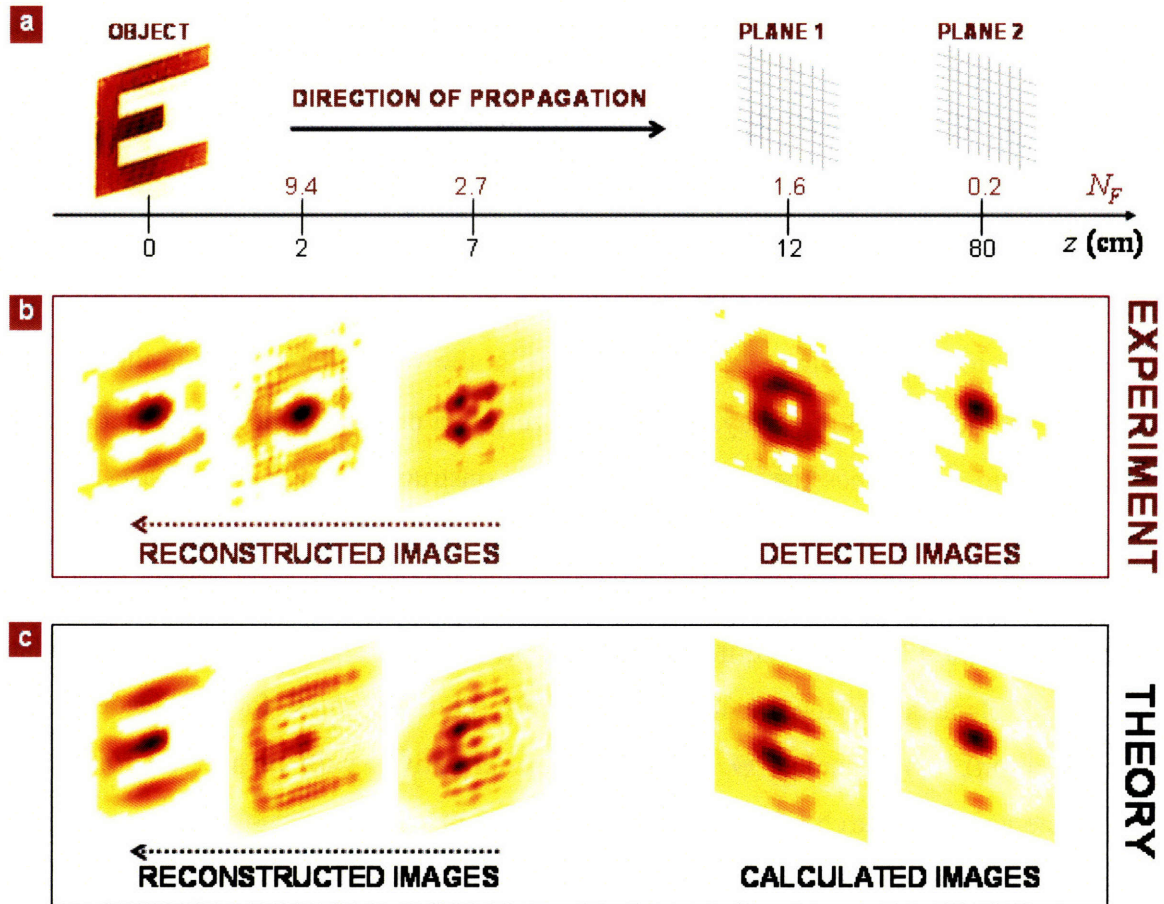
Figure II.8: a, An object (letter 'E') is illuminated with a laser beam (the image of the object is captured with a Vidicon camera) and the diffracted fields propagate to the planes of two 32×32 planar fiber arrays at two different locations (Fresnel zone, 12 cm, and Fraunhofer zone, 80 cm, shown on the right, first row) are obtained using the fiber webs. The Fresnel number N_F is also given. b, Two intensity distributions are measured. The phase retrieval algorithm is used to obtain back-propagated images in the direction receding from the webs towards the object (the object reconstruction is at at 0 cm, shown on the left). The reconstructed images are blurred, but a clear image is obtained at the location of the object. c, The second row shows the results of theoretical reconstructions with the phase retrieval algorithm when using near- and far-field diffraction patterns that were obtained from the measured illuminated object distribution.

In order to verify the fidelity of the amplitude and phase estimation, we use the acquired complex wave front to 'propagate' the field computationally at distances receding from the first web towards the object. A set of these computed estimates is shown in Fig. 5.3b. The estimates are blurred until we approach the location of the object where a clear image is formed. For comparison, we used scalar diffraction theory to calculate the diffracted field of a letter 'E' modulated by a Gaussian beam at the two measurement planes, the resulting amplitudes, truncated to the array size, are shown in

Fig. 3. We then used the phase retrieval algorithm to reconstruct the object at those same planes receding from the first array.

There are several unique features of our approach that are not captured by other techniques that sample a 3D electromagnetic field such as photorefractive crystals, for example. First, our fiber webs are 2D manifolds embedded in 3D space, and therefore they capture much less light than a truly 3D volumetric sampling detector. This serves to reduce the amount of acquired data and minimizes the absorbed power. Second, no optical readout is required, as is the case in photorefractive crystals, since information is acquired directly in the form of an electrical signal. Most importantly, the size of our fiber webs can be made arbitrarily large, an advantage not shared by any other rival technology.

Finally we comment on the weight of such arrays. Assume a 1×1 m^2 array formed of 1-mm diameter fibers with 1-cm spacing providing 10,000 detection points. With average density of the fiber materials being 1.84 gm/cm^3, the overall weight of the array is 0.289 kg, which is negligible when compared to the weight of any traditional optical component of comparable size. Note that using fibers with smaller diameters allow for weaving denser arrays.

Fibers demonstrated in this chapter integrate for the first time optic (with the optical filter), electronic (the fiber can be seen as a simple resistor) and optoelectronic (the fiber acts as a photoconductor) functionalities. This generated a lot of interest in the academic as well as in the industrial world. The new direction I took in my thesis work was to understand better the physical phenomena in play in the detection of light, and to study the geometric and structural influence on the photodetecting fiber to improve both its efficiency and functionalities.

III. Geometric and structural analysis of hybrid photoconducting fiber devices

III.1. Motivations

The recent development of co-drawn metal-insulator-semiconductor photodetecting fiber-based devices described above has heralded a novel path to optical radiation detection [17-20,30-32] For the first time, device-like performance may be delivered at length scales and in a mechanically flexible form hitherto associated with optical fibers. At the heart of the fabrication process is the simultaneous reduction of the cross-section and extension of the axial dimensions of a macroscopic preform. Thermal drawing results in extended lengths of functional fiber while maintaining the material composition and transverse geometry throughout the entire length. Although beneficial for many applications, the extended length scales of fiber-devices tend to degrade their performance by raising the noise floor. My next study aims to minimize the noise per unit length by identifying optimal fiber structures and geometries [40]. A comparative study of the responsivity, noise and sensitivity [41,42] of photodetecting fibers as a function of structural and geometric scaling parameters is performed. This leads to the introduction of a novel thin-film photodetecting fiber device architecture. Precise control over the submicron scale dimensions affords more than an order of magnitude increase in the fiber-device sensitivity. Potential applications of fiber devices include remote sensing, functional fabrics, and large-area, two-dimensional (2D) and three-dimensional (3D) arrays (or "fiber webs") capable of optical imaging.

We will start this chapter by describing the fiber structures under study and explain the basic principles of photoconduction and the model we will use in the course of our work to derive the different quantities of interest. In a second part we will define the dark and noise currents in photoconducting fiber devices and study the influence of fiber length and diameter on them. The third and fourth parts will deal with the fibers under illumination, how light is absorbed inside the fiber device and how the photocurrent scales with these same geometric parameters. Finally, we will introduce a new thin-film structure and compare it with its solid-core counterpart.

III.2.   Formulation of the problem

III.2.a. Fiber structures and parameters

The basic structures and scaling parameters of the fibers discussed in this chapter are illustrated in Figure III-1. The mesoscopic-scale fiber devices are produced from a macroscopic-scale preform, having the desired device structure albeit at macroscopic dimensions, by a thermal drawing technique described in Chapter 1. Two basic fiber-device structures are considered here and are contrasted in Figure III-1(b) and Figure III-1(c). The first structure [17,18] consists of a solid amorphous semiconducting core contacted with four metallic conduits (tin) and a protective polymer cladding, poly(ether sulfone) (PES) that encapsulates the device while simultaneously imparting mechanical strength and flexibility to the fiber. Figure III-1(b) shows a schematic drawing (b1), a scanning electron microscope (SEM) micrograph (b2) of the cross section, and a longitudinal section of this fiber device (b3). The drawing process maintains the ratio of the solid-core diameter d, the scaling parameter under investigation, to the outer diameter of the fiber. The second fiber device is similar to the above described device except that the photoconducting element is a thin film (of the same material used in the solid-core fiber) supported by an inner polymer tube. Figure III-1(c) shows a schematic drawing (c1), an SEM micrograph (c2) of the cross section, and a longitudinal section of this fiber device (c3). This new structure allows for two independent scaling parameters to be varied: the diameter of the thin film d (corresponding to the diameter of the above described solid-core device) and the film thickness t. We show that this additional degree of freedom enables the design of photodetecting fibers with enhanced sensitivities. The amorphous semiconductor used in this paper is a chalcogenide glass having the formula $As_{40}Se_{54}Te_6$. The composition can be changed to optimize the performance according to the application at hand, but the scaling trends reported here are essentially *independent* of the semiconductor used.
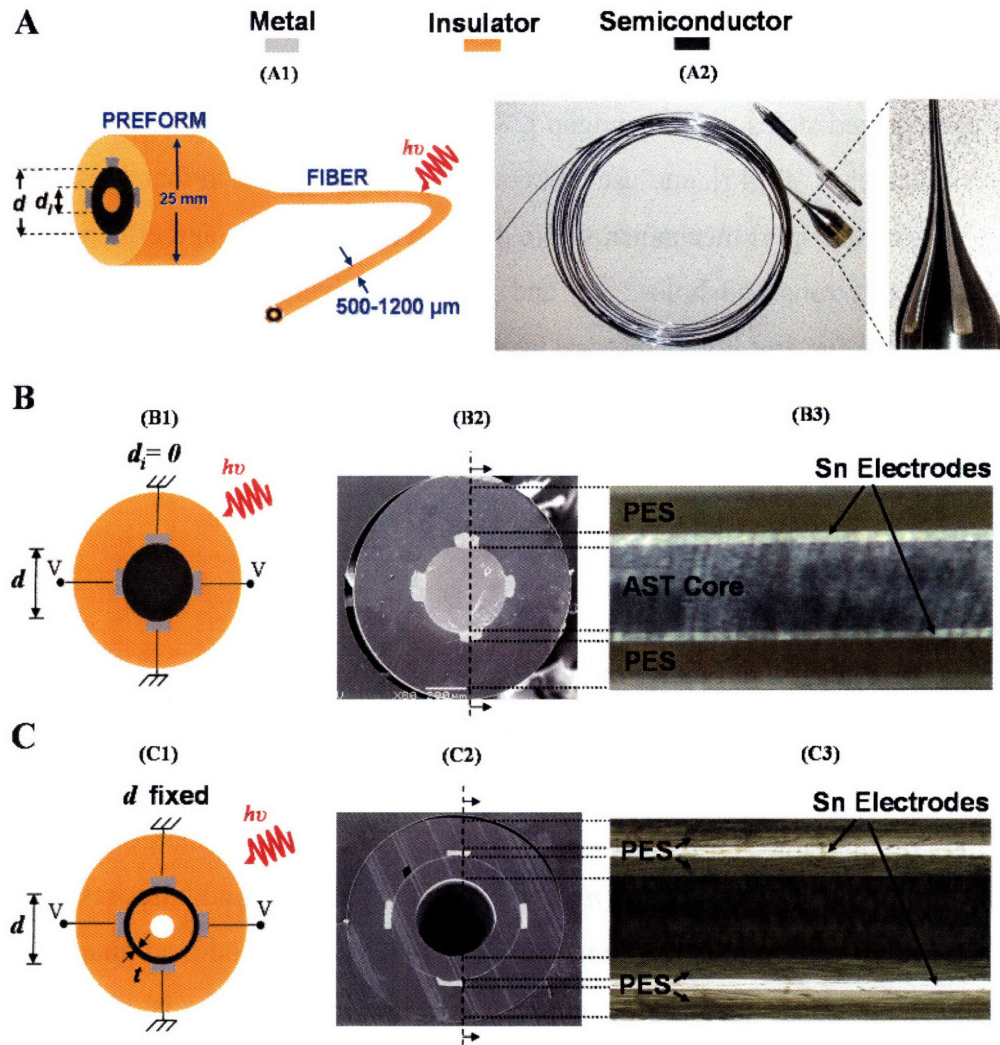
Figure III-1. Geometry and structure of mesoscopic photodetecting fiber devices. (a) A macroscopic preform is drawn down to a mesoscopic fiber (a1). Meters-long fiber devices (a2) are produced from the preform (the neck-down region of the preform is shown in the inset). (b) Schematic cross-section of a solid-core fiber device showing the electrical connections to an external circuit and the relevant device parameters (b1). Scanning electron microscope images of cross section (b2) and image of a longitudinal section of the fiber device (b3). (c) Schematic cross-section of a thin-film fiber device showing the electrical connections to an external circuit and the relevant device parameters (c1). Scanning electron microscope images of cross section (c2) and image of a longitudinal section of the thin-film fiber device (the thin film is not visible in the longitudinal section) (c3).

III.2.b. A phenomenological approach

To discuss the influence of the fiber geometric parameters we need to take into account the amorphous nature of the semiconductors used. Conduction in disordered materials occurs when carriers travel into extended states, as well as hop between localized states in the gap. These complex microscopic transports involving trapping and

releasing events as well as recombinations have been extensively studied, and different models exist that account for the complexity of the problem due to the presence of a high density of localized states in the bandgap [28,29,43,44]. In our study, we will follow the approach of Ritter et. al [45], and use a phenomenological approach that does not depend on the details of transport mechanisms. We define a drift mobility and effective diffusion constants for electrons and holes, $\mu_{n,p}$ and $D_{n,p}$ respectively, the under script n and p referring to electrons and holes, that are averages for all the carriers in extended as well as in localized states inside the bandgap. This leads to definitions of the drift and diffusion current densities as:

$$\vec{J}_p^{\,drift} = \mu_p p \vec{E} \tag{III-1a}$$

$$\vec{J}_p^{\,diff} = -D_p \vec{\nabla} p \tag{III-1b}$$

where $\vec{E}$ is the electric field and p the total concentration of holes. Similar relations hold for electrons. We also define life times τ_n and τ_p for electron and holes, which are average life times for free and trapped carriers. We will consider a small signal approach as in [45] where the illumination is low enough so that the increase of charge concentrations compared to their value in the dark (n_{dark} and p_{dark} for electrons and holes respectively) is small, to avoid the complication due to the dependence of these defined quantities on the carrier concentrations. The extra current due to illumination is then given by $\Delta \vec{J}_p = \mu_p' \Delta p \vec{E}$ where Δp is the excess hole carriers and μ_p' the small signal hole mobility.

This phenomenological model has the advantage of giving a simple framework in which to understand the effects of the structure and derive the scaling laws of interest while dealing with conduction in the amorphous semiconductor in use.

III.2.c. Dark current and noise

In the dark, the uniformity of the core semiconductor and charge neutrality imply that the electrical potential distribution in the fiber cross-section is given by the Poisson equation $\vec{\nabla}^2 V = 0$. We use the cylindrical coordinate system shown in Figure III-1 and neglect edge effects at the ends of the fiber (all physical quantities are uniform in the z

direction). We also neglect the electron drift mobility due to the p-type nature of Chalcogenide glasses and so have a dark conductivity given by $\sigma_{dark} = ep_{dark}\mu_p$, where e is the elementary charge and p_{dark} the concentration of holes in the dark. In the steady state ($\nabla \vec{J}_{dark} = 0$,being the current density) and with the symmetry implied by the external applied voltage scheme shown in Figure III-1, the total dark current is for a fiber of length l and diameter d is:

$$I_{dark}(l,d) = 4l\sigma_{dark} \int_0^{d/2} E_\theta (r,\theta = \pi/4)dr \qquad \text{(III-2)}$$

(the factor 4 accounts for the four currents between the pairs of neighboring electrodes). From this equation we see that the dark current scales linearly with the length of the fiber for any given diameter.

One succinct way of describing the effect of the fiber diameter on the dark current is to look at the potential distribution in the core, and to consider a simple geometric transformation. If the potential distributions for fibers having diameters d and D are $V^d(R,\theta)$ and $V^D(R,\theta)$, respectively, then $V^d(r,\theta) = V^D(r\frac{D}{d},\theta), r \in [0,d]$. In other words, finding the potential distribution for one diameter yields the distributions for all other diameters after scaling. By the same token, the scaling of the electric field $\vec{E}(r,\theta) = -\vec{\nabla}V$ with fiber diameter is

$$\vec{E}^d(r,\theta) = \frac{D}{d} \vec{E}^D(R,\theta) \qquad \text{(III-3)}$$

Using the scaling argument provided in Equation III.3, however, it can be easily seen that I_{dark} is in fact independent of d, such that the dark current depends on the fiber length alone.

The value of the dark current is important when one considers the noise of such devices. In photoconductors, noise is dominated by the dark current fluctuations due to the Johnson noise and the generation-recombination process [41,42]. The treatment of noise is complicated in our case by the amorphous nature of the photoconducting element where trapping and release events due to the high concentration of localized states, as well as the different recombination mechanisms and life times, need to be taken into

account. Our purpose here is not to have a detailed study of the frequency dependence of the spectral density, but rather to get an idea of the influence of fiber geometric parameters on the amplitude of the noise current. We can use two simple and succinct approaches where we assume only a dark current noise (no background or amplification noise): first, using the phenomenological model described in part one, we can reduce the noise mechanism to one of a p-type semiconductor with mobility μ_p and life time τ_p and consider a generation process with associated time constant τ_p. Considering a Maxwell-Boltzman distribution of the holes participating to the current and following the treatment of Ref 7, we can derive an expression for the amplitude of the current noise i_N in a fiber device of diameter d, taking into account the particular geometry of our system:

$$i_N = \left(\frac{16e\mu_p A}{\pi}\right)^{1/2} \frac{\sqrt{I_{dark}}}{d} \tag{III-4}$$

where A is the integral in Equation III-2 and is size independent.

Models for the noise in amorphous semiconductors with a large density of localized states have also been studied [46]. When each trapping and releasing event is considered random and has a shot noise associated with it, a similar expression for the noise current amplitude is obtained for our particular geometry by, for example, adapting the method of R-C equivalent circuitry [46]. From this analysis it is clear that the noise increases with the square root of the fiber length and the inverse of the diameter as is apparent in the results shown in Figure III-7. The dark current I_{dark} and photocurrent I_{ph} were measured with a pico-ameter (Keithley 6487), applying a constant voltage of 50V throughout this study. The noise current i_N was measured by carefully shielding the fibers from the environment, recording the current over an extended period of time (typically 10 minutes), and statistical analysis of the amplitude of the fluctuations. In Figure III-2 we show a typical current noise measurement and a Gaussian fit that we extracted from it. Plotted is the number of time a certain current value is measured over the period of time data were recorded. We can see that it fits pretty well a Gaussian density g with a mean the mean dark current and standard deviation the one measured from the recorded data.
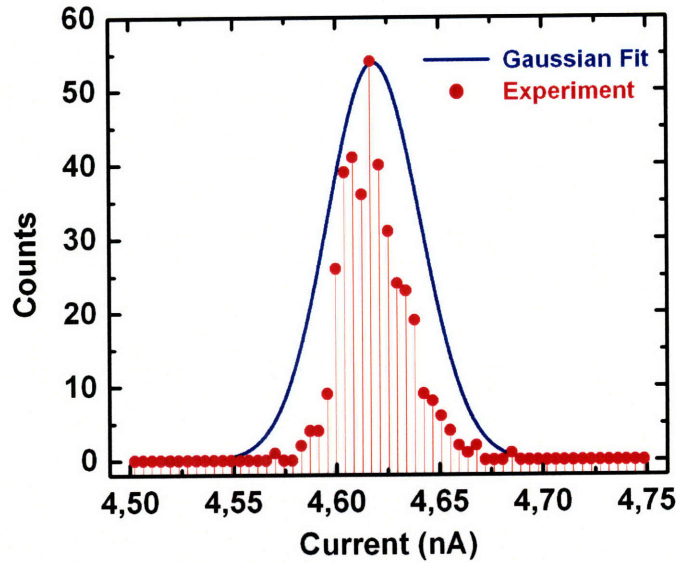
Figure III-2. Number of time (counts) a value of the dark current was measured over a long period of time (typically 15mn) for a 7 cm long solid-core fiber. Red points are the experimental data. The blue curve is a Gaussian fit of the data, where the mean is the mean dark current and the standard deviation is the one measured from the experimental data.

This increase of noise is of concern when one thinks about large area optoelectronic applications with long and thin fibers. Let us see next how light is collected in fiber-device before studying the effect of geometric parameters on the photo-current.

III.3. Light collection and photon flux

Let us consider a fiber of radius R, with a ratio η between the fiber radius and the glass core radius (i.e. $R^c = \eta R$). We also consider an incident plane wave of frequency ω and intensity $\hbar\omega\Phi_0$, as shown in Figure III-3 below. Reflection and transmission will occur due to the index of refraction mismatch at the air-polymer and polymer-glass interfaces. Thanks to the cylindrical shape of the device, the polymer cladding (n_{PES}=1.7 in the range of wavelengths considered for PES) has the advantage of focusing the incoming beam onto the glass core. A light beam reaching the fiber at a point $A(R,\alpha)$ with an intensity of $\hbar\omega\Phi_0\cos(\alpha)$ along the circle line is transmitted and reaches the semiconductor core surface at a point $B(\eta R,\upsilon)$ if its path indeed intercepts with the surface of the core. This is always the case when the ratio η is greater than a critical value

obtained by looking at the limiting case where the incident beam is tangential to the fiber. In that case the beam and the radius form a right angle and using Snell's law, we have $n_{PES} \sin \beta' = 1$. Moreover, in the right triangle we have OB'A' $\sin \beta' = \dfrac{\eta d}{d} = \eta$, which leads to the value $\eta_c = \dfrac{1}{n_{PES}}$.

METAL   **GLASS**   **POLYMER**
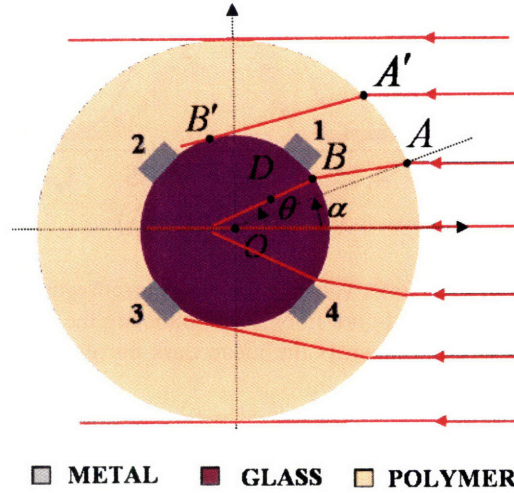
Figure III-3. Schematic view of the absorption of an incoming uniform beam reaching the fiber device.

For a given point $D(r,\theta)$ inside the fiber core, using simple geometric considerations, it is straightforward to reconstruct the incoming beam reaching the point $D(r, \theta)$ and find $B(\eta R, v(\theta))$ and $A(R, \alpha(\theta))$, as well as the angle between the radius and the transmitted beam in the core $\gamma(\theta)$. From these calculations, the transmission can also be derived, and the photon flux inside the core at a point $D(r, \theta)$ is then given by, neglecting absorption in the polymer, the following formula:

$$\vec{\Phi}(r,\theta) = T(\theta)\Phi_0\left(-\cos(\gamma)\vec{e}_r + \sin(\gamma)\vec{e}_\theta\right)e^{-\dfrac{d_{BD}}{\delta_{Glass}}} \qquad (\text{III-5})$$

The exponential term represents the absorption of light into the semiconducting core, where δ is the penetration depth defined as $\delta = \lambda/4\pi k$, λ is the wavelength of illumination, and k is the imaginary part of the refractive index. d_{BD} is the distance between points B and D.
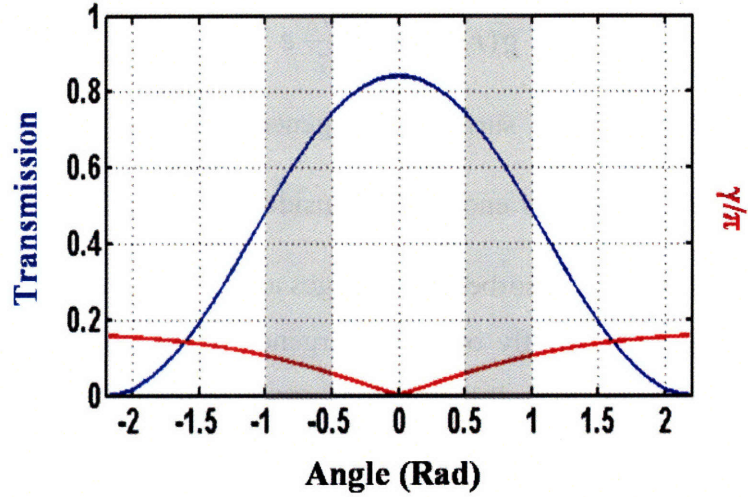
Figure III-4. Transmission (blue) and angle of transmitted beam with respect to the radius (red), along the core surface, of an incoming light as pictured in Figure III-3. The shaded regions represent the space occupied by the electrodes.

This can be greatly simplified in our case, looking at Figure III-4 where we computed the transmission coefficient T(θ) (in blue) and the ratio $\gamma(\upsilon)/\pi$ for a TE polarized beam, with respect to the angle υ ($\upsilon = \theta$ on the core surface, where $r = \eta R$). We used a typical ratio of $\eta = 0.44$, and an index of refraction of 3.2 for As_2Se_3. The electrodes 1 and 4 are placed at angles ± 0.485, as indicated by the shaded regions. The change of the transmission between these two electrodes is found to be less than 8%, while the angle γ between the radius and the transmitted light is less than 0.19 rad (10 degrees). This enables us, with a very good approximation, to consider that the transmission T is independent of the angle between electrodes 1 and 4, and that $d_{DB} \approx d/2 - r$. If $T\Phi_0$ is the surface distribution of incoming photons on the solid-core, the surface distribution at a distance r is related to it by, given the absorption:

$$lr\Phi(r)d\theta = T\Phi_0 l \frac{d}{2} e^{-(\frac{d}{2}-r)/\delta} d\theta$$

so

$$\Phi(r) = \frac{d}{2r} T\Phi_0 e^{-(\frac{d}{2}-r)/\delta}$$

Looking at the number of charges absorbed, we can derive the generation rate:

$$\frac{d(r\Phi)}{dr} = rg(r)$$

$$g(r,\theta) = \frac{dT\Phi_0}{2r\delta} e^{-\frac{d/2-r}{\delta}} \tag{III-6}$$

We see that close to the surface, the generation rate can be approximated by

$g = \frac{T\Phi_0}{\delta} e^{-(d/2-r)/\delta}$, which is enough to consider as we will see at short wavelengths

where the light is strongly absorbed and charges are only generated close to the surface.

Let us comment briefly on the divergence of the generation rate when $r \to 0$. Indeed in our approximation, all the photons concentrate on the $r = 0$ point, leading to a divergence in their concentration. In the calculations of the current however, in the integrals in Equations (III.11) and (III.12), we see that g is multiplied by the electric field E that changes linearly with r for small radius as apparent on Figure III-5a. There is then no divergence problem when integrating the current density between 0 and d/2.

III.4. Scaling laws and fiber device characteristics

III.4.a. Responsivity and sensitivity

Let us consider a plane wave illuminating a fiber device as shown in Figure III-3, the $\theta = 0$ line being a plane of anti-symmetry of the system. As we indicated earlier, we assume that the light signal is small enough to use the small signal approach described in [45]. The electric field is also low, which leads us to consider that charge neutrality is maintained and so $\Delta n = \Delta p$, where Δn and Δp are the total change in electrons and holes concentrations, respectively, due to illumination. Under these conditions, and if we assume that each photon absorbed generates an electron-hole pair, the transport equation in steady state is given by,:

$$0 = g - \frac{\Delta p}{\tau} + D\nabla^2(\Delta p) + \mu\vec{\nabla}(\Delta p\vec{E}) \tag{III-7}$$

where g is the generation rate and τ, D and μ are ambipolar life times, diffusion constant and mobility, respectively [45]. To solve this equation for our particular geometry, approximations can be made depending on the value of the penetration depth of the incoming beam compared to the fiber diameter. Note first that the last term of Equation

III.7 can be written as $\nabla(\Delta p \vec{E}) = E_r \dfrac{\partial \Delta p}{\partial r} + \dfrac{E_\theta}{r} \dfrac{\partial \Delta p}{\partial \theta}$ since the dark current is conservative, as we saw earlier. We can then distinguish between two cases:

Case #1. If the penetration depth is much smaller than the fiber diameter ($\delta \ll d$): photo-generated charges are created close to the surface and diffusion towards the center of the fiber will occur. The diffusion length is orders of magnitude smaller than the fiber diameter. Therefore far from the surface Δp is negligible, Moreover, we can show that the electric radial component of the electric field can be neglected close to the surface as apparent in Figure III-5. We used the FemLab software, which is based on the finite element method, to calculate the electric field distribution in the cross section of the fiber solid-core modeled as a conducting element with conductivity σ. We computed a structure exactly similar to the one seen in Figure III-1 and we set the boundary conditions as follows: interfaces between the polymer and the glass were set to have no charge surfaces, and the electrodes were set to a 50V potential (as used in the experiments) and to the ground as shown in Figure III-1. On Figure III-5a we show the value of the electric field along the radius that lies in between 2 electrodes. To show that the radial component of the electric field is negligible close to the surface, we extracted from the simulation the radial and angular components along a curve that is 2 micrometers away from the surface. The angular component is found to be almost constant, and we plotted in Figure III-5b the ratio of these two components along the curve. It is clear from the plot that the approximation made of neglecting E_r with respect to E_θ close to the surface of the solid-core, but also in the thin film, is justified.

Finally, the transmission can be approximated as independent of the angle between electrodes 1 and 4, and we can assume that the light path follow the radius, as we explained in the previous section. Therefore, the last term of Equation III-7 is negligible everywhere. We then have, in cylindrical coordinates:

$$\frac{\partial^2 (\Delta p)}{\partial r^2} + \frac{1}{r} \frac{\partial \Delta p}{\partial r} - \frac{\Delta p}{L^2} = -\frac{g}{D} \qquad \text{(III-8)}$$
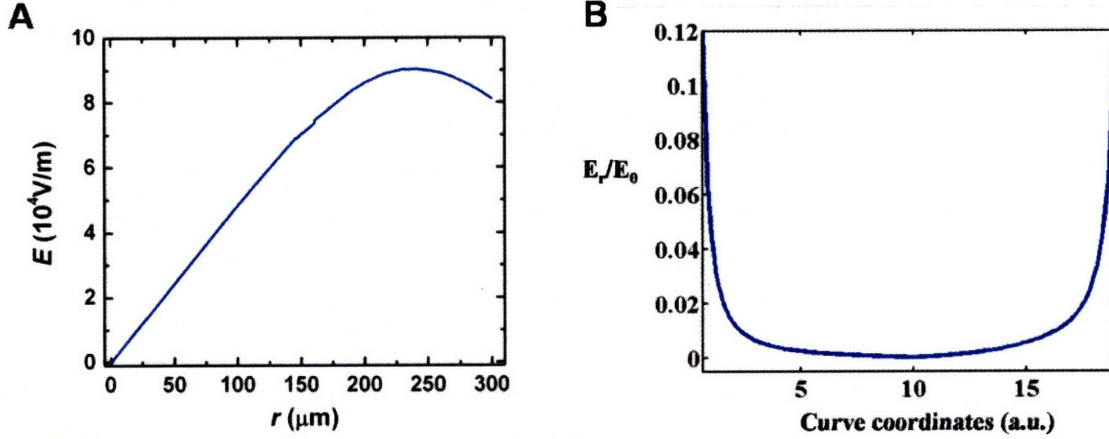
Figure III-5. Ratio of the radial and angular components of the electric field in a photodetecting fiber, along a curve 2 micrometers away from the core surface, between two electrodes.

with $g \approx \dfrac{T\Phi_0}{\delta} e^{-(d/2-r)/\delta}$. The solution of the homogeneous differential equation is a linear combination of Bessel functions of the first and second kinds. To simplify, we will neglect the second term of this equation, motivated by this simple argument: far from the surface, the free photo-carrier concentration is null, whereas close to the surface the $1/r$ factor makes this second term negligible compared to the second derivative of the free photo-carriers concentration. We choose a boundary condition on the core surface of zero concentration of extra charges due to the presence of a high density of recombination centers. The solution to this equation is then simply given by:

$$\Delta p = \frac{T\Phi_0 \tau}{\delta(\alpha^2 - 1)} \left[e^{-(d/2-r)/L} - e^{-(d/2-r)/\delta} \right] \qquad (III.9)$$

where $\alpha = L/\delta$. To verify the fact that the second term in (6) may be neglected we write at the surface:

$$\left| \frac{2}{d} \frac{\partial(\Delta p)}{\partial r} [d/2] \right| = \frac{2L}{d} \left| \frac{\partial^2(\Delta p)}{\partial r^2} [d/2] \right| \qquad (III.10)$$

which justifies the approximation made, keeping in mind that $L \ll d$. As the photo-current density $\Delta \vec{J}$ is conservative, we can integrate it along any surface perpendicular to its lines to obtain the current going through electrodes 1 and 4:

$$I_{ph}(\delta \ll d) = \frac{C}{\delta(\alpha^2 - 1)} \int_0^{d/2} \left(e^{-\frac{d/2-r}{L}} - e^{-\frac{d/2-r}{\delta}} \right) E_\theta^d(r,0)dr \qquad \text{(III.11)}$$

where $C = e\mu\tau ZT\Phi_0$ and Z is the extension of the light beam along the fiber axis. Note that we neglect the effects of diffusion along the fiber axis, as Z is orders of magnitudes longer than the diffusion length (evaluated to be between 100 nm and 10 µm for our glasses [45-51]). Also, this is taking into account only the current between electrodes 1 and 4, as all the charges are generated close to the surface, and will not reach the area between electrodes 2 and 3.

Case #2. The penetration depth is approximately equal to or larger than the fiber diameter ($\delta \approx d$ or $\delta \gg d$): Diffusion can be neglected in this case, except at the surface where charge diffusion occurs due to the zero concentration of photo-generated charges boudary. As this occurs within a few micrometers from the surface, we can neglect this effect compared to the hundreds of micrometers over which the current is integrated and reasonably neglect the diffusion. The last term of Equation III.7 can still be neglected because charges are absorbed almost uniformly between electrodes 1 and 4, and 2 and 3. We then simply have $\Delta p \approx g\tau$. Using the value of the generation rate derived in the previous section and taking into account the current collected between electrodes 2 and 3, the photo-current can be written as:

$$I_{ph}(\delta \approx d) = \frac{Cd}{2\delta} \int_0^{d/2} \left(\frac{e^{-\frac{d/2-r}{\delta}}}{r} + \frac{e^{-\frac{d/2+r}{\delta}}}{r+d/2} \right) E_\theta^d(r,0)dr \qquad \text{(III-12)}$$

From Equations III-11 and III-12 we see that the photocurrent changes linearly with the light intensity, as we expected when we considered a small signal approach where only monomolecular recombination occurs. It is also linearly dependent on the extension of illumination along the fiber axis. The ability to integrate intensity along the entire length is an important advantage of a distributed 1D photoconducting fiber device. The photocurrent of an arsenic triselenide (As_2Se_3) fiber core illuminated at different powers with the 522nm line of a tunable Argon laser source is shown in Figure III-6. Here, the photocurrent for different lengths of excitation from a white source is plotted. A clear linear behavior is observed in both cases.
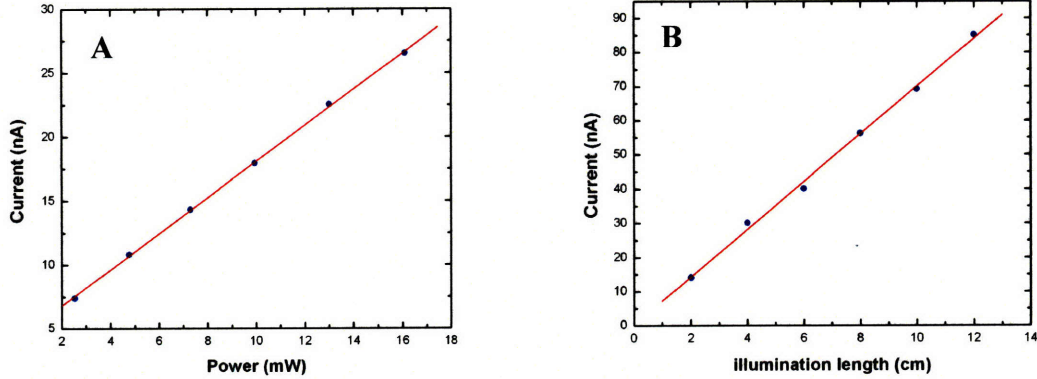
Figure III-6. Photocurrent for an As2Se3 core fiber device (a) for different illuminating powers at 522nm and (b) for different length of illuminated fiber, for a constant light source.

We can now evaluate the effect of the fiber length and diameter on the photo-current. We see from Equations III-11 and III-12 that the photo-current is independent of fiber length as long as it is greater than the beam expansion Z. This is straightforward as the increase of length does not influence the absorption of light by the device. When the fiber length gets shorter than the beam expansion however, light is absorbed only along the fiber length and the dependence of the photo-current on fiber length is shown by replacing, in Equations III-11 and III-12, the factor Z by $min(l,Z)$ where l is the fiber length. This is apparent in Figure III-7(a), where the photo-current stops increasing as the length of the fiber becomes larger than the extension of the beam. The raise of current observe as the fiber length increases is only due to the increase of dark current.

Now, in order to look at the influence of the diameter on the photo-current, we make the change of variables $R = \dfrac{D}{d}r$ to perform the geometric transformation inside the integral in Equation III-11. Compared to a reference diameter D, the photo-current for a fiber of diameter d is given by:

$$I_{ph}(d) = \frac{C}{\delta(\alpha^2 - 1)} \int_0^D \left(e^{-\frac{D - R}{L}\frac{d}{D}} - e^{-\frac{D - R}{\delta}\frac{d}{D}} \right) E_\Theta^D(R,0) dR \qquad \text{(III.13)}$$

A similar change of variable can be made in Equation III-12. We use a value of 100 nm for L, a reasonable guess from literature. However, our model is very robust to a change
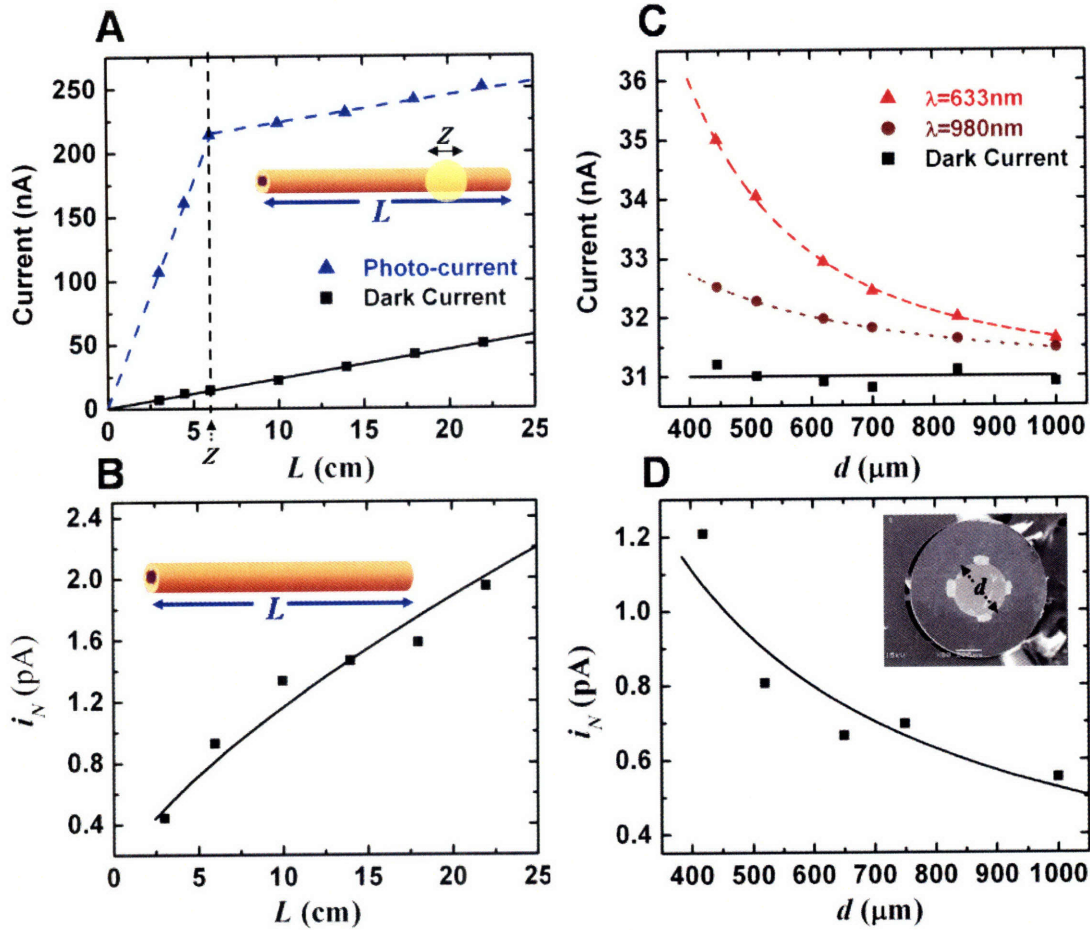
Figure III-7. Scaling trends for solid-core fiber devices. (a) Dependence of the dark current and photocurrent (white light illumination over a spot of diameter z) on the fiber length L. (b) Dependence of noise current on fiber length L. (c) Dependence of dark current and photocurrent (at two wavelengths) on the diameter of the fiber core d. (d) Dependence of noise current on d.

of L and a change of an order of magnitude (L = 1 μm) leads to a change in the theoretical model of less that 0.1%.

The result was verified experimentally by measuring I_{ph} for fibers having different d values ranging from 440 to 1000 μm under fixed illumination conditions (same incident power on the fiber devices). The spectral dependence of I_{ph} was investigated at two wavelengths, λ = 633 nm (He-Ne laser) and λ = 980 nm (laser diode). The penetration depths δ used for the simulations, obtained from measuring the imaginary part of the glass refractive index, are $\delta(\lambda$ = 633 nm) = 100 nm and $\delta(\lambda$ = 980 nm) = 425 μm. Figure III-7(c) demonstrates that the results of our model agree well with the experimental data. Finally, in Figure III-7(d) we plot i_N as a function of d, showing the expected inverse

proportionality. Thus, while smaller diameters afford a larger I_{ph} ($I_{ph} - I_{dark} \propto 1/d^2$) they also result in a larger i_N ($i_N \propto 1/d$); nevertheless, the sensitivity increases for smaller fiber diameters $s \propto 1/d$. The background noise resulting from the extended length of a photodetecting fiber device is hence compensated by a reduction of its cross-sectional dimensions.

III.4.b. Response time

We will briefly comment on the time response of fiber devices, although a thorough study including the effect of temperature would be necessary to confirm our findings. We need here to take into account the details of the dynamics of trapped and free carriers and the particular form of the localized states distribution. The current in the glass is carried out by the shallow, high-mobility states, but the transient current reflects the trapping of carriers in progressively deeper states (traps), in the band tail [48-50]. The band tail of localized states above the mobility edge can be represented by a distribution of the form $N_t(E) = \dfrac{N_t}{E_0} \exp\left(-\dfrac{E}{E_0}\right)$, where N_t is the total density of localized states and E_0 the characteristic energy of the localized states distribution, and where the mobility edge is set to a zero energy [50-52]. If the total filling of gap states is not achieved at steady state, the initial portion of the decay is governed by capture processes, and the recombination becomes dominant at later times. We assume this to be the case here for low light intensities. This is due to the fact that the trapping time of free carriers, i.e. their life time before being trapped in localized states in the gap, is much shorter than the recombination time [48,50,51, 53,54]. We measured the rise and decay times of fibers with an As2Se3 and $As_{40}Se_{54}Te_6$ solid-core of different diameters but the same length, and vice versa. No influence of the power for the range of power used, nor fiber size, was observed. This was expected as the dynamic of the transient current is governed by size independent materials properties.

These conclusions have significant practical consequences. Since thinner fibers are more flexible, they can be tightly woven into complex fabrics and systems. Moreover,

reducing the fiber diameter increases the manufacturing time and cost efficiency, since a given preform will produce more fiber length as the target diameter is reduced (per volume conservation). Our study shows that, counter intuitively, thinner fibers are also *more sensitive* (due to the increase in responsivity), which adds to the motivation of our efforts to produce fibers with even smaller cross-sectional dimensions.

To increase the sensitivity of a device, we can raise its responsivity as we just did by reducing the fiber diameter. An other approach is to maintain the same level of responsivity for a given signal but decrease the noise associated with the device.

III.5. From solid-core to thin-film fiber devices

III.5.a. Motivation

We now turn to an alternative strategy: replacing the solid core with a thin-film photoconducting structure (Figure III-1(c)). A striking advantage of the new thin-film structure compared to its solid-core counterpart is the significant reduction of I_{dark} and hence device noise per unit length, as exemplified in Figure III-8.(a), where i_N of the solid-core and thin-film fibers (both having the same diameter d) are plotted as a function of L. The drop in I_{dark} for a thin-film structure results from removal of most of the bulk of the glass contributing to I_{dark} in the solid-core case. On the other hand, I_{ph}-I_{dark} remains the *same* in both structures if the film thickness exceeds a few penetration depths at the illumination wavelength. For the thin-film structure, I_{ph} is given by a simple formula:

$$I_{ph} - I_{dark} \propto T \cdot E \cdot (1 - e^{-t/\delta})$$

(III-14)

where T represents the fraction of externally incident photons that reach the thin film, t the film thickness, δ the penetration depth, and E the electric field intensity. The third term in Equation 1 is proportional to the fraction of photons reaching the thin film that generate photocharges within it. We have assumed a uniform field throughout the thin film, an assumption we have found to be valid over the range of considered thicknesses using our computational model. Also, we neglected optical resonance since the reflection at the interface between the glass and the polymer is negligible, around 7% (considering index of refractions of 3.0 and 1.7 for the glass and the polymer respectively).

III.5.b. Scaling laws of thin-film fiber devices

In order to study the effect of the film thickness on the performance of this new structure, we fabricated four preforms having identical dimensions and structures while only varying the thickness of the incorporated thin film. The preforms were drawn down by the same reduction factor resulting in final film thicknesses of 120, 240, 360 and 480 nm. In Figure III-8.(b) we show SEM micrographs of thin-film devices with t = 120 nm and t = 360 nm. These micrographs demonstrate the precise control over the thickness of sub-micrometer-thick photodetecting films spanning the entire fiber length. We find that the dependence of I_{ph}-I_{dark} on t (Figure III-8.(c)) follows closely the expected form given $1 - e^{-t/\delta}$ in Equation III-14. A notable exception is I_{ph} for the thinnest film (120 nm) at the shorter wavelength. We believe that this loss of responsivity (i.e., photocurrent for a given amount of incident light energy) is due to surface roughness, which becomes more pronounced as the feature sizes are reduced and the film thickness becomes comparable to the penetration depth. Surface roughness reduces the photocurrent since most of the free carriers in this case have lower drift mobility. This is corroborated by the observation that the responsivity of thin-film devices is smaller (by a factor of 2 to 3) than solid-core structures of similar glass composition. In addition to surface roughness we believe that the thin-film composition is more inhomogeneous than the bulk glass due to dissociation during evaporation and rapid cooling under vacuum conditions [54,56]. This leads to an increase in disorder and the density of localized states in the band tail, further reducing the free-carrier average drift mobility [28,44]. From Figure III-8. we see that increasing the film thickness increases $I_{ph} - I_{dark} \propto 1 - e^{-t/\delta}$ and $i_N \propto \sqrt{t}$. It is then possible to engineer the material (δ) and the film thickness t to maximize the sensitivity $s \propto \left(1 - e^{-t/\delta}\right)/\sqrt{t}$ of the device at a given wavelength. For an illumination at 674 nm, corresponding to $\delta(\lambda = 674$ nm$) = 150$ nm, this function is maximal for a film thickness of 240 nm. This extra independent degree of freedom in the fiber structural design is of significant advantage for applications where one is constrained in terms of the fiber external dimensions (d and L).
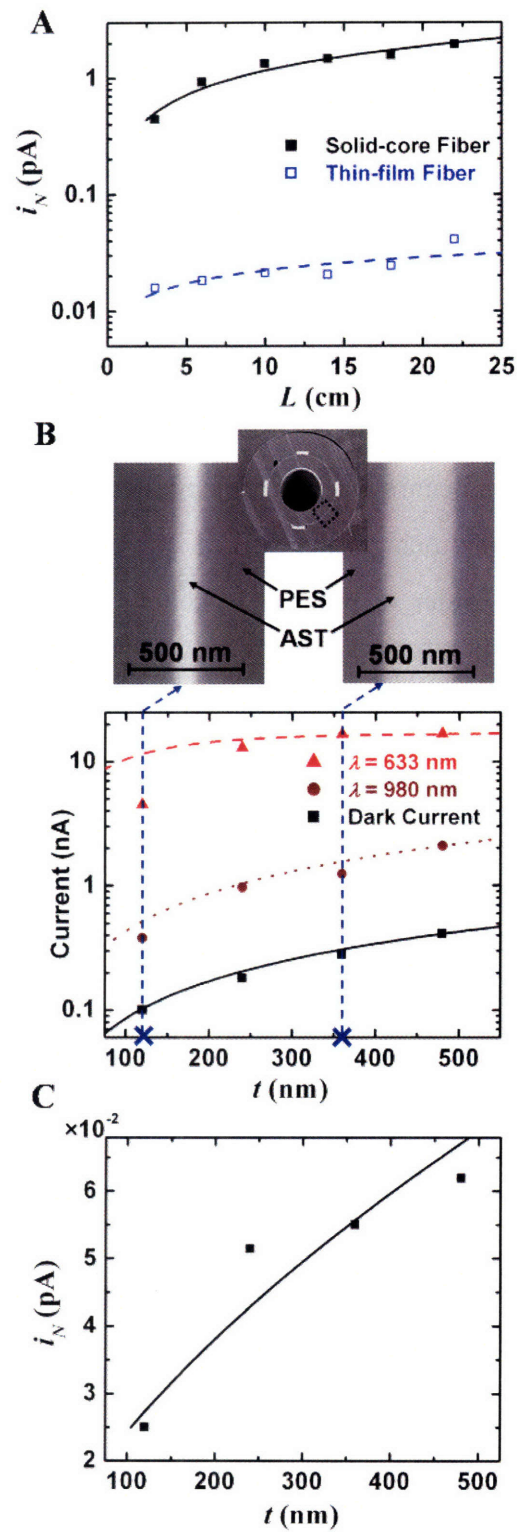
Figure III-8.. Scaling trends for thin-film fiber devices. (a) Comparison of the dependence of the noise current of solid-core and thin-film fiber devices having the same diameter. (b) SEM micrographs of the thin-film devices having thicknesses of 120 and 360 nm showing. Below: Dependence of the dark current and photocurrent (at two wavelengths) on thin-film thickness t. (c) Dependence of the noise current on *t*.

III.5.c. Comparing solid-core and thin-film structures

Figure III-9, in which the spectral dependences of the sensitivity for solid-core and thin-film fiber devices are contrasted, summarizes many features discussed in this study. In the solid-core case, s is relatively constant over a very wide spectral range (and hence penetration depths) with two notable exceptions. At small penetration depth (short wavelength), light is absorbed close to the surface of the core where the electric field is higher, leading to an increase in I_{ph} and hence s. A drop in s occurs at very large penetration depth (long wavelength) when δ becomes comparable to the diameter d. In the thin-film case, a drop in s occurs when the thickness t becomes comparable to δ since a large fraction of incident photons go unabsorbed. Nevertheless, thin-film fibers have a sensitivity of more than an order of magnitude better than solid-core fibers at shorter penetration depths. The judicious choice of materials, structure, and dimensions can hence lead to significant improvement in device performance for a given application.
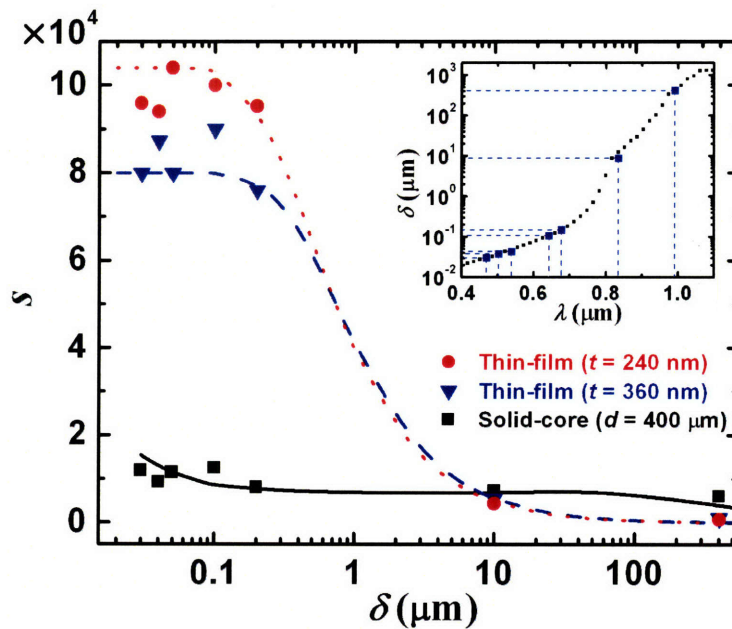
Figure III-9. Comparison of the sensitivity s for solid-core and thin-film fiber devices as a function of penetration depth of the incident radiation, or equivalently the radiation wavelength (the inset shows the dependence of the penetration depth on wavelength for the amorphous semiconducting glass used in this paper).

We also compared the rise and decay time of two $As_{40}Se_{54}Te_6$ device fibers, one with a solid-core and the other with an initial 9 micrometer thick film. Both fibers were illuminated by a white light source, and the drop of potential due to the decrease of resistance of the fiber was amplified and recorded with an oscilloscope. The results are reported in Figure III-10, in which the blue and red curves represent the core and thin-film fibers, respectively. As can be seen, the thin-film fiber has a faster response. As we discussed earlier, the initial drop of current as the light is switched off is due to the trapping of charges that were in extended states. If, as we assumed, the thermal evaporation as well as the surface roughness are responsible for more localized states in the semiconductor in thin-film form, the carrier lifetime is reduced, and the drop of photocurrent is faster. Hence, the thin-film device exhibits faster responses.
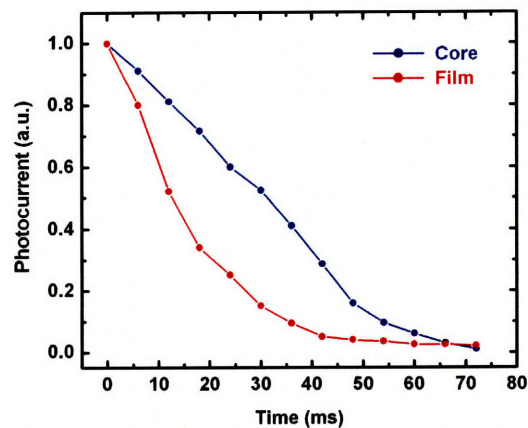
Figure III-10. Decay time of photocurrent for core and thin film $As_{40}Se_{54}Te_6$ fibers, blue and red respectively.

To give an idea of the performance of such fiber devices, the Noise Equivalent Power (NEP), which is the illuminating power for which the sensitivity is equal to one [41,42] was measured to be of approximately 25 $nW.cm^{-1/2}$ for a fiber with film thickness of 240 nm illuminated at 674 nm, more than an order of magnitude lower than that of its solid-core-fiber counterpart. Note also that other structural modifications such as the addition of electrodes, the reduction of their spacing, the addition of anti-reflective coatings, packaging of multiple photodetecting elements into a single fiber, post-drawing crystallization of the amorphous semiconductor, and the use of higher voltage bias can significantly improve the device performance. Nevertheless, the scaling effects are

independent of both the type of glass used and the type of improvements listed above, which make the conclusions drawn in this study for both the solid-core and the thin-film structures general and robust.

The improvement in performance of the new photodetecting thin-film structure allows us to extend the range of fiber-based-device applications. The large-area fiber-webs constructed of solid-core fibers used as large interacting screens or in lens-less imaging systems are intriguing applications of photodetecting fiber-devices [17,18,30] The low sensitivity of these fibers necessitated the use of high incident optical power, 1.5W in the case of the lensless imaging system to reconstruct an image from an illuminated object [30]. A grid of the same size constructed of higher-sensitivity thin-film fibers could perform the same task with incident power lower than 100mW, which can be provided by a simple laser diode. Moreover, these large interactive screens, or even functional fabrics, could respond to even weaker light sources such as laser pointers, making them useful for real-world applications. Our study also has striking implications with respect to the increase of fiber-web size that is possible when using thin-film devices, while maintaining the same sensitivity performance of previously published arrays. Since the sensitivity is inversely proportional to $\sqrt{L}$, a 100-m long thin-film fiber can detect a light beam with the same sensitivity as a one-meter long solid-core fiber if a modest ten-fold improvement in sensitivity is achieved. This means that if we could cover a 1-m^2 photodetecting area with a required level of sensitivity with our previously reported solid-core fiber grid, we can now build a thin-film-fiber grid with a 10000 m^2 of photodetecting area, while maintaining the same sensitivity.

In addition to the increase in performance, the thin-film structure enables us to envision new applications with enhanced functionalities. We present in the next section an application in which we use the hollow core of the fiber as a receptacle for a chemically sensitive material. The presence of certain molecules interacting with this material generates light inside the fiber core that is captured by the surrounding semiconducting film in the fiber.

III.5.d. Application: fiber-based TATP sensor

The large number of potential explosives used by terrorist organizations worldwide has prompted an intense joint development effort at Nomadics, Inc. (Oklahoma, OK) and MIT of emission-based sensing materials for detection of peroxides, to compliment Nomadics's mature TNT-detecting materials. The goal of the collaboration is to develop an integrated fiber-sensor platform for the detection of both liquid and solid peroxides explosives including hydrogen peroxide, TATP and HMTD. The active sensing elements of the device will be comprised of the new multimaterial and multifunctional fiber devices coated internally with novel transduction materials that have shown extreme sensitivity to peroxide vapor. We envision fiber devices as stand-alone, remote, disposable probes that can be sent into harsh or dangerous environments. The resulting fiber devices are intended to engender unprecedented sensitivities from Nomadics optical detection materials while enabling a more versatile, agile detection device. Importantly, the strong, flexible fibers allow applications of Nomadics vapor phase detection technologies that are currently inaccessible with the existing explosives detecting device, FidoXT™. Coupling multifunctional fibers with Nomadics sensing materials through this development effort is expected to result in inexpensive, disposable probes for ultrasensitive peroxide detection. We expect this sensing technology to serve as a platform for a comprehensive detection system for emerging peroxide threats.

Here we focus on efforts made to develop TATP-sensitive fiber based devices. Specifically, we want to use the hollow core of a thin-film photodetecting fiber as a host for ultra-sensitive chemiluminescent (CL) transduction materials. These materials indicate the presence of suspect vapors emanating from liquid or solid peroxide explosives. In the usual system, shown on Figure III-11, the CL mix is coated on the inner wall of a capillary tube. The hydrogen peroxide vapors sucked into the tube react with the CL mix to produce visible light that is then detected by a power meter placed at the end of the capillary tube. In order to improve guidance of the signal to the detector, the use of PBG fiber is investigated. However, here, instead of relying on guidance of the light inside the core of a PBG fiber to an external detector, we use the unique cylindrical profile of the fiber photodetector to increase the capture efficiency of emitted photons by
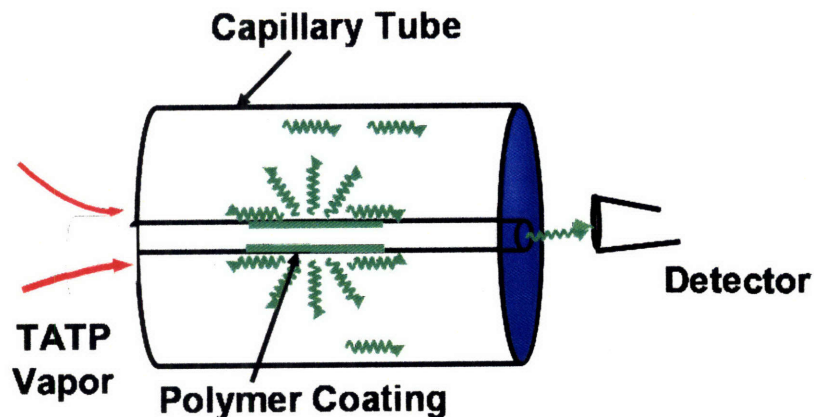
Figure III-11. Schematic of a TATP detection system. The inner wall of a capillary tube is coated by a chemiluminescent (CL) material specifically sensitive to TATP. TATP vapor is sucked inside the hollow core. Light generated is detected at the end of the tube by an optical detector.

the surrounding sensing materials. The light signal is captured "on the spot" and converted into an electrical signal. With this novel design, the signal indicating the presence of a threat is contained in photons that travel back to the distant user through the low-loss and reliable electrical guidance mechanism. This will potentially increase the efficiency, resulting in lower detection limits for the wide range of peroxide-based threats that currently exist. Furthermore, the simplicity of instrumentation required to support these fiber sensors (a battery-operated ammeter with wireless transmission capabilities) will enable their widespread placement as autonomous sensors.

Proof-of-principle of fiber-based peroxide detection is presented in Figure III-12. The results were obtained using a thin-film fiber device with a simple structure similar to the one shown in Figure III-1. On top of the 4 (or 6) electrodes contacting a semiconducting layer ($As_{40}Se_{54}Te_6$ in that case), the fiber inner core is coated with a ultra-sensitive CL transduction layer specifically sensitive to TATP. Fibers were sealed to a vapor stream of hydrogen peroxide. Upon exposure to peroxide, we rapidly registered an increase in current compared to that measured in an identical, uncoated fiber. Rapid sensor recovery was also demonstrated when vapor stream was turned off. This recovery would be significantly expedited by a clean air flow through the fiber that will be implemented in future generations of our vapor delivery system. Optimization is still underway at both Nomadics and at MIT. The fiber structure and materials, both the

photodetecting layer and the polymer cladding, are being investigated, as well as a reliable vapor delivery system that will enable the precise quantification of the sensitivity of the fiber. Nevertheless, these early results represent a striking example of applications for thin-film fiber devices and demonstrate the first photodetecting fiber-based explosive detector.
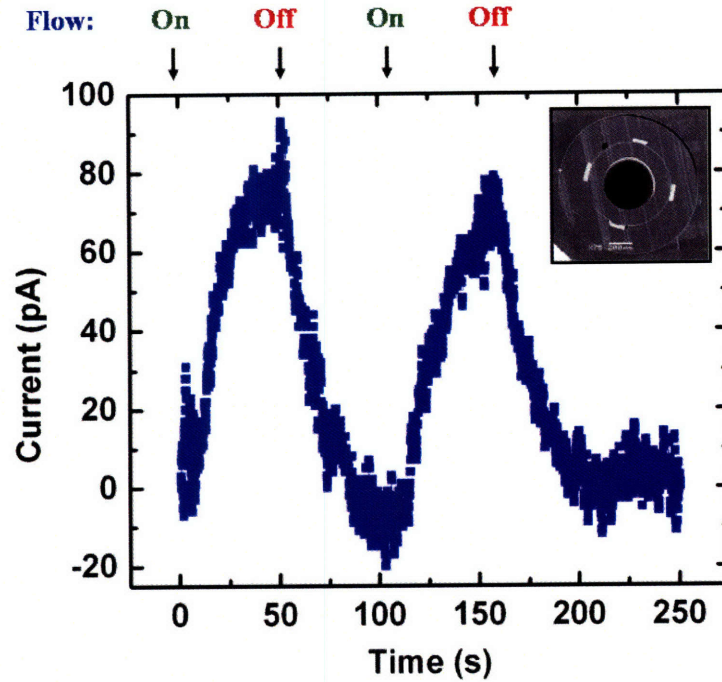
Figure III-12. Photocurrent versus time for a thin-film photodetecting fiber device whose inner wall is coated with a CL TATP sensitive film. An increase in current is the sign that light was generated as the flow of hydrogen peroxide is on and molecules react with the CL material. Rapid recovery is observed as the flow is turned off.

Thin-film structures have other significant characteristics. In the next chapter, we will address one very important characteristic, which is their ability to be densely packed into a single fiber. While passive structures (such as external Bragg mirrors [17]) may be incorporated into solid-core fibers, the addition of other photodetecting devices into the same fiber cannot be achieved in a straightforward fashion. Our novel fiber device structure paves the way to the integration of multiple devices into a single multifunctional fiber.

IV. Integrated Fiber Devices

IV.1.   Motivation

The development of semiconductors technology has been for the most part the result of the reduction of device feature size, enabled by continuous improvements in thin film processing. Achieving smaller sizes not only enables an increase in the device packing density, but is also crucial for the functionality, efficiency and design of complex devices [3-5]. Multimaterial integrated fiber devices produced by simple and inexpensive fiber drawing techniques and recently proven to exhibit many of the semiconductor devices functionalities, follow the same trend. We recently demonstrated that the reduction of cross sectional sizes and the design and controlled processing of thin film structures inside fiber devices significantly increase their performance. This study had significant practical implications in the optimal design of photodetecting fibers to be used in applications such as remote sensing, large-area optical-detection array systems, and functional fabrics. In this chapter, we study how this new thin-film design can be used to also increase the device density integrated in a single fiber and what practical consequences this has in terms of fiber functionalities. In Figure IV-1(a,b) we show Scanning Electron Microscope (SEM) pictures of core and thin-film photodetecting fibers reported in previous publications [17-20], where we have insisted on the extension along one dimension characteristic of these fiber devices that brings significant advantages, besides their low cost and ease of production, for different applications. We are however yet to investigate the use and resources of the angular and radial dimensions of the fiber devices. The objectives of this chapter is then three folds: (1) Demonstrate the controlled fabrication of multimaterial fiber devices with new structures where two thin films are integrated at prescribed radial positions and contacted by electrodes placed at prescribed angular positions, as depicted in Figure IV-1(c,d); (2) show that these new fibers enable not only the detection of a light beam, but also its direction and frequency; (3) finally, we build a fiber grid with these new fibers which enables significant improvements to the lensless imaging system previously reported [30].
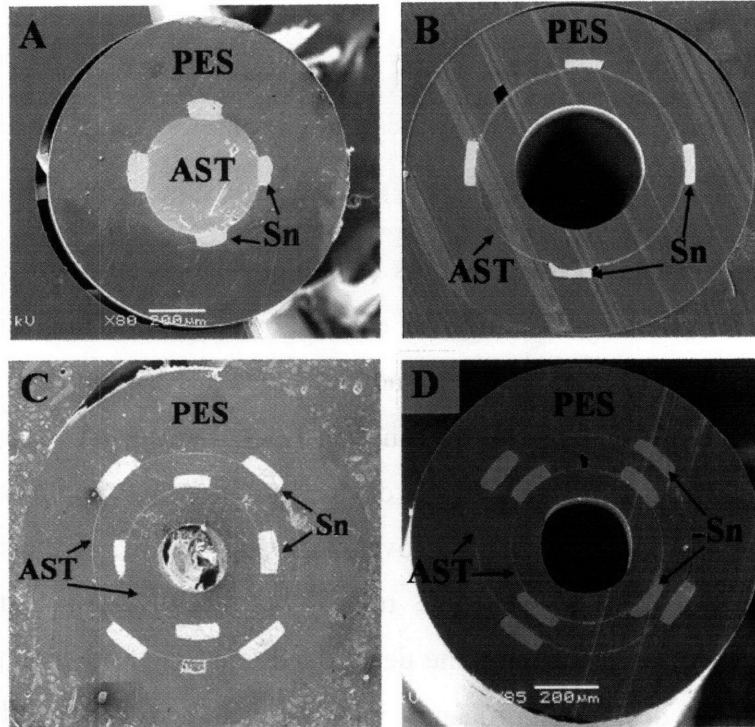
Figure IV-1. SEM pictures of the cross section of different multimaterial fiber devices. All fiber has PES polymer support, $As_{40}Se_{54}Te_6$ (AST) as a semiconducting glass and Sn electrodes. (a) Core fiber; (b) Thin-film fiber. (c) Dual fiber with the four electrodes of the external layer rotated by 90^0 with respect to the electrodes of the inner layer. (d) Dual fiber with aligned electrodes.

IV.2. Angular resolution

IV.2.a. On the symmetry of the current system

So far it was the response of fibers integrated into specific assemblies that enabled the reconstruction of the location and direction of an incoming beam [30]. Each fiber alone contained no knowledge about these characteristics due to the symmetry of both their structure and the electric field distribution inside them. Indeed, in our previous configuration where two opposed electrodes are grounded and the two others brought to a same potential (V), as represented in the first schematic of Figure IV-2(a), the electric field E_k in each of the four quadrants labeled by k ($1 \leq k \leq 4$) is the same. When light is impingent on a fiber however, a unique set of four numbers (Δn_k, $1 \leq k \leq 4$) which represent the number of free charges generated in each quadrant is uniquely related to the angle of illumination θ of the incoming beam. The total photo-current generated is the sum of the

four photo-currents induced in between the electrodes: $\Delta I = \sum_{k=1}^{4} \Delta i_k$ where $\Delta i_k \propto \Delta n_k E_k$.

Since the E_k are all equal when the four electrodes are contacted, $\Delta I \propto \Delta nE$ where Δn is the total amount of charges generated in the film. These quantities are all independent of θ and so the fiber can not distinguish between the different directions of illumination. As we mentioned, going from a single one dimensional fiber to a two dimensional fiber array has enabled us to localize a point of illumination, but an uncertainty in this case remains for the direction of the incoming light. One way to go around this problem is to put two arrays one after another as we described above. But even this way, there is still a two-fold degeneracy for the direction of the incoming beam. We propose here a way to break the symmetry in the fiber, and have the fiber respond differently as the light touches it from different angles.

IV.2.b. A first approach: quad photodetector

Our first approach is to apply a voltage of opposite sign to the two ungrounded electrodes as shown in Figure IV-2 (b). If the fiber has a semiconductor core, then a high field will be applied across the core of the fiber, and the light, absorbed at the surface, won't really affect the overall current read. On the other hand, when the same configuration is used but with a thin film, the current is forced to circulate in the "channels" formed by the thin film in between a very low conductivity polymer between the electrodes. In such a configuration, from the positive electrode to the two grounded ones, positive current is flowing, whereas from the negative electrode, a negative current flows. The total current measured in the external circuit can then be written as:

$$I = \sum_{k=1}^{4} i_k \qquad \text{(IV-1)}$$

$$= V_+(G_1 + G_4) + V_-(G_2 + G_3)$$

where the G_k are the electrical conductivities of each channel. If the fiber is perfectly symmetric, then $G_k = G$ for $1 \le k \le 4$, and one can easily see that when we apply a voltage such that $V_+ = -V_- = V$ the overall current going through the ground equals zero.

If now a light is incident on the "positive side" of the fiber, meaning on the electrode that has a positive potential applied to, as described Figure IV-2 (b), more light is absorbed on this part of the thin film and the conductivity of the positive side increases, making the overall photocurrent measured through the ground positive:

$$\Delta I = V(\Delta G_+ - \Delta G_-) \text{ and } \Delta G_+ < \Delta G_- \Rightarrow \Delta I > 0$$

Similarly, a negative current going through the ground is measured if the light hits the negative size of the fiber. By applying these two different voltages and taking advantage of the thin film geometry, we are able to break the device symmetry, and create a *fiber that can distinguish its right from its left.* In Figure IV-2(c), we have measured the current for different angles of illumination. We can clearly see the two regions where the current is positive and negative, each of length π. The theoretical curve drawn on the graph follows a simple description of what is happening as the degree of illumination changes: if we start by illuminating the positive electrode with a zero angle, the light will mostly see the positive side of the fiber and a maximum positive current I_+ is obtained. (Similarly if we were to illuminate directly the negative side (I_-)). As we rotate the fiber of an angle θ, the light hits the positive side only on a portion $(\pi - \theta)\dfrac{d}{2}$, and hits the negative side on a portion $\theta\dfrac{d}{2}$, so the current measured goes as:

$$I(\theta) = \frac{1}{\pi\dfrac{d}{2}}\left(\int\limits_0^{\pi-\theta} \Phi(\theta)d\theta\frac{d}{2}I_+ + \int\limits_{\pi-\theta}^{\pi} \Phi(\theta)d\theta\frac{d}{2}I_- \right) \qquad (IV\text{-}2)$$

where $\Phi(\theta)$ was derived as explained above, and we need to weight each contribution with the value of the light intensity absorbs, that is a function of the angle as we saw earlier. For a symmetrical fiber, we should have $I_+ = -I_- = I_{max}$.

In Figure IV-2c, we show the theoretical curve in blue where we calculated the light distribution on the film surface, and integrated the different parts accordingly. The experimental points show in red prove a very good agreement with the model of light absorption we used, and clearly show the transition between a positive and a negative current as we rotate the fiber by π.
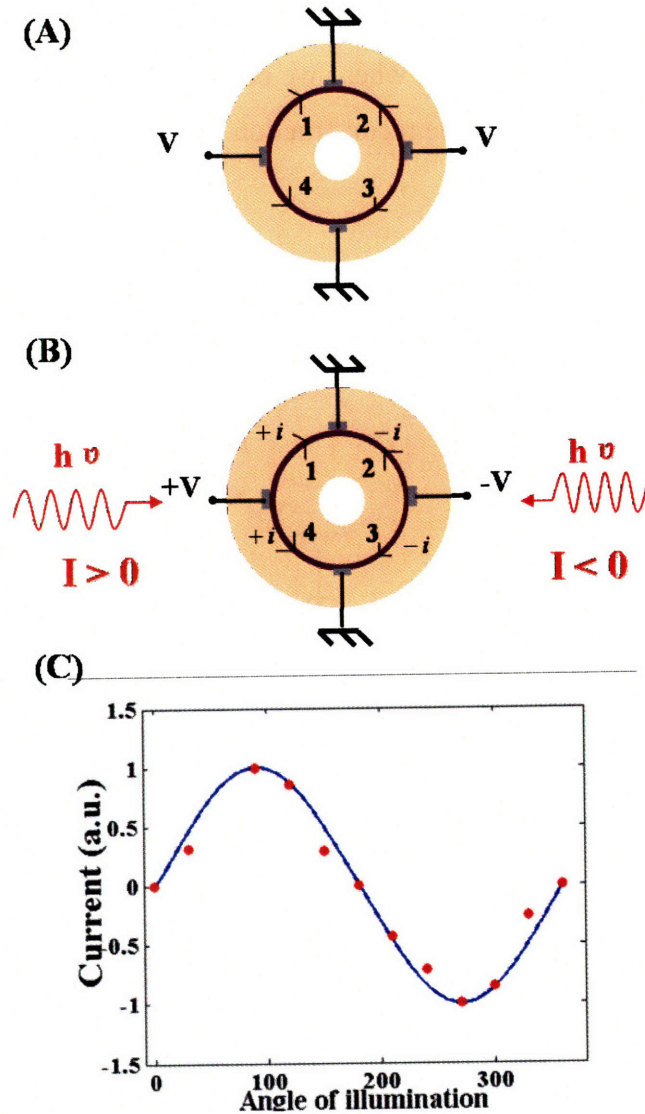
Figure IV-2. (a) Schematic of thin-film fiber with the four quadrant represented. (b) Same schematic with opposite voltages applied and the current directions represented. When light is impingent from the left, a positive photocurrent is observed as shown on (c) where is plotted the theoretical (line) and experimental data (point) of the photocurrent measured for different angles of illumination.

If now we construct a fiber that has two thin films independently connected to an external circuit, every light that is not absorbed entirely in the first film will reach the second, and generate a current. By rotating the application of the voltages, as shown in Figure IV-3(a), we see that each film can distinguish, between two directions of illumination. By looking at the sign of both photo-generated current, one can distinguish up to four directions of illumination. This leads to the first single device *Quad photoconductor*. Such a structure was successfully constructed and tested as can be seen

in Figure IV-3(a). White light from a Tungsten lamp was used as the illuminating source. Results are presented Figure IV-3(b) where we can clearly see the $\pi/2$ shift between the inner and outer layer that enables the reconstruction of four directions of illumination.
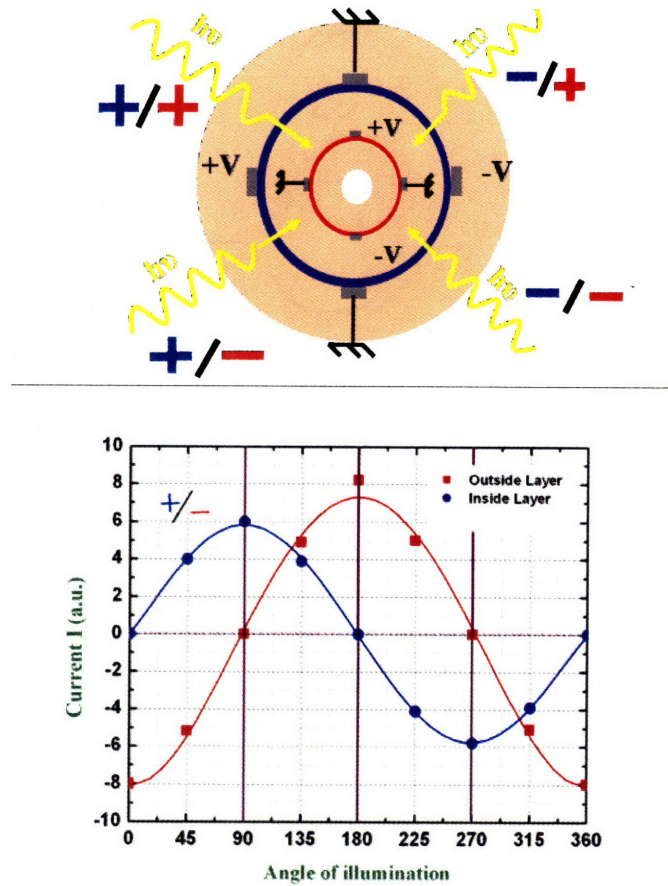
Figure IV-3. (a) Schematic principle of the quad photodetector, with the indicated different signs of currents corresponding to the different portions of thin film illuminated. (b) Experimental results (dots) and theoretical curves (lines) derived in the text, for the 2 layers.

Breaking the symmetry of the system through the applied voltage constitutes one way of improving the "vision" capability of the fiber device. The next section shows how to improve further the angular resolution by breaking the fiber device into multiple embedded photodetectors.

IV.2.c. Increasing the angular resolution

Our approach is here to treat each quadrant as an independent detector by applying a voltage only between two adjacent electrodes at a time as depicted on the 2 schematics of Figure IV-4(a1). It is then possible to synchronize a multiplexer, given the response speed of the device typically of a few milliseconds, to scan and collect the currents at each quadrant. When the potential is applied this way, the symmetry is obviously broken and the current acts as follow. On the schematics where the applied potential is represented in red on Figure IV-4, the electric field in quadrant 1 is stronger than in the three other quadrants. When light is incident with a zero angle, most of the photons are absorbed in 1 which generates a higher current than when light is incident at $\pm180°$ for which the photons are absorbed in the low electric field region (quadrants 2, 3 and 4). This gives rise to the angular dependence of the photo-current apparent on Figure IV-4(a2). There, the theoretical curve was derived by computing the amount of light absorbed in each quadrant for a given angle of illumination. When we rotate the application of the voltage to different electrodes, the dependence of the photo-current on θ is shifted accordingly by $90°$ for adjacent quadrants. An illumination event is then now characterized by a set of four current measurements that is related uniquely to θ.

The angular resolution of such a system is not easy to evaluate since it is a function of the light intensity. Indeed, this resolution is limited by the noise, both dark current (or background) and photo-current noise, which increases with light intensity [41,42]. It is also directly related to the slope of the change of photo-currents with respect to θ in each quadrant, which is a function of the structure in the fiber. To understand the system better, we can first look at two limiting cases where the power of illumination is equal to the NEP of the system, and secondly where it is large enough so that the noise is dominated by the photo-current fluctuations. Note first that the NEP of the system is defined a bit differently. It is sufficient to have a level of power incident on the fiber that generates a photo-current above the noise level in only one of the four quadrant. This photo-current follows the curves of the maximum of current between the four devices for all angles. Hence the NEP is given by: $\min_{-\pi \leq \theta \leq \pi} \left[\max_{1 \leq k \leq 4} (I_k(\theta)) \right] = \max_{1 \leq k \leq 4} (i_{Nk}(\theta))$ where i_{Nk} is the noise level
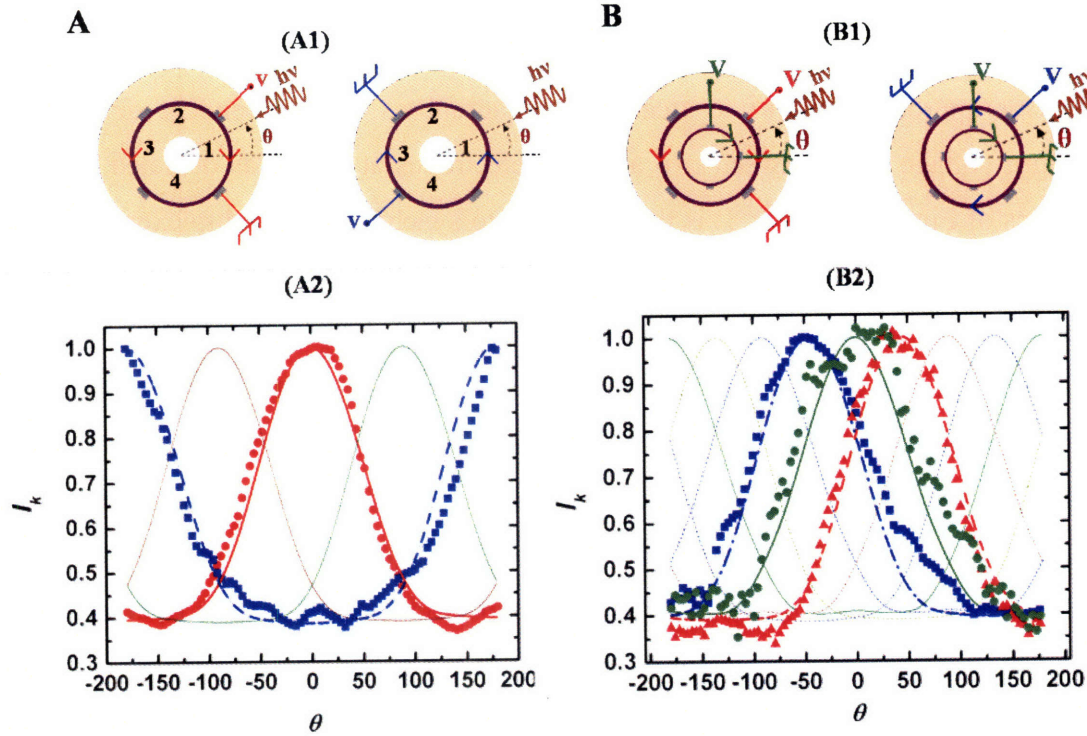
Figure IV-4. (a1) Schematics of thin-film fibers where, quadrant 1 (left) and quadrant 3 (right) are contacted, the number labeling the 4 quadrants. (a2) Dependence of photocurrents on θ when contacts are made like in the schematics in (a1): red curve (theoretical model) and dots (experimental results) for quadrant 1 blue for quadrant 3. (b1): Schematics of dual ring fibers with rotated application of potential on the external thin-film. (b2): Dependence of photocurrents on θ when contacts are made like in the schematics in (b1)

of quadrant k. Since the photocurrent is very low compared to the dark current it doesn't generate more noise than the dark current itself and so all the i_{Nk} are equal to i_N. Now if the power absorbed by the fiber is just equal to the NEP, the photocurrent is picked up only by one quadrant, unless we are exactly in between 2 quadrants (angles -135, -45, +45 and +135 on Figure IV-4). One quickly realizes that unless at these limiting cases, a maximum resolution of 90^0 is obtained.

When the illuminating power becomes larger, the change of photo-current with incident angle θ starts to be higher than the noise and the angular resolution increases. Indeed, let us assume first that the incident power (or number of photons per unit time N) is known and that the photo-current generated is still low enough so that the fluctuations in each quadrant is dominated by the dark current fluctuations i_N. Then two angles of illumination separated by $\Delta\theta$ will be resolved if:

$$\Delta\theta \geq \frac{i_N}{I_1(0)}\left[\min_{-\pi \leq \varpi \leq \pi}\left(\max_{1 \leq k \leq 4}\left(\frac{dF_k(\theta)}{d\theta}\right)\right)\right]^{-1}$$ (IV-3)

where F_k is the function plotted on Figure IV-4 of the change of current of quadrant k with respect to θ. $I_1(0)$, the current generated in quadrant 1 for an illumination ot zero angle, is known because proportional to a constant A, the same for all quadrant, that is material and structure dependent, and to N, the total number of incident photons. In Figure IV-5(a) we plotted the maximum derivative of the F_k as a function of the angle for 1 and 2 layers. Typical values of noise measured were around 0.1 pA for 15 cm long fibers. For an illumination generating 1 pA (typical dark current being 100 pA) we obtain a resolution of 17°. It goes below 4° as we increase by an order of magnitude the illuminating power.

The advantage of having two layers is here striking. Indeed the angle for which the resolution is the lowest is at 0° (and other angles shifted by 45°). When we have two layers, eight quadrants are considered all similar as the previous four ones but shifted by only 45° this time. Higher slopes are then obtained at 0° for example from the inner layer by a ratio of 1.3 as apparent on Figure IV-5(a). This increases by the same amount the resolution obtained. As we increase the incident power, fluctuations of the photo-current adds to the background noise and the situation is more complicated. We can note though that $I_1(0)$ will increase proportionally to N while i_N goes with $\sqrt{N}$ in a simple noise picture [41,42]. We can then obtain in theory arbitrary small angular resolutions as the incoming light power increases. In Figure IV-5(b) we plotted experimental data and the Gaussian fit as on Figure III-2 for two angles of illumination separated by four degrees. The photo-current was much larger than the dark current and the noise associated to it can be taken to be from photo-current fluctuations only. The variance is roughly 30 pA for a current of 3.9 nA. This leads to an angular resolution of below 4° as apparent on the graph.

Now that we have the intuition of how angular resolution can be rendered quite small, let us look in more details what would happen in a real measurements where N is also an unknown. For an illumination event with sufficient power, we can immediately

find from which quarter light is from simply by looking at $\max_{1 \leq k \leq 4}(I_k(\theta))$, let us say

quadrant 1. We can then refine this angle resolution by looking at maximum current

between the two adjacent quadrants of 1, namely 2 and 4. We already have a 45^0
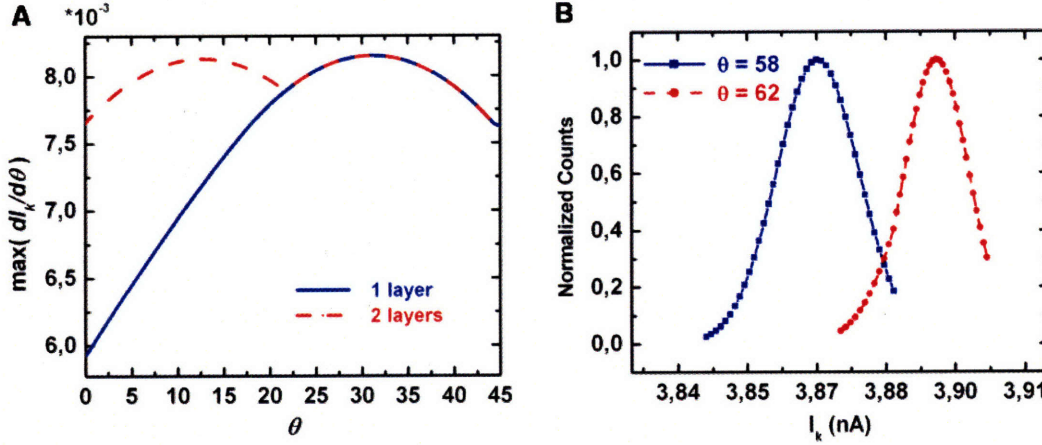
Figure IV-5: (a) Maximum of the four derivative of I_k as a function of the angle of illumination. (b) Number of counts versus current value for a fiber illuminated at two angles of illumination.

resolution using this technique. Higher resolution can be obtained though because more

information is contained in the ratio of the two maximum currents (in quadrant 1 and let

us say 2). Indeed, by taking the ratio of the currents we eliminate the unknown N and we

project the measured currents on the plots of Figure IV-4. Averages photo-currents I_1 and

I_2 have fluctuations i_1 and i_2 associated to them which fits well a Gaussian like

distribution and are independent. The ratio $R = I_1 / I_2$, independent of N, as a

consequence also has fluctuations $r(N,\theta)$ associated to it. Similarly to above, the angular

resolution criteria we set for the fiber device is then simply the following: two beams of

incoming angles θ_a and θ_b will be separated if the change in $R(\theta)$ is larger than its

fluctuations r. In mathematical terms, this gives:

$$R(\theta_2) - R(\theta_1) \geq r \text{ or } \frac{dR}{d\theta}\Delta\theta \geq r \text{ , which leads to the angular resolution } \gamma:$$

$$\gamma = \max_{N,\theta}\left[r(N,\theta)\left(\frac{dR}{d\theta}\right)^{-1} \right] \qquad (IV-4)$$

The distribution obtained form the ratio of two independent Gaussian like distributions with mean I_k and variance i_k is a complicated mathematical object [57]. We take hear a much simpler approach to get a physical insight on the behavior of r and the angular resolution of our system. To do so, we can look at the largest deviation from the mean value of R:

$$R = \frac{I_1 + i_1}{I_2 - i_2} \approx R + \frac{i_2}{I_2}\left(\frac{i_1}{i_2} + R\right)$$ at first order in i_k / I_k (remember that we are in the case of

large incident power). We can then take for r:

$$r(\theta) = \frac{i_2}{I_2}\left(\frac{i_1}{i_2} + R\right)$$

This is simplified in the case of small signal where the photo-current is much larger than the dark noise but the noise is still dominated by the dark current. In this case:

$$\gamma = \frac{i_N}{I_1(0)}\max_\theta(\varphi(\theta)) \text{ with } \varphi(\theta) = \frac{R+1}{F_2(\theta)}\left(\frac{dR}{d\theta}\right)^{-1} \qquad \text{(IV-5)}$$

The form of the angular resolution is very similar as previously. Only the function $\varphi(\theta)$ changed. Since we considered an extreme case to simplify the mathematical treatment, we end up with a larger coefficient than previously reported. However, resolutions of the order of $4°$ can be achieved at reasonable power of illumination.

Let us study now how we can use integrated fiber devices to get knowledge on yet an other characteristic of an incoming beam, its frequency.

IV.3. Spectral resolution

A light beam, besides its direction and location, is also characterized by its wavelength and its intensity. The intensity is given by the number of photons per unit of time and area, times the energy of a single photon $h\nu$, where h is the Planck constant and ν the frequency related to the wavelength (λ) through the formula $\nu = c/\lambda$, c being the speed of light. We neglect here the effect of polarization which has been observed to be negligible. In this section we demonstrate a way to enable a photodetecting fiber device to recognize the wavelength of the monochromatic beam impingent on it.

IV.3.a. Principle

As we discussed earlier, upon illumination, a semiconducting thin film partially reflects, transmits and absorbs photons. A fraction η (quantum efficiency) of absorbed photons transfer their energy to electrons that get excited from the valence band (and localized states in the bandgap) to the conduction band [3,5,41,42]. The number of such transitions is characterized by the coefficient of absorption α (with unit the inverse of a length) that is wavelength dependent and is a function of the number of electrons in the valence band and in localized states, and the number of available states in the conduction band. For crystalline semiconductors the change of α with wavelength is sharp around the materials bandgap because below this energy photons aren't providing enough energy for the electrons to reach the conduction band. For amorphous semiconductors on the other hand, the high density of trapped electrons in localized states of broad energies in the gap results in "sub-bandgap" absorption and a smoother change of α with wavelength is observed.

The number of photons absorbed in an amorphous semiconducting film of thickness t illuminated perpendicularly by a monochromatic light of wavelength λ and penetration depth $\delta(\lambda)$ ($\delta = 1/\alpha$), neglecting any resonance effects in the film, is given by:

$$\Phi_a = T(1 - e^{-t/\delta})\Phi_i \qquad\qquad \text{(IV-6a)}$$

$$\Phi_t = T^2 e^{-t/\delta}\Phi_i \qquad\qquad \text{(IV-6b)}$$

where Φ_i, Φ_a and Φ_t are the incident, absorbed and transmitted number of photons per unit of time respectively and T is the translation coefficient between the film and surrounding medium (polymer in the case of fibers). The penetration depth is given by $\delta = \lambda / 4\pi k$ where k is the imaginary part of the index of refraction [3,5,41,42]. Note that we assume a quantum efficiency of one. In a layer where the electric field is uniform, and considering conduction by majority carriers only, the photocurrent is simply given by:

$$I_{ph} = e\mu\tau T(1 - e^{-t/\delta})\Phi_i E l \qquad\qquad \text{(IV-7)}$$

where e is the elementary charge, μ and τ are the average mobility and life time of majority carriers, E the electric field and l the film length.

Let us assume now a second film of the same material and of same thickness as depicted in Figure IV-6. We neglect absorption in the medium (polymer for example) in between the two films. The number of photons reaching the second film per unit of time is simply Φ_t. The photocurrent in this second film is then given by:

$$I_{ph}(2) = e\mu\tau T^3 e^{-t/\delta}(1-e^{-t/\delta})\Phi_i El \qquad \text{(IV-8)}$$
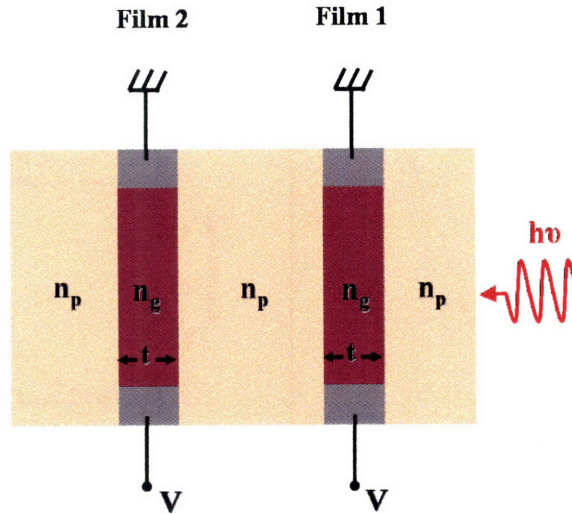
Figure IV-6. Schematic of a dual film planar device.

The ratio of the photocurrents generated in films 1 and 2 is then simply

$$R(\lambda) = \frac{I_{ph}(2)}{I_{ph}(1)} = T^2 e^{-t/\delta} \qquad \text{(IV-9)}$$

The function R is a function of wavelength only; it doesn't depend on the number of incoming photons. We plotted this theoretical function Figure IV-7 for different film thicknesses and different glasses ($As_{40}Se_{60}$ and $As_{40}Se_{54}Te_6$), neglecting the change of T with wavelength over the range of frequencies considered. The addition of tellurium shifts the optical gap towards longer wavelengths as one can see. It is clear from these graphs that the ratio of photocurrents can enable to recover the wavelength of the incident beam. This is possible over a certain range of wavelengths, the center and width of which depends on glass composition and film thickness. Note that the striking advantage of using amorphous semiconductors is that the absorption edge is not as sharp compared to their crystalline counterparts. There is a fairly smooth increase of penetration depth over

tens of nanometers in wavelength, over which the photo-current ratio goes from 0 to 1. In this band, wavelengths could be distinguished, with a resolution that depends on the sensitivity of the two embedded photoconducting devices. Note also that the incident light intensity can also be recovered once the wavelength is known and after proper calibration of the system by simply looking at the value of the photocurrent in the first film.
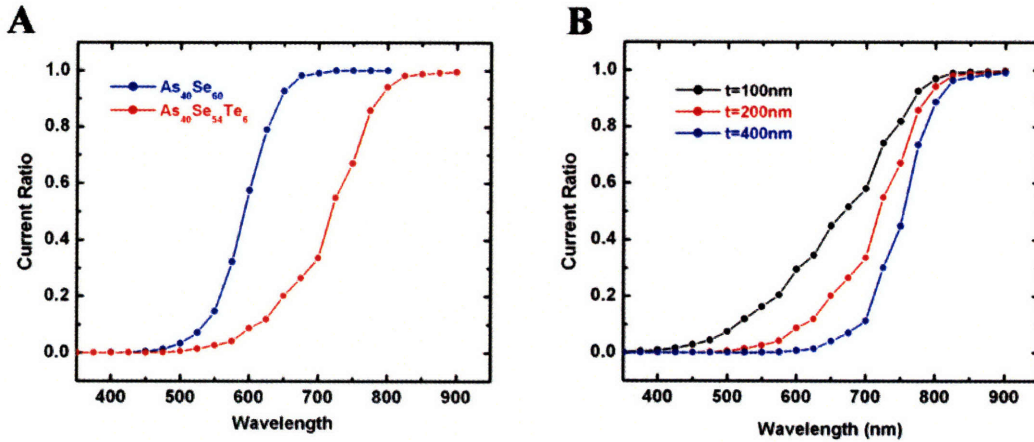
Figure IV-7. Theoretical curves of the photo-current ratio for two successive films of same thickness and different glasses (a) and same glass but different film thicknesses (b).

IV.3.b. Fiber-based device with spectral resolution

For light impingent on a fiber device, these findings still hold. Indeed, in a thin-film structure fiber, as we saw earlier, I_{ph} is given by a similar formula:

$$I_{ph} - I_{dark} \propto T N_{ph} E (1 - e^{-t/\delta}) \qquad \text{(IV-10)}$$

where T represents the fraction of externally incident photons that reach the thin film, N_{ph} the number of photons incident on the fiber, t the film thickness, δ the penetration depth, and E the electric field intensity. We have assumed a uniform field throughout the thin film, an approximation we have found valid over the range of considered thicknesses using our computational model. Equation (IV-10) tells us that when a monochromatic beam reaches the fiber, the two unknowns, the frequency ω and N_{ph} can not be determined by a single photo-current measurement.

The integration of a second film inside the fiber device as depicted in Figure IV-1(d) has the significant advantage to solve this problem and to bring spectral resolution to the fiber. The current in the inner layer is given by:

$$I_{2,ph} - I_{2,dark} \propto T_2 E_2 N_{ph} (1 - e^{-t_2/\delta_2}) e^{-t_1/\delta_1} \qquad \text{(IV-11)}$$

where the suffix $k = 1,2$ refers to the outer and inner film respectively, and the factor e^{-t_1/δ_1} represents the portion of photons unabsorbed in the first layer (we neglected losses in the polymer in between the two films). To simplify, we chose to produce fibers with two films of same thicknesses ($t_1 = t_2$) and same materials ($\forall \omega, \delta_1(\omega) = \delta_2(\omega)$). The ratio R (ω) of the measured currents in the inner layer to the current in the outer layer is again a bijective function of ω independent of N_{ph}:

$$R(\omega) \propto e^{-t/\delta(\omega)} \qquad \text{(IV-12)}$$

where the coefficient of proportionality is independent of ω.

In order to test this theory we fabricated dual ring fiber devices with different glasses used in the earlier simulations ($As_{40}Se_{54}Te_6$ and $As_{40}Se_{60}$) and different film thicknesses. We measured the photocurrent generated in both the inner and outer layer of each fiber by a Monochromator. A frequency range form 400 nm to 1000 nm, with steps of 20nm was used. On Figure IV-8 we show the measured ratio of current R for fibers with same glass composition ($As_{40}Se_{54}Te_6$) but different film thicknesses, and for fibers with same film thickness ($t = 520$nm), but different glass compositions. The spectral resolution of these fibers is clear. It is also apparent on these graphs that the fibers have spectral resolution only in a certain range of frequencies. The ratio R is indeed null when all the light is absorbed in the first layer (due to short penetration depth and/or thick layer), and becomes constant as the wavelength increases and the penetration depth is large enough so that the light absorption is proportional to t ($1 - e^{-t/\delta} \approx t/\delta$). Hence, two parameters influence this range of frequencies: the material through its optical bandgap and the value of $\delta(\lambda)$, and the layer thickness. A good example of the influence of the material is given here where the addition of tellurium shifts the optical gap towards longer wavelengths. This bandgap determines where the penetration depth will have a sharp increase. However the slope of $\delta(\lambda)$ doesn't change much from one material to the next. As apparent in Figure IV-8(a), the change of material only shifts the frequency

range of spectral resolution with respect to the optical bandgap and the according penetration depth of the material.
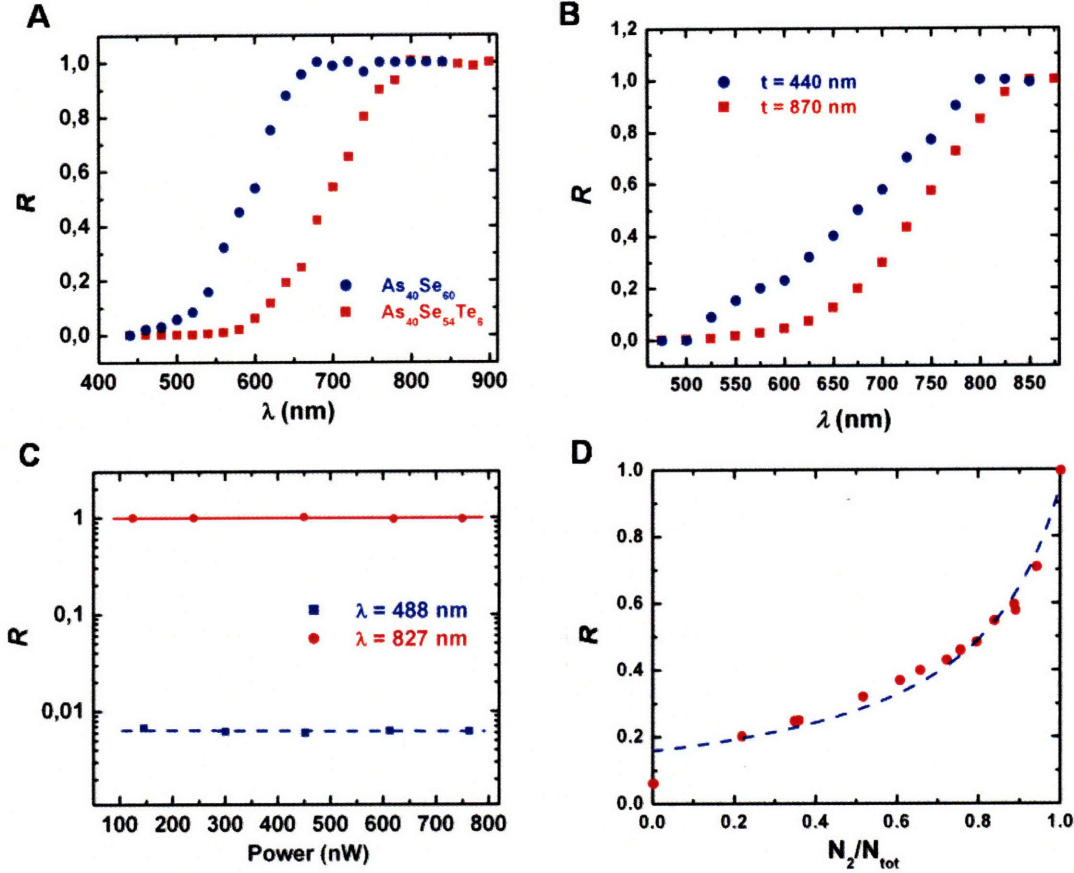
Figure IV-8. (a) Change of R with respect to λ for tow fibers with different glasses but same film thickness $t = 520$ nm. (b) Change of R with respect to λ for tow fibers with different film thicknesses but same glass $As_{40}Se_{54}Te_6$. (c) Change of R with incident power for two different thickness. (d) Change of R with respect to the ratio of the number of photons at 827 nm to the total number of photons (at 827 nm and 488 nm).

However, the film thickness seems to influence both the position of the frequency range and the slope of R. This remark is first supported by the observation that in Figure IV-8(a) the slope is the same for a same thickness layer while on (b) two films of different thicknesses have clearly R functions with disparate slopes and ranges of frequencies that can be separated. This becomes clearer if we look at the derivative of R with λ:

$$\frac{dR}{d\lambda}(t,\lambda) = \frac{1}{\delta(\lambda)^2} \frac{d\delta}{d\lambda} t e^{-t/\delta(\lambda)} \qquad \text{(IV-13)}$$

This function is maximum for a wavelength λ_0 and a thickness t_0 such that $t_0 = \delta(\lambda_0)$. This gives a criteria of thickness and material selection if the range of wavelength over which spectral resolution is desired is known. Another way to look at it more physical is that when t becomes larger, the range of wavelengths for which R is very small increases since more light is absorbed in the first layer. Since the penetration depth increases quite sharply after the bandgap, R reaches a value of 1 around a similar wavelength regardless of the film thickness. Indeed, the penetration depth is much longer than the thicknesses considered at this point. So the slope of R will have to be greater for a thicker film since it goes from 0 to 1 over a narrow band of wavelengths.

Another striking result is presented in Figure IV-8(c) where we illuminated a fiber with an $As_{40}Se_{54}Te_6$ glass with a thickness of 520 nm, at two different wavelengths, 488 nm (Argon laser) and 827 nm (laser diode), while varying the incident power. It is clear from these results that the ratio R is independent of the incoming power as predicted by our theoretical analysis. Finally, Figure IV-8(d) presents yet another significant feature of dual ring fibers. In this case, we illuminated the fiber *simultaneously* with these two previous frequencies while varying the ratio of red (827 nm) to blue (488 nm) photons. The ratio of current is plotted and shows that the relative power of the two incoming beams is uniquely related to R. This is due to the following reason: each beam is characterized by a number of photons and their energy (or frequency). We then have a total of two unknowns per beam. A number of layers equal to twice the number of beams would then be necessary to spectrally resolve the incoming light. It is possible however to reduce this number of layers in specific cases since higher frequencies would be absorbed and not "see" deeper layers. If two beams of *known* frequency on the other hand are simultaneously incident on a dual-ring fiber of given film thicknesses, we now have only two unknowns. It is possible in this case to separate their respective number of photons.

A final interesting piece of information we can get out of the measurement of the function R is the penetration depth of the material inside the fiber. Indeed, δ is related to R through the simple relation:

$$\delta(\lambda) = \frac{-t}{\ln(R(t,\lambda))} \qquad \text{(IV-14)}$$
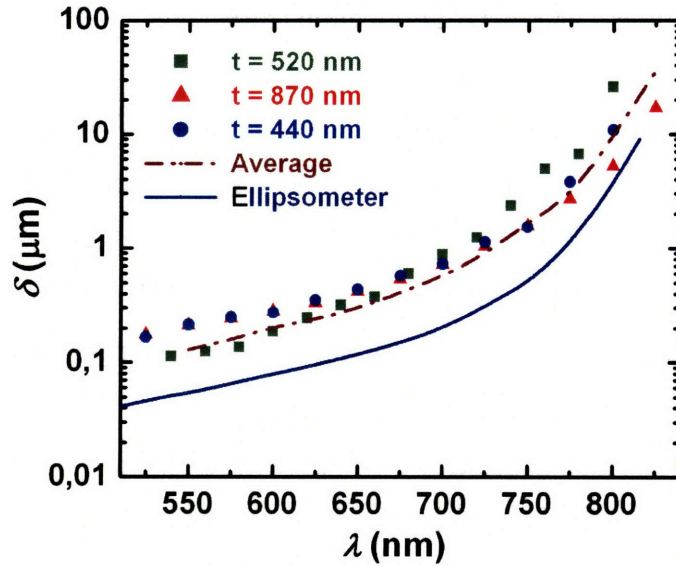
Figure IV-9. Data points: Reconstructed penetration depth for fiber with an $As_{40}Se_{54}Te_6$ glass and three different film thickness. The dash line represents the average of the three thicknesses and the plain line the penetration depth obtained from measurements on an Ellipsometer.

On Figure IV-9 we plotted the penetration depth extracted from R for three different fibers with $As_{40}Se_{54}Te_6$ as the material and three different thickness (data points). We can already notice that the data obtained for these different thicknesses are close, within the range of noise associated to the measurement, especially in the region of better spectral resolution between 600 nm and 750nm. Here, the noise is mostly from the FWHM of the line from the Monochromator which was measured to be around 15 nm. We also show the average penetration depth obtained for the film in the fiber, and the one for the same film deposited on a Silica glass substrate for which the n and k values of the index of refraction were measured thanks to an Ellipsometer (using the relation $\delta = \lambda / 4\pi k$). A small shift towards smaller wavelength is observed but it seems that the optical bandgap obtained using these two independent method of measurement is fairly good. This means that after thermal processing, the optical bandgap of the film remains roughly unchanged. A change in the value of the penetration depth is observed however. This could be attributed to the surface roughness generated during the draw process that scatters some light and lower the mobility of photo-generated charges. It would seem that more photons were absorbed, corresponding to a longer penetration depth. This is confirmed by the fact that the difference between penetration depth seems to get smaller

as the wavelength increase, which corresponds to a case where surface roughness influences less photon absorption.

IV.3.c. Discussion on the spectral resolution

Similarly to the angular resolution case, the question is to know what is the minimal difference in wavelength $\Delta\lambda$ a dual-ring fiber can separate. Again here one understands that this resolution will depend on the intensity of the incoming light, the current noise and the slope of the function R. R is a function of t, λ and δ and its fluctuations due to the noise r is also a function of these parameters, plus on N, the number of incoming photons. A thorough study of this problem would then be extremely complicated. However, we can understand the behavior of the resolution of this system through a few simple idea. Note that on top of the noise generated by the fiber itself (to which we could add the fluctuations of film thickness along the fiber length) the monochromatic line has a noise due to its non-zero FWHM measured to be around 15 nm for the instrument we used. Let us investigate the case where a small signal is impingent on the fiber. Dark current noise i_N (we consider the noise of the inner and outer layer to be roughly the same) dominates the fluctuations and we have, like above:

$$\gamma(t,\lambda,N) = \frac{i_N}{I_{Out}}(R+1)\left(\frac{dR}{d\lambda}\right)^{-1} \qquad \text{and} \qquad I_{Out} = I_{Out}(N)(1-R) \qquad \text{(IV-15)}$$

Where $I_{Out}(N)$ is the photocurrent generated in the outer layer if all the incoming photons N were absorbed in the layer. We can then consider the function $\varphi(t,\lambda)$ for the resolution:

$$\varphi(t,\lambda) = \frac{1+R}{1-R}\left(\frac{dR}{d\lambda}\right)^{-1}$$

We plotted φ for the three fibers with $As_{40}Se_{54}Te_6$ glass and 440nm, 520nm and 870 nm film thickness on Figure IV.10. The value of the derivative of R with respect to λ was extracted by fitting R with a polynomial expression of the fifth order (with a chi^2 error of less than 0.01) and take the corresponding values of this derivative. The maximum resolution is given for a minimum of φ. We can clearly see a range of frequencies of higher resolution for each curve that corresponds to the slope of R being null (when all the light is absorbed in the first layer), then increase to the resolved frequency range and
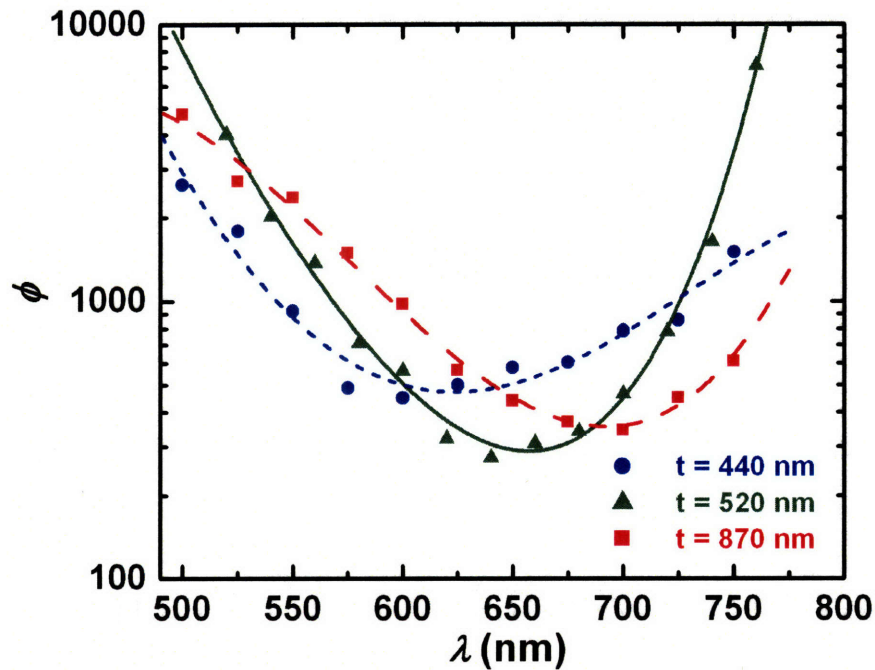
Figure IV-10. Function φ as a function of λ for fibers with same glass $As_{40}Se_{54}Te_6$ and three different thicknesses. Dots are experimental results and the lines are just fittings for the eye.

decrease again to plateau at 0 when absorption in the film is the same. It is also interesting to see that the minimum of φ happens at longer wavelengths as the film thickness increases. This was expected after the influence of t we discussed previously.

Here again, an absolute value of the spectral resolution of an integrated fiber device can't be given since it is strongly dependent on the condition of experimentation. A typical measure of dark current noise in the condition of the experiment we did gave i_N of around 0.5 pA. Typical current for $I_{Out}(N)$ was 30 pA. We get then a resolution as high as 100 nm at the limit where 0<R<1, and as low as 5 nm in the good frequency region. This number is within the noise of the Monochromator that we used. The limitation in this case was from the source itself, and was apparent already in Figure IV-8 where each line spaced by 20nm could already be separated.

IV.4. Integrated fiber device for lensless imaging

Following the work of Abouraddy et al [30] briefly described in chapter 2, we propose a way to use integrated fiber devices to improve the current lensless imaging system. A remark can already be made on the use of a single plan with previously used solid-core fiber devices. Indeed, the approach described above may eventually become useful in optical imaging when a larger number of fibers are included in the web to form images of objects with more detail. Note that this system has an infinite depth of focus, i.e., an image is formed of the object regardless of the distance of the object from the webs, provided that the diffracted field at the locations of the two webs, is intercepted. Furthermore, the image reproduces the object with its real physical dimensions and also determines its physical distance from the webs. In principle, by virtue of obtaining a complete description (both the amplitude and phase) of the electromagnetic field, this approach may be used to image 3D objects that are translucent enough so that excessive occlusion does not occur. Moreover, even though the use of a single dense array having a higher fill factor will result in a strongly perturbed field at the second plane, the reconstruction can still be achieved using a single intensity measurement [58] without the need for a measurement at the second plane. This procedure requires that an over-sampling requirement be satisfied: the sampling of the diffracted field must be dense enough to enable the reconstruction of the autocorrelation function of the object [37, 59].

Using integrated fiber devices, an alternative strategy can be found. Indeed, the above results were all based on the Fresnel function that we reproduce below. The Fresnel transform of a 2 variables function g is given by:

$$\mathfrak{I}_n\{g\}(x, y) = \iint dx'dy'g(x', y')e^{i\frac{\pi\left(x'^2 + y'^2\right)}{\lambda_n d}} e^{i2\pi\frac{xx' + yy'}{\lambda_n d}}$$

The wavelength of illumination and the distance of the plans influence the result of the transform through the exponential term only. Specifically, λ and d affect the integral through their product λd. In the previous section we were able to reconstruct the intensity and phase of an object by measuring the 2D intensity distribution at two different plans. The Fresnel formula however tells us that it would be equivalent to obtain the two intensity distributions on a *same plan*, but at *two different wavelengths*. Interestingly, the

previous section described how new integrated fiber devices can separate the relative intensity of two incoming beams as long as their respective frequency is known. Building a fiber web with dual ring fibers can then enable a more sensitive system (since we go from solid-core fiber to thin-film structure, cf Chapter 3) that can perform the same task of imaging but with one step measurement on a single plane.
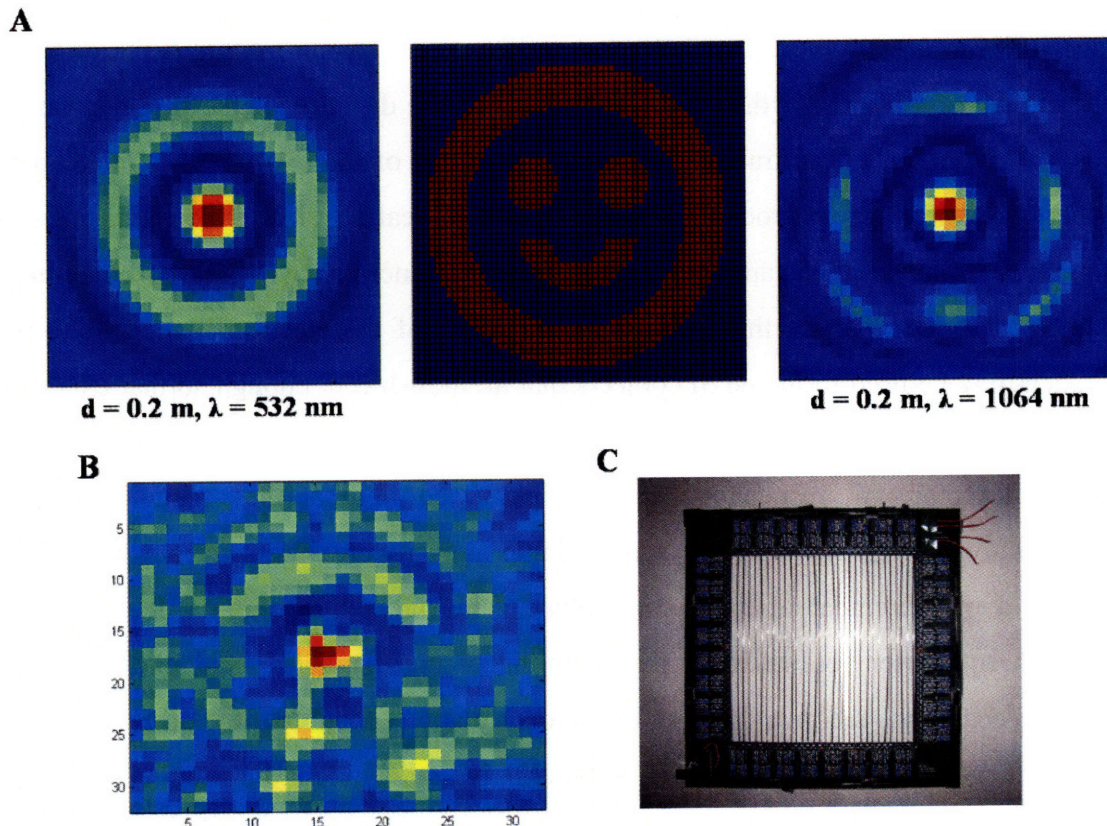
Figure IV.10: A: (middle) computed picture of the object imaged; (left and right) computed diffracted image of the smiley face illuminated at 532 nm (left) and 1064 nm (right) at 20 cm of distance. B: image reconstructed with a CAT scan measurement at 532 nm and 20 cm of distance. C: Picture of the integrated fiber grid.

We built such a grid as can be seen on Figure IV.10c with the same dimension and filling factor as in chapter 2, but made out of integrated fiber devices with two thin-film structures. We are imaging a smiley face as pictured on Figure IV.10a, where we also represented the computed diffraction pattern obtained on a plan at 20 cm illuminated by two different wavelengths 532 nm and 1064 nm (from a pulse NdYag laser for example). The preliminary results obtained are really encouraging: the grid responds very

well and is more sensitive than its counterpart in chapter 2. On Figure IV.10b we show experimental results of the reconstructed image of the smiley face illuminated at 532 nm at plan 20cm away. This early result is already very good considering the small average power seen by the grid because of the pulse nature of the light from the NdYag laser (that we evaluated at around 50 mW). Unfortunately, problems encountered with other illumination sources to be used prevent us from completing this study in this thesis. We refer the reader to a future publication that should come out in early 2008 [60].

We demonstrated in this chapter fibers with angular resolution of less than 4 degrees and spectral resolution as low as 5 nm. This was made possible by the combination of two thin-films of prescribed thickness and composition in a single fiber. In the next chapter we use both a solid-core and a thin-film structure packaged in the same fiber. This combination in a specific design described below enable the observation of a field effect in a fiber-device.

V. Field Effect Fiber Device

V.1. Motivation

Field effect studies in Chalcogenide glasses have been heavily pursued in the 70s and 80s [61-67] since it is a great tool to probe the density of localized states inside the bandgap of these materials. It is indeed the concentration and distribution of those that are responsible for most of their electronic properties [28,29]. Because of the difficulties encountered and the rise of crystalline semiconductor technology, amorphous semiconductors and especially chalcogenide glasses have been left a bit aside for applications involving electronic junctions.

The use of chalcogenide glasses inside fiber devices is natural in our case because we make use of their thermo-mechanical properties and their amenability to thermal drawing. However so far, neither junctions nor non-linear electronic behavior in fiber devices have been reported. This would pave the way to a whole new scope of functionalities and applications for fiber-based devices. In this chapter we focus on the simplest field effect structure depicted in Figure V-3 which involves only one semiconductor (p-type in our case), an insulator for which we use the polymer itself, and three electrodes. The objectives are three-fold: (1) Demonstrate the use of new materials as active components in the device. Specifically, we show that for the first time electronic properties of the polymer are used and enable the field effect observed. Moreover, the gate electrode can be engineered to be a chalcogenide glass core that has been annealed and partially crystallized to increase its electronic conductivity as we will explain. (2) The structure we are studying is an ideal tool to investigate the distribution and density of localized states of the glasses we use, especially after post-drawing crystallization process. Such fibers can teach us about the electronic structure of the material before and after annealing which can be of great interest for the design of future devices. (3) Finally, demonstrating memory device capabilities integrated inside flexible, low weight and inexpensive fiber devices is of great interest in different area of applications.

We first explain the main features, based on different references [28,29,68-76] of the density of states of chalcogenide glasses which explain many of their electronic properties. We then focus on the field effect in chalcogenide glasses and show early

attempts and results in fiber form. Finally we show how by changing the structure and annealing the fiber we were able to create the first field effect inside a continuous thermally drawn fiber device.

V.2. Electronic properties of chalcogenide glasses

Chalcogenide glasses, to the contrary of amorphous solids made up primarily of Group-IV or Group-V elements, exhibit p-type conductivity, do not have variable-range hopping nor show any Electron Paramagnetic Resonance (EPR) signal [29]. Moreover, their Fermi energy varies only slowly with electronic density or temperature, and thus is effectively pinned. In this first part we present a model of negative correlation energy that explains these features.

V.2.a. Dangling bonds and the negative correlation energy

A dangling bond is simply a broken or unsatisfied bond in a covalent solid. A simple dangling bond normally contains one electron and is electrically neutral. However, it is able to donate or accept an electron, and under certain circumstances the electronic occupancy can change, varying concomitantly the charge of the center. It is important to note that we are here concerned with amorphous materials, where the nature of the structure, namely disorder, makes an isolated dangling bond a perfectly feasible entity. On the contrary, in crystalline materials, if an atom is removed from for example a tetrahedrally coordinated diamond cubic lattice, four dangling bonds remain pointing into the vacancy, and this is the least number that can result from the introduction of vacancies. Thus, the possibility of the existence of single isolated dangling bonds is a consequence of the presence of structural randomness that characterizes amorphous semiconductors.

A simple molecular orbital picture can convince oneself that dangling bonds are expected to introduce electron states deep into the gap, which is otherwise empty of state, except for band tailing below the mobility edges resulting from the randomness of the

potential. A single dangling bond will be either empty (positively charged as one electron was lost), occupied by one electron (neutral) or filled with 2 electrons (negatively charged). Adding a second electron on a site obviously involves a cost in energy due to the coulomb repulsion between the two charges, $U = \langle \dfrac{e^2}{4\pi\varepsilon_0\varepsilon r_{12}} \rangle$ (Hubbard electron repulsion energy), but we will see that strong coupling with phonon can occur and lead to an effective correlation energy between two electrons on the same site, U_{eff}, to be negative.

The density of states in the gap for an amorphous semiconductor containing isolated dangling bond defects might be then as shown schematically in Figure V-1. The dangling bond level is broadened by disorder (bond-angle fluctuation etc.) into a band. This representation of the density of states can account for many features observed in chalcogenide glasses, such as the presence of a mobility edge separating extended and localized states, the existence of a gap, which explains the transparency of glasses at certain frequencies, the pinning of the Fermi level by the presence of the defect states, etc. If the two defects are separated in energy, the Fermi level will lie in the gap between them, or if, as in Figure V-1, they overlap, Ef will lie in the center of the region of overlap. Although in this situation we have E_f lying in a band and one might think that the material should be metallic, it must be remembered that E_f lies in a band of localized states, so the charges excited above the Fermi level don't contribute to any current and the material remains a semiconductor.

Now that we are familiarized with the single dangling bond, let us try to understand how the sign of the effective correlation energy $Ueff$ can influence certain properties of the glasses.

V.2.b. The negative correlation energy

In order to account for the apparent complete diamagnetism of chalcogenide glasses, Anderson [70] was the first to suggest the presence of dangling bonds with *negative effective electronic correlation energy*. Street and Mott [71] following this idea
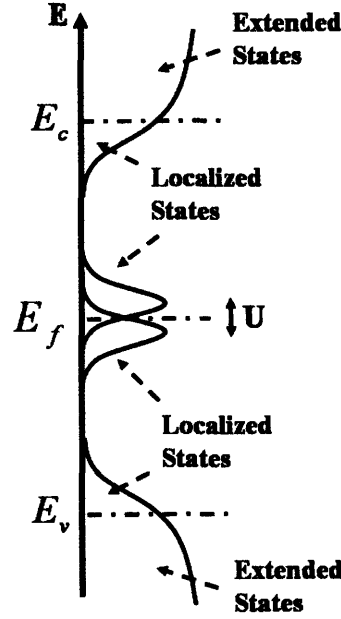
Figure V-1. Density of states for an amorphous semiconductor with the presence of single dangling bonds.

proposed a model in which the localized states in the gap of chalcogenide glasses appear at dangling bond with again a negative effective correlation energy, which explains a lot of the features introduced above.

One way to understand how a correlation energy can be negative is to consider electron-phonon interaction. Below we will discuss another chemical approach that explains this negativity as well. Let us derive a simple Hamiltonian for the electrons and phonons, using the creation (annihilation) operators formalism, where $c_{i\sigma}^{*}$ $(c_{i\sigma})$ is the creation (annihilation) operator for the electrons and $b_{i\sigma}^{*}$ $(b_{i\sigma})$ the ones for the phonons.

The electronic term of the Hamiltonian can be written as following, neglecting the hopping interaction with neighboring sites:

$$H_e = \sum_{i,\sigma} E_i n_{i\sigma} + U \sum_i n_{i\sigma} n_{i-\sigma}$$

where E_i is the energy of an electron localized on site i, $n_{i\sigma} = c_{i\sigma}^{*} c_{i\sigma}$ is the occupancy of site i by an electron with spin σ, and U is the Hubbard electron repulsion energy introduced above.

The phonon term can be written as:

$$H_p = \hbar\omega \sum_i b_i^{*} b_i$$

where ω is the phonon frequency, taken to be constant in the Einstein approximation. The electron-phonon coupling term can be taken to be linear:

$$H_{e-p} = \lambda \sum_{i,\sigma} n_{i\sigma} (b_i + b_i^*)$$

where λ is the electron-phonon coupling constant. This cross term can be eliminated by introducing a displaced phonon operator $d_i = b_i + \dfrac{\lambda n_i}{\hbar\omega}$ where $n_i = n_{i\sigma}^* + n_{i\sigma}$.

The total Hamiltonian can then be rearranged, and we obtain:

$$H = \sum_{i,\sigma} \left(E_i - \frac{\lambda^2}{\hbar\omega} n_{i\sigma} \right) n_{i\sigma} + \left(U - \frac{2\lambda^2}{\hbar\omega} \right) \sum_{i,\sigma} n_{i\sigma} n_{i-\sigma} + \hbar\omega \sum_i d_i^* d_i$$

Hence, the effective Hubbard correlation energy for two spin-paired electrons at the same site is given by;

$$U_{eff} = U - \frac{2\lambda^2}{\hbar\omega} \tag{V-1}$$

which is negative if $\dfrac{2\lambda^2}{\hbar\omega} > U$, i.e. for strong electron-phonon coupling.

A crucial observation is to be made here: at low frequency, when the last term of the total Hamiltonian can be neglected, It is straightforward to see that for one site, the energy level of the site occupied by n electrons (n=0, 1 or 2) are given by:

$$n = 0 \Rightarrow E_0 = 0$$
$$n = 1 \Rightarrow E_1 = E_{eff} \tag{V-2}$$
$$n = 2 \Rightarrow E_2 = 2E_{eff} + U_{eff}$$

with $E_{eff} = E - \dfrac{\lambda^2}{\hbar\omega}$. We can see that when U_{eff} is negative, $E_2 + E_0 < 2E_1$, which means that it is energetically favorable for electrons to pair up rather than remain unpaired, such that at certain sites there are two electrons and at others none. This simple result already explains the diamagnetism observed in many chalcogenide glasses: the electrons that in majority pair up, have opposite spin according to the Pauli's exclusion principle that cancel each other.

Let us see how a simple statistical model for a single dangling bond defect with a negative U_{eff} can explain other features presented earlier.

V.2.c. Pinning of the Fermi level and p-type conductivity

A single dangling bond defect can be view as a Grand Canonical Ensemble, as its energy and the number of particles that occupy it change. The thermodynamic potential of such a system is then a function of the temperature T, and of the chemical potential μ, and can be written as follow (neglecting all other external parameters):

$$\Phi(T,\mu) = U - TS - \mu\langle N \rangle$$

where $\langle N \rangle$ is the average number of particles in the system. The relation between the thermodynamic potential and the partition function is given by:

$$\Phi(T,\mu) = -kT \ln Z_G$$

from which we get the very useful relations:

$$\bar{n} = \langle N \rangle = kT \frac{\partial \ln Z_G}{\partial \mu}$$

$$U = kT^2 \frac{\partial \ln Z_G}{\partial T}$$

and the partition function is given by:

$$\sum_{states} \Omega(E,N) e^{-(E-\mu N)/kT}$$

where $\Omega(E, N)$ is the degeneracy of a state of energy E with N particles. In our case, we saw that the dangling bond can be empty, occupied by one electron of spin up or down (degeneracy of 2), or full with 2 electrons. We derived in the previous section the energies for these states. Then, we can derive the partition function of our system, and we obtain:

$$Z_G = 1 + 2e^{(\mu-E_{eff})/kT} + e^{(2\mu-(2E_{eff}+U_{eff}))/kT}$$

Now we can consider a larger picture for our system, namely a cloud of electrons in interaction with N_0 defects. The defects are independent from each other, so the partition function for the total system is straightforward:

$$Z_{total} = Z_G^{N_0}$$

from which we can express the number of electrons per defect site n, which will be very useful to study how the Fermi level changes when electrons are injected in the system,

why it is "pinned" for U_{eff} negative, and where it stands between the conduction and valences bands.

$$n = \frac{kT}{N_0} \frac{\partial \ln Z_{total}}{\partial \mu} = \overline{n}$$

One last reminder is how to link the chemical potential with the Fermi level. We simply have, as it can be easily demonstrated for a quantum fermions gas:

$$E_F = \lim_{T \to 0, n fixed} \mu(T)$$

Finally, we saw that a system of electrons in interaction with single dangling bond defects can be represented by the number of electrons per defect and the partition function:

$$Z_G = 1 + 2e^{(E_F - E_{eff})/kT} + e^{(2E_F - (2E_{eff} + U_{eff}))/kT} \tag{V-3}$$

To get a good understanding of the system, it is convenient to think about what happens when new electrons are injected, or as n, the number of electrons per defect site, increases. Intuitively, when the correlation energy is positive, it is energetically better for the system to put one electron per defect site. Then when n goes from 0 to 1, the defects get occupied by one charge only and almost no defect gets doubly occupied. Of course, when there are more electrons than defects (n>1), the defects start to be filled. This simple understanding can lead to separate two cases:

Case #1. 0<n<1: We can neglect the last term in Z_G, which accounts for the doubly occupied states, because all the defects are either unoccupied or singly occupied:

$$Z_G(0 < n < 1, U_{eff} > 0) \approx 1 + 2e^{(E_F - E_{eff})/kT}$$

It is from this very easy to express the Fermi level in term of n:

$$n = kT \frac{\partial \ln Z_G}{\partial \mu} = \frac{2e^{(E_F - E_{eff})/kT}}{1 + 2e^{(E_F - E_{eff})/kT}} = \frac{1}{1 + \frac{1}{2} e^{-(E_F - E_{eff})/kT}}$$

$$\Rightarrow E_F = E_{eff} - kT \ln\left[\frac{2(1 - n)}{n}\right]$$

Case #2. 1≤n≤2: In that case, no defect is empty as we discussed previously, so we can neglect the first term in Z_G, which accounts for the unoccupied defects:

$$Z_G(1 < n < 2, U_{\textit{eff}} > 0) = 2e^{(E_F - E_{\textit{eff}})/kT} + e^{(2E_F - (2E_{\textit{eff}} + U_{\textit{eff}}))/kT}$$

So

$$n = \frac{2e^{(E_F - E_{\textit{eff}})/kT} + 2e^{(2E_F - (2E_{\textit{eff}} + U_{\textit{eff}}))/kT}}{2e^{(E_F - E_{\textit{eff}})/kT} + e^{(2E_F - (2E_{\textit{eff}} + U_{\textit{eff}}))/kT}} = \frac{1 + e^{(E_F - (E_{\textit{eff}} + U_{\textit{eff}}))/kT}}{1 + \frac{1}{2}e^{(E_F - (E_{\textit{eff}} + U_{\textit{eff}}))/kT}}$$

$$\Rightarrow E_F = E_{\textit{eff}} + U_{\textit{eff}} + kT \ln\left[\frac{2(n-1)}{2-n}\right]$$

Combining these two results, we obtain the plot represented in Figure V-2(a). This sketch accounts for the features described earlier: as the electron concentration n increases from zero (at $T = 0K$), the Fermi level rises slowly in the lower singly occupied level (note that the density of upper levels is equal to the density of the filled lower level, as a state cannot be doubly occupied for a positive $U_{\textit{eff}}$ material until it is first singly occupied). As soon as n=1, the Fermi level jumps discontinuously across the gap of magnitude $U_{\textit{eff}}$ to the upper level, and subsequently rises gradually through this level until $n = 2$ and all states are doubly occupied. These results are consistent with the observation of a modulation of the Fermi level via variation of electronic density and with predominance of variable-range hopping near E_F at low temperatures. Then, according to experimental data, amorphous materials from groups IV and V have indeed a positive correlation energy.

The situation is very different when $U_{\textit{eff}}$ is negative. Intuitively, when we start at n=0 and we add 2 electrons to the system, we saw that it is energetically favorable for them to occupy a same site. As more electrons are injected, defects will be either fully occupied or empty, for any value of n such as 0<n<2. Thus we can here neglect the second term in Z_G, which takes into account the singly occupied states:

$$Z_G(n, U_{\textit{eff}} < 0) = 1 + e^{(2E_F - (2E_{\textit{eff}} + U_{\textit{eff}}))/kT}$$

Again here we can extract the Fermi level:

$$n = \frac{2e^{(2E_F - (2E_{eff} + U_{eff}))/kT}}{1 + e^{(2E_F - (2E_{eff} + U_{eff}))/kT}} = 1 + \tanh((E_F - (E_{eff} + 1/2U_{eff}))/kT)$$

$$\Rightarrow E_F = E_{eff} - \frac{|U_{eff}|}{2} - \frac{kT}{2}\ln\left[\frac{2-n}{n}\right] \tag{V-4}$$

The Fermi level for the case of a negative correlation energy is plotted in Figure V-2 (b). The levels corresponding to double occupancy lie below those for single occupancy, and the density of lower levels is equal to the number of electrons introduced and thus this band is always full, as can be seen in Figure V-2 (b). The injection of electrons into such a material therefore results in immediate double occupancy of levels without an intermediate n=1 stage. Thus, E_F remains pinned midway between the two levels at an energy $E_{eff} - U_{eff}/2$ for all values of n. This provides a natural explanation of the fact that field-effect measurements indicate a very large density of states at E_F in chalcogenide glasses, but no variable-range hopping is observed. As electrons are injected into this system, they populate the quasiparticle levels at E_{eff} and $E_{eff} - U_{eff}$, leaving the Fermi energy unchanged. However, there is actually no density of quasiparticle states at E_{eff}; the Fermi energy is pinned by states $\pm\frac{1}{2}U_{eff}$ away.

What is striking in this model is that we can see that the Fermi level lies below the energy of the highest filled one-electron state, even at $T = 0K$. The physical reason for this apparently strange result is that although excitation of one electron from the valence band to the defect state requires an energy of $E_{eff} - E_v$, excitation of two electrons takes an energy of only $2E_{eff} - U_{eff} - 2E_v$. Thus, excitation of a large number of electrons requires the average energy $E_{eff} - \frac{1}{2}U_{eff} - E_v$, or $E_F - E_v$, as it should. The physical consequence of this result is that E_F is lower in energy than would be expected from the defect energy E_{eff}. Consequently, E_F is closer to the valence band than it would be for positive or zero correlation energy, and p-type conduction is favored. This is in
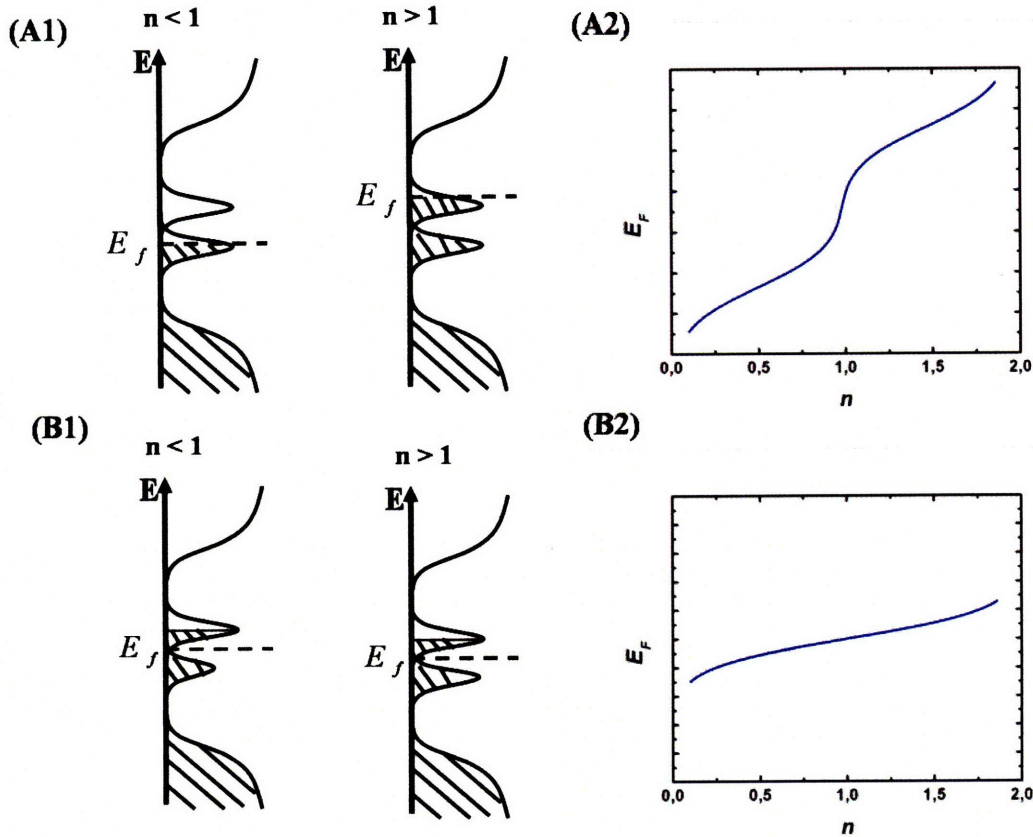
Figure V-2. Density of states (a1 and b1) and Fermi level (a2 and b2) as a function of electron occupation *n*, for (a) positive correlation energy defects and (b), negative correlation energy defects.

agreement with experimental results on chalcogenide glasses, almost all of which exhibit a p-type thermopower.

The effect of a negative correlation energy is also key to understand field effects in chalcogenide glasses.

V.3. Field effect in chalcogenide glasses

Field effects in chalcogenide glasses have been extensively studied in the past [61-67] as we mentioned. Marshall and Owen were the first to obtain solid results using As_2Te_3 and $As_{30}Te_{48}Si_{12}Ge_{10}$ [65]. Later, Mahan and Bube [66] also obtained a clear field effects in similar type of glasses. Radjy and Green [67], however, observed that the field effect modulation decays to a very small value over time. Basing our analysis on the

excellent paper of Robert C. Frye and David Adler [69], we explain briefly the theory and show the first results we obtained of FET inside fiber devices.

V.3.a. Basic theory

The structure used to study field effects in chalcogenide glasses, which we have reproduced in fibers, contain a p-type chalcogenide glass contacted by two parallel electrodes called the Source and the Drain as shown in Figure V-3(a). A third electrode, the Gate, is isolated from the semiconductor by an insulating layer. The gate, insulator and semiconductor form a capacitor. As can be seen in Figure V-3(b), when a voltage is applied between the gate and the drain (or source) charges are generated at the surface but also inside the bulk of the semiconductor. These charges participate to the current between the Source and the Drain which gives rise to the field effect.

Since, especially in the fiber case as we will see, the charges generated when a voltage V_G is applied to the gate expand in the bulk by a distance small compared to the thickness of the insulator t, the total induced charge per unit area is given by:

$$Q = \frac{V_G \varepsilon}{t} \qquad (V-5)$$

where ε is the dielectric permittivity of the insulator. As we saw earlier, amorphous semiconductors contain delocalized as well as localized states inside the bandgap. The induced charges is then composed of free, Q_F, and trapped, Q_T, carriers with $Q = Q_F + Q_T$. Only free charges will be responsible for the change of conductivity $\Delta\sigma$ between the Source and the Drain and we have:

$$\Delta\sigma = \mu_f Q_f \frac{d_{DS}}{l}$$

where μ_f is the mobility of the free carriers, d_{DS} is the distance between the source and the drain and l the width of the conducting path. The change of current between the source and the drain is then given by:

$$\Delta I_{DS} = \mu_h \frac{d\varepsilon}{lt} V_{DS} V_G \qquad (V-6)$$
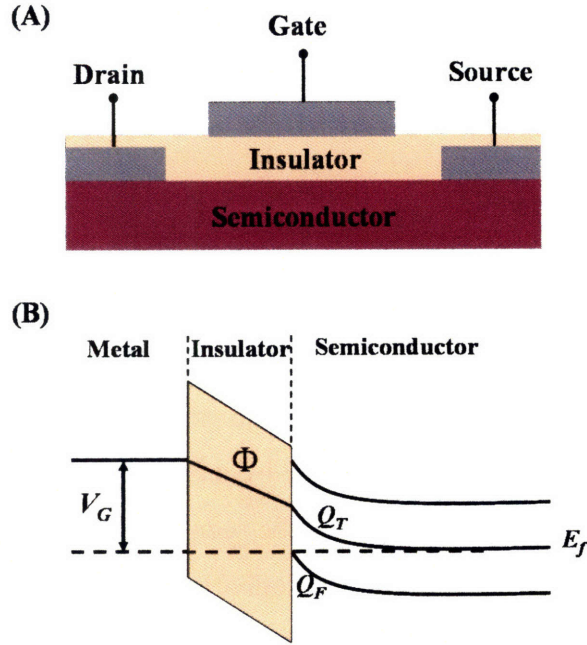
Figure V-3. (a) Schematic of a simple field effect Transistor structure. (b) Band diagram of a Metal Insulator Semiconductor (p-type) junction when a negative voltage is applied to the metal.

where μ_h is the trapped-limited mobility of holes in the semiconductor, $\mu_h = \dfrac{\mu Q_f}{Q}$. In a system like ours where the density of localized states is large and where the negative correlation energy pins the Fermi level when charges are injected into the system as demonstrated in the first part, we expect the ratio of free to total charges to be very low. The change of current ΔI_{DS} should then be small and barely any field effect can be observed.

This is of course in contradiction with the observed field effects cited above, although Radjy and Green observed that the field effect decays with varying times, sometimes several hours long [67].

V.3.b. Valence Alternative Pair (VAP) model

Robert C. Fried and David Adler developed a convincing model to explain the presence of field effect in chalcogenide glasses and its transient nature [69]. We refer the reader to their work for a complete treatment of the problem and present here only the main concepts and conclusions that will help us understand our results. The significant

addition to the formalism developed so far is the distinction between two types of dangling bonds: an acceptor-like and a donor-like that can transform into one another by a simple structural change involving a bond breaking or bond formation and a small atomic relaxation. These pairs of positively and negatively charged atoms with different coordination number (depending on the glass structure) are called Valence Alternation Pair (VAP), a concept developed first by Kastner et al [73]. These charged defect centers have a very low creation energy which ensures their presence in large numbers as the material is quenched below the glass transition temperature.

Above we demonstrated that a strong electron-phonon coupling can lead to a negative correlation energy. In this model however, a strong contribution to the negative correlation energy is chemical in origin [73,74]. Indeed, when electrons are injected inside the system, they first neutralize the ionized donors and ionize some of the neutral acceptor states. This leads to an imbalance in the number of neutral donor versus neutral acceptors and some of the former transform as described above into the later, even in ionized acceptors. As the acceptor density increases, the Fermi energy is pulled back down to its initial solution as seen in Figure V-2(b). This pinning of the energy level results from a negative correlation energy of chemical nature since it is a change of defect state structure that favors the location of two electrons on a same site.

In more mathematical terms, the model now has two defect types: a donor-like type that can be either neutral (d^0) or positively charged (unoccupied, d^+), and an acceptor-like type that can be either neutral (a^0) or negatively charged (a^-). For simplicity we keep the same notations as in [69], and consider the energy of d^+ to be zero, d^0 has an energy T_0 (which corresponds to E_{eff} in the previous section, Equation (V-2)), a^0 has an energy T_0+W and a^- which represents the doubly occupied states has an energy of $2T_0-U$, where U is positive ($U=-U_{eff}$ in the previous section). The difference of energy between the neutral acceptor and the neutral donor is W. The grand partition function is thus now:

$$Z_G = 1 + 2(e^{(E_F-E_{eff})/kT} + e^{(E_F-(E_{eff}+W))/kT}) + e^{(2E_F-(2E_{eff}+U_{eff}))/kT}$$

The average occupation n is still given by Equation (V-4), and the Fermi energy of this system at equilibrium, μ_0 is still given by $\mu_0 = T_0 + \frac{1}{2}U$, obtained when $n = 1$. This is also the Fermi level at equilibrium of the material since the density of localized states is

expected to be much higher than the one of electrons in the conduction band or holes in the valence band. Since a voltage $V = q\Phi$ is applied, the chemical potential is replaced by $E_F - q\Phi$.

With obvious notations, the total number of localized states is given by:

$$N = N_D + N_A = N_D^+ + N_D^0 + N_A^+ + N_A^0$$

Considering the subsystems of donor-like and acceptor-like we see that at equilibrium and for $\Phi = 0$ we have:

$$N_D^+ = \frac{N_D}{1 + 2e^{-(U/2-E_F)/kT}}$$

$$N_A^- = \frac{N_A}{1 + 2e^{-(U/2+W-E_F)/kT}}$$

Finally, at equilibrium:

$$N_D^0 = e^{W/kT} N_A^0 \tag{V-7}$$

This leads to the relationships

$$N_D \approx \frac{N}{2}\left(1 + \tanh\left[(E_F - q\Phi)/kT\right]\right)$$

$$N_A \approx \frac{N}{2}\left(1 - \tanh\left[(E_F - q\Phi)/kT\right]\right) \tag{V-8}$$

which show that the densities of donors and acceptors vary with applied electrostatic potential, and substantiate the pinning of the Fermi level described above.

This analysis shows that in chalcogenide glasses, the high density of localized states prevents the observation of any field effect. Even though this claim is contradicted by the solid results presented by different groups, as we mentioned above, the first attempt to obtain a field effect in fiber devices has failed.

V.3.c. Results on early fiber structures

The first FE fiber made had a simple structure as shown on Figure V-4(a) and (b), We can clearly see the drain and the source electrode contacting a semiconducting thin-film. A third electrode, the gate, is in contact with the polymer that acts as the capacitor. Note that this is the first time the electrical properties of the polymer, here PES, are used. On Figure V-4 (c) and (d) we show the drop of potential in the polymer layer between the
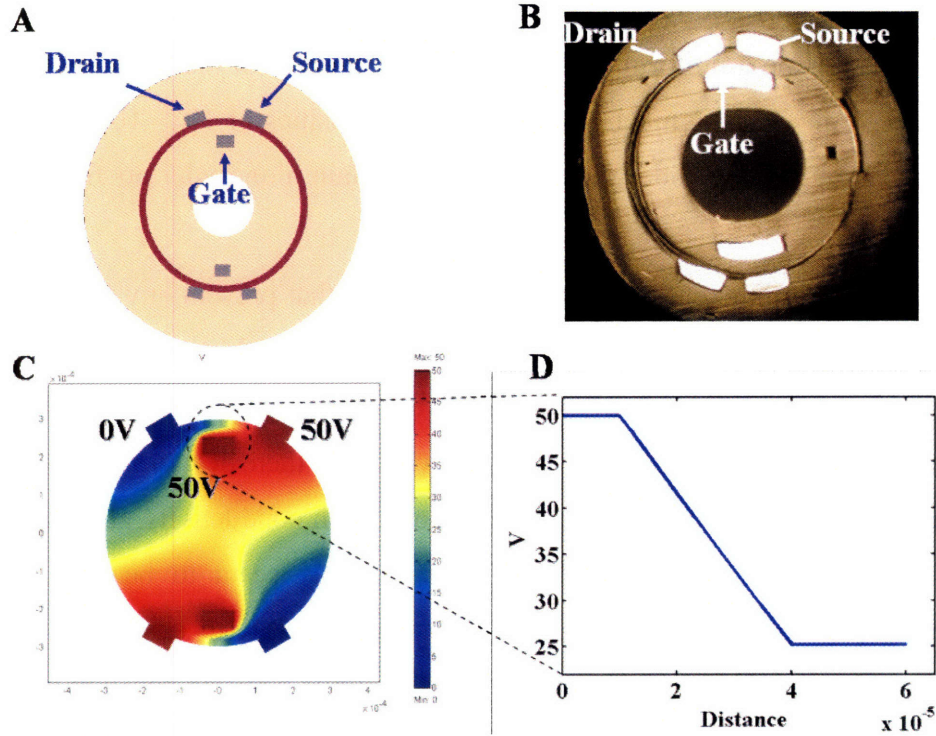
Figure V-4. (a) Schematic of a FET fiber cross section. (b) Microscope picture of the cross section of a FET fiber of same structure as in (a). (c) Color map of the voltage distribution in a FET fiber structure, with 50V applied on the drain and the gate, the source being grounded. (d) Voltage drop in the insulating layer. Both (c) and (d) graphs are computed with the finite element code software FemLab.

semiconductor and the gate electrode. Using the same finite element code software we used earlier to determine the electric field in the photoconducting fibers, we simulated the voltage distribution in the fiber when 50V is applied to the gate and the source, while the drain is grounded. There is a sharp drop of potential across the insulating element, because the surface of the glass film is forced to be at a gradient potential by the source and drain. For a thickness of typically 10 microns, the drop of 25 V in the film creates an electric field of around $2.5*10^8$ V/cm, in the range of what is used in the modern wafer based optoelectronic devices [3-5,77]

The p-type semiconducting glasses used in these fibers were chosen to exhibit as little localized states as possible. $As_{40}Se_{60-x}Te_x$ glasses and glasses doped with germanium (GAST) such as $Ge_{15}As_{15}Se_{30}Te_{20}$ were used. However, barely any field effect could be obtained with these designs. An inherent problem can be understood by making a simple calculation. For typical dimensions of fiber length (l = 150 mm), the insulating layer thickness (t = 50μm), and the distance between the electrodes (d_{DS} = 100

μm), a gate voltage of 200V, and a film thickness of 500nm, we obtain a total charge induced, if we assume a uniform distribution of the charges in the semiconducting film, of around 10^{17} cm^{-3}. This is much smaller than the densities of 10^{19}- 10^{20}cm^{-3} evaluated for traps in many chalcogenide glasses and can explain alone why no field effect was observed.

On top of the inherent problem of defect states that prevent any field effect to be observed, the structure chosen can also be improved. Indeed, electrodes facing each other require a minimum thickness of polymer in between them for the structure to hold, which limits the capacitance value that can be achieved. We then designed a new structure where the gate is the core of the fiber made out of a high conductivity glass, as shown in Figure V-5. In this configuration, the dimensions may seem to be too large for a significant drop of potential to occur in the insulating layer (to charge the capacitor). However, the large difference of electrical conductivity between the polymer and the glass core ensures that most of the potential drop will occur in the insulator. Indeed, if a potential is applied between the Gate and the Source, the equivalent circuitry is like having two resistances, the solid-core and the polymer tube, in series (we can neglect the influence of the semiconducting films). PES polymer has typically an electrical resistance 4 to 7 orders of magnitude larger than the chalcogenide glasses we use. Since the core is only at maximum an order of magnitude larger in size, it is clear that resistance of the polymer tube is orders of magnitude higher than the one of the solid-core. The potential will hence drop almost entirely into the insulating layer.
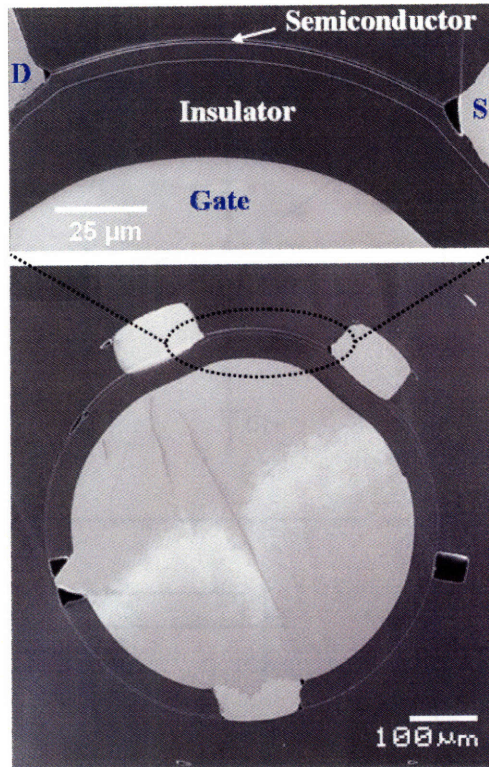
Figure V-5. SEM micrograph of a FE fiber with a magnification of the region of interest on top. One can clearly see the Source (S) and the Drain (D) contacting a semiconducting film. The Gate is the fiber core and is separated from the semiconductor by a polymer (or insulating) layer.

This improvement in structure significantly facilitated the fabrication of FE fibers and enabled the introduction of thinner insulating layer. In return, more charges could be generated in the semiconducting film as a voltage was applied to the gate. Yet, this wasn't sufficient to overcome the density of localized states since no field effect was observed as shown in Figure V-6(a) and (b). The field effects were tested by applying a constant voltage between the source and the drain, V_{DS} (equal to 50V in that case) and measuring the change of current between them, ΔI_{DS}, as a voltage is applied between the gate and the source. The applied voltage was modulated in two ways, as in [69], schematized on the insets of Figure V-6(a) and (b). The symmetry observed in the change of drain-to-source current between positive and negative gate voltages is the mark of no field effect. The simple step voltage, used for transient experiments, shows a rapid decay of the change of ΔI_{DS} down to a zero value.
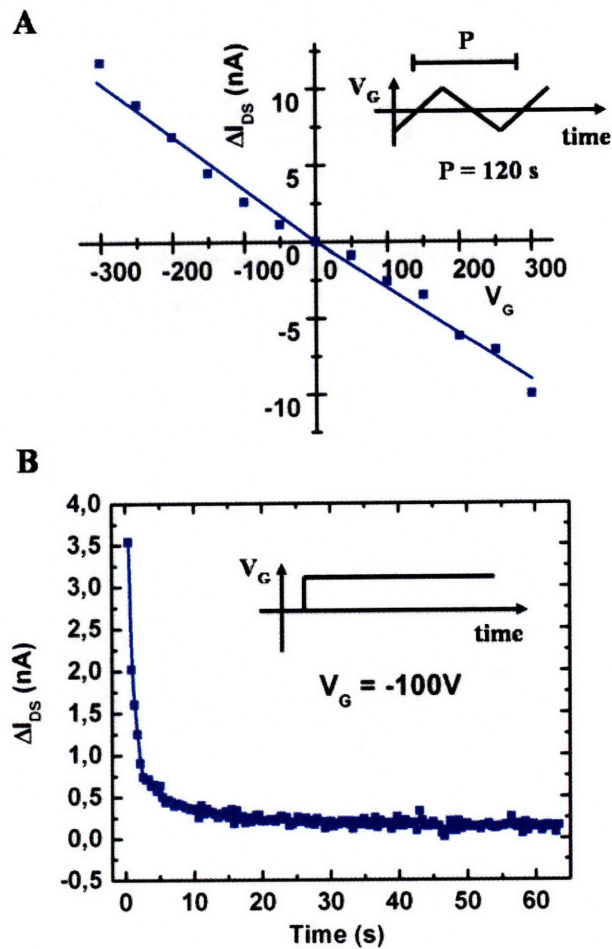
Figure V-6. (a) Change of source-to-drain current with different gate voltages applied with a periodicity of 120s. (b) Decay with time of the source-to-drain current change as a gate voltage of -100V is applied and maintained.

These results lead to the conclusion that only lowering the density of defects dangling bonds responsible for the pinning of the Fermi level as explained above can lead to the observation of a clear field effect. It turns out that post-drawing annealing of fiber devices seems to be doing just so.

V.4. Post-drawing crystallization

V.4.a. Principle and motivation

The amorphous nature of the semiconductors dealt with so far is critical for the fabrication of fiber devices. However, the defect states that come with the disorganized structure can be an inherent limitation to attainable sensitivities and functionalities for

fiber based devices. In an effort lead by Dr. Sylvain Danto [78], we found a way to overcome this smilingly fundamental constraint by performing a thermal-induced post-drawing crystallization of the chalcogenide glass inside the fiber. The amorphous semiconductors we select require to be stable against crystallization to resist the draw process as explained in chapter one. However, it is possible to identify glasses that will be at their limit of crystallization during the draw process, and that an adequate thermal treatment in the fiber form can significantly change the structure of the material over time. I refer the reader to the work of Dr. Sylvain Danto to be published soon for more details on the mechanism of such crystallization [78]. Here I will focus on the effect of heat treatment on FE fibers, especially how we were able to reduce the density of localized states in the semiconducting film and indeed observe a field effect in our fibers. First we show the field effect results obtained that we discuss in a last section.

V.4.b. The first Field effect fiber device

The FE fibers we tested in the previous section that showed no clear field effect were placed in an oven set at 208C for time varying between 48 and 312 hours. The temperature was chosen to allow a slow crystallization process while maintaining intact the polymer matrix that holds the fiber. Indeed, PES has a T_g of around 230C, well above the annealing temperature. In Figure V-7 we show SEM micrographs of a similar FET as in Figure V-5 annealed for 288 Hrs at 208 C. Features that resemble to crystal regions can be observed although such observation can't lead to firm conclusions. We refer the reader to the work of Danto et al for a more detailed study based on SEM micrographs, DSC and X-ray analysis [78]. Here we strengthen these assertions by demonstrating a significant change in electronic properties of the semiconducting film.

The first drastic change observed occurs in the conductivity itself. Figure V-8(a) shows an increase of orders of magnitude in conductivity as the fibers are annealed. Note that these values are averaged over a few samples tested. Damaged samples but also small variations of temperature in the oven lead to quite large variations in results. However, a careful selection of sample and a controlled heat process enabled us to obtain repeatable results. One feature to be noticed and that was observed in all the annealed
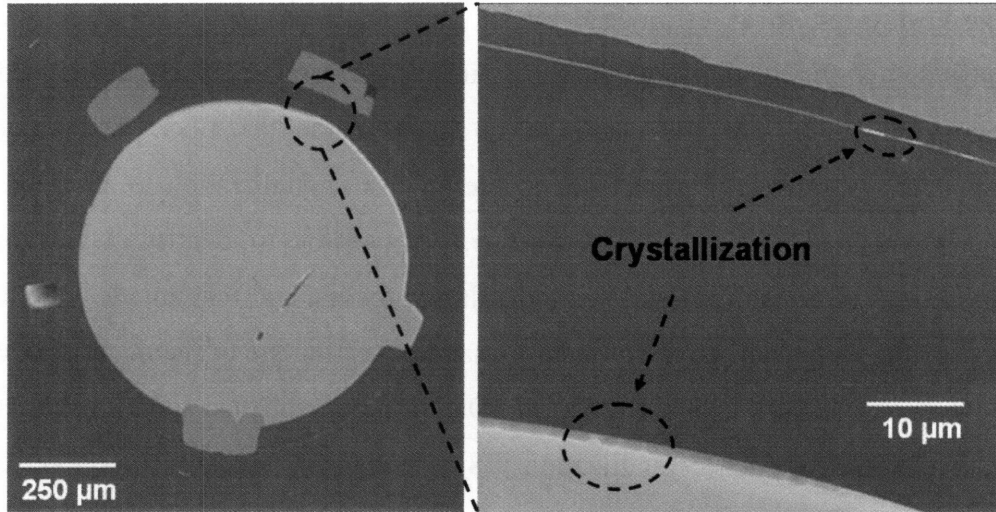
Figure V-7. SEM Pictures of the whole structure (left) and magnification (right) on regions where structural changes are apparent in the fiber core and in the thin film.

samples is that the current has a very slow transient behavior. We associate this to the reminiscence of deep trapping states in the material with long escaping time (several minutes). Yet, this sharp increase of conductivity is we believe due to a decrease in the density of localized states inside the Bandgap. As crystallization proceeds, dangling bonds disappear and so are VAPs. The mobility of carriers is as a result increased and so is the conductivity. The advantage of having an FE structure inside the fiber, besides interesting device applications, is that it enables us to probe the density of localized states and have a deeper insight of what is happening as we anneal the film.

We annealed for 288 Hrs the same fiber we tested in Figure V-6. We then subjected it to the same conditions of experimentation to observe a field effect (namely, $V_{DS} = 50$ V and a modulated change of gate voltage with a period P = 120 s). Figure V-8(b) clearly shows a field effect patterning to a p-type semiconducting film. The results are even more compelling when compared to the one obtained before annealing. These results represent the first non-linear response observed in a fiber-based device and demonstrate our ability to control the density of states in the semiconducting material inside the fiber. Indeed, this suggests that the annealing process drastically reduced the density of localized states in the bandgap so that the injection of holes in the system would enable the Fermi level to move and an activated current type of response could be observed. Looking at the experimental results of Figure V-8(b) and using Equation (V-6)
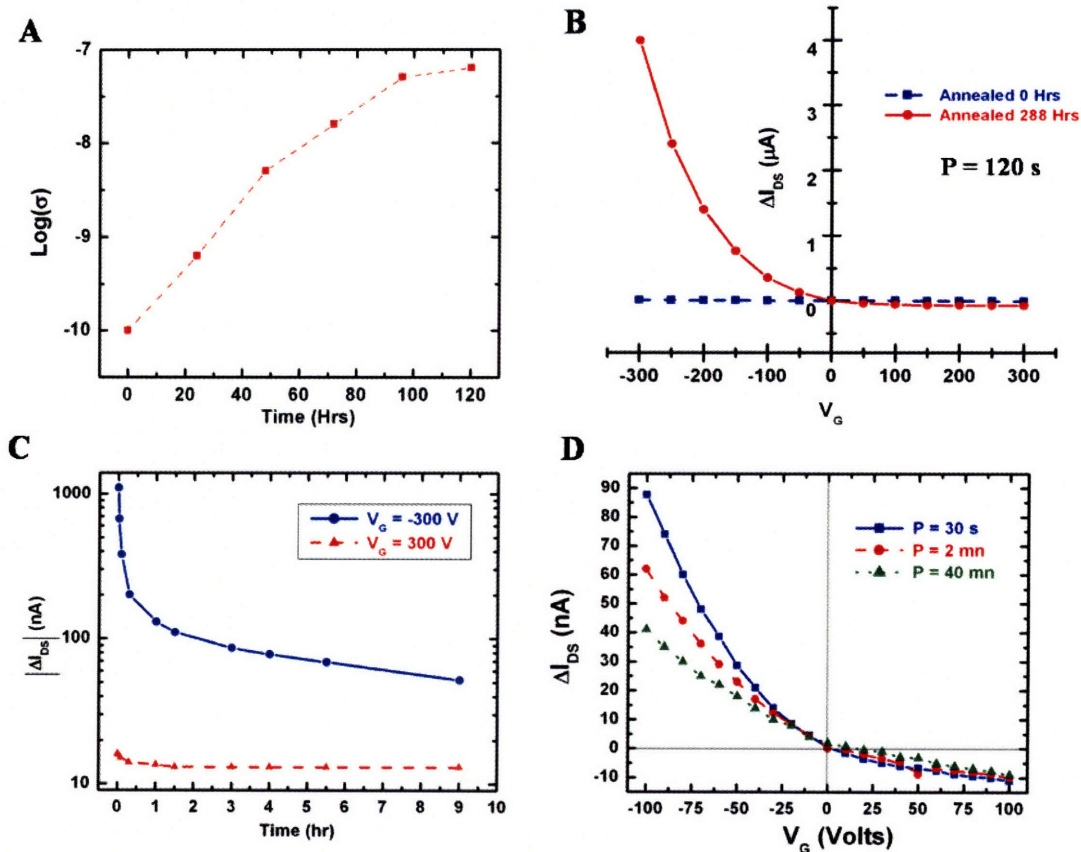
Figure V-8: (a) Change of conductivity of AST thin-film with annealing time. (b) Change of drain-to-source current for a gate voltage applied with a period of 120 s for unannealed (blue) and annealed fiber (red). (c) Decay of drain-to-source current over time when a step voltage of -300V (blue) and +300V (red) is applied to the gate. (d) Change of drain-to-source current for a gate voltage applied with different periods for an annealed fiber.

we can make a first evaluation that the density of localized states has dropped by more than two orders of magnitude. However, we have also observed that this behavior is transient as shown in Figure V-8(c,d), as the period of the gate voltage modulation is increased, the field effect is less pronounced. Same thing when a step gate voltage is applied: the current between the source and the drain increases drastically (when the gate voltage is negative) before decreasing slowly over time to its original value (when $V_G = 0$), sometimes over several hours. This is in total agreement again with the paper of Frye and Adler [69], who explain this transient behavior studying the kinetic structural changes from donor-like to acceptor-like defects. We will come back to this in our discussion in the next section.

Yet, we have been able, using proper annealing conditions, to obtain fiber device exhibiting a steady state field effect. Figure V-9(a) shows the decay over time of the absolute value of the drain-to-source current (since it is negative when a positive voltage is applied) $|\Delta I_{DS}|$, when -300V and +300V are applied to the gate. A 10V potential was applied between the drain and the source and the dark current, when $V_G = 0V$, was 4 nA. After a very long period of time, up to 36 hours, the change of current slowly converges to 16nA and -4 nA respectively, illustrating the strong asymmetry when holes or electrons are injected inside the material. Figure V-9(b) shows the I-V curves after steady state is reached for the three gate voltages -300V, 0V and +300V. It seems that a pinch-off type of behavior, even though we are in an accumulation regime, is reached at +300V, although a small leakage current through the polymer is responsible for the negative current obtained.

These compelling results are a corner stone towards a new generation of fibers with complex functionalities. They demonstrate our ability to integrate, using a simple and inexpensive fabrication technique, over tens of meters of fibers length materials with *crystalline*-like behavior. We discuss in the next session a few more findings and future work we envision.

V.4.c. Discussion

To have a complete understanding of what happens as we anneal the fiber, a complete study with several fibers having different structures (especially changing the insulator thickness) and glass composition is necessary. Temperature effects should be analyzed as well as photo-response, both spectral as well as regarding time response. Here we discuss some preliminary results on the time dependence of the field effect observed in the fiber to give a physical intuition of what might be happening as the fibers are annealed. Transient behaviors indeed give some insight about the field effect mechanism in materials with a high density of localized states as explained thoroughly in [69]. Following their model, three types of single step transitions occurring via charge transfer and/or atomic relaxation are responsible for the transient behavior. They are summarized by the following diagram:
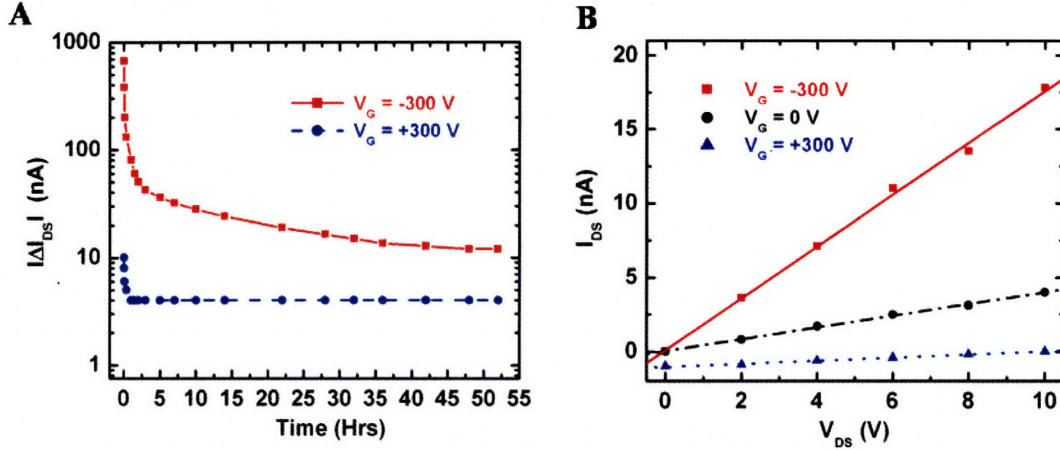
Figure V-9: (a) Decay with time of drain-to-source current change upon the appliance of a gate voltage of -300V (red) and +300V (blue). (b) I-V curve of drain-to-source current for an applied gate voltage of -300V (red), 0V (black) and +300V (blue).

$$N_D^+ \leftrightarrow N_D^0 \leftrightarrow N_A^0 \leftrightarrow N_A^- \qquad \text{(V-9)}$$

In other words, an electron can be captured (or a hole released and vice versa) to neutralize a donor-like defect, a structural change can occur to transform a donor-like to an acceptor-like defect, and an electron can be captured (or a hole released, and vice versa) to ionize an acceptor-like defect. It is reasonable to assess that the slow process responsible for the long decay times is the structural change $N_D^0 \leftrightarrow N_A^0$. Indeed the other processes involve the capture of free charges and the release of trapped charges that are typically faster than the time constants of hours the field effect measurements exhibit. The rate to first order from mass-action consideration is given by:

$$R = \frac{1}{\tau}\left(N_A^0 - e^{-W/kT} N_D^0\right) \qquad \text{(V-10)}$$

where τ is the relaxation time and we have considered W positive. What happens when a negative voltage is applied to the gate is then the following: Holes are injected inside the semiconductor and neutralize ionized acceptors. Neutral acceptors become in excess and relax into neutral donors, which in turn capture holes. This process has a time constant of $\tau_1 = \tau/2$ (the factor 2 kicks in due to the two holes transfer process). The excess of charged donors resulting increase the density of charges and hence reduce the screening length. The bands in the bulk material flatten and holes captured deeper inside are

reemitted to move towards the surface. In this process, neutral donors in turn transform into neutral acceptor that give up a hole and become negatively charged again. This process has a time constant τ_2 as indicated below. The two holes emitted in this process will become trapped a gain, converting acceptors to donors and so on.

Hence, the overall process has two decay mechanisms at early and later times, well fitted by first orders exponential decays where:

at early times:
$$\frac{d(\Delta I_{DS})}{dt} + \frac{1}{\tau_1} \Delta I_{DS} = 0$$

at later times:
$$\frac{d(\Delta I_{DS})}{dt} + \frac{1}{\tau_2} \Delta I_{DS} = 0$$

where $\tau_1 = \frac{\tau}{2}$ and $\frac{\tau_1}{\tau_2} = 2e^{-W/kT}$. To get insights on what happens with the density of states as we anneal the fiber, we performed field effect measurements on fibers annealed for different times. Especially we recorded the transient behavior over time using a labview interface with a Keithley 6487 picometer and were able to extract the two time constants. In Table 1 we report our findings as well as the calculated energy W. We reproduced in Table 1 median results obtained on different samples annealed for a same amount of time since the results varied between samples. We attribute these fluctuations again to small difference in temperature distributions experienced during annealing and a potential non uniformity of contact between an electrode and the glass film along the fiber length. Nevertheless, intriguing observations can be made: first, as we explained, very long time constants are obtained in agreement with results reported in [67,69]. A clear pattern can be observed where the time constants get longer and the energy W is roughly constant around 0,092 ± 0,006 eV. A drastic jump of time constant and a slight increase of W occur however between the fibers annealed 240 Hrs and 288 Hrs, where steady state field effect was observed.

Evidence exists that the time constants τ_1 and τ_2, and hence τ, are activated [69]. The neutral defects lie at the bottom of a potential while a barrier energy exists between the two states. This seems intuitive since a local structural rearrangement is required for interconversion to occur. The influence of the height of this barrier on the interconversion

	Annealed 60 Hrs	Annealed 96 Hrs	Annealed 120 Hrs	Annealed 168 Hrs	Annealed 240 Hrs	Annealed 288 Hrs
τ_1 (mn)	2	3.5	5	6	9	30
τ_2 (mn)	42	70	80	100	160	770
W (eV)	0.093	0.092	0.087	0.088	0.089	0.098

Table 1: Time constants of transient field effect and corresponding measured energy W from measurements made on fibers annealed for different times.

time is very strong. Little change in energy can lead to orders of magnitude changes in time constant. The jump of time constants between the 240 and 288 Hrs of annealing time is hence not surprising with regards to these observations. A distribution of VAP could yield a wide spread of interconversion times [76]. As the film is annealed, VAP disappear as bonds are forming and atoms rearrange in their low energy crystalline form and the time constant will change accordingly. Indeed as the density of VAPs decrease, less neighboring sites are available for interconversion which leads to an increase of the barrier energy. We would also expect the energy W to increase slightly since the tendency of the matrix is to lower each site binding energy which would separate more the level of neutral donors and acceptors.

As we pointed out, the situation here is quite complex and can be sorted out by careful time-resolved measurements over wide temperature ranges. However, our initial results seem to confirm that the annealing process decreases the number of defect states inside the bandgap. Moreover, it limits their interconversion which leads to a drastic increase in time constant rendering the field effect in fiber good for real world applications. The control over the density of defect states and their relative energy is essential for the formation of practically all electronic and optoelectronic devices involving hetero-junctions. In that regard, this study is a significant step towards a new generation of fiber-based devices with even more complex functionalities.

CONCLUSION

The heart of this work consisted of the development of a novel fiber drawing technique that integrates materials with widely disparate optic and electronic properties. More specifically, the controlled processing of metallic elements inside a fiber device using a preform-to-fiber drawing technique is unprecedented. This new materials processing paradigm enabled the integration of novel electronic and optoelectronic functionalities into fiber-based devices to be used in a myriad of new applications. In particular, we demonstrated the design, fabrication, characterization and modeling of 1D distributed photodetectors. Theoretical considerations combined with a constant refinement of the drawing technique enabled the transition from solid-core to thin-film photodetecting structures, and from single thin-film to multiple thin-film structures. Our efforts have resulted in photodetecting devices with improved sensitivity and unprecedented performance such as angular and spectral resolutions. We also demonstrated the firs field effect in thermally drawn fibers thanks to the appropriate combination of solid-core and thin-film structures in a single fiber.

The novel fiber structures described in this thesis have remarkable properties in their own right. Nevertheless, intriguing device applications follow not only from the ability to engineer the single-fiber features, but also from the ability to arrange these fibers into larger assemblies and woven fabrics. These are made possible thanks to both the fiber flexibility and mechanical toughness. We have demonstrated the fabrication of fiber webs capable of light detection at unprecedented level of scale and practicality. Improving the fiber structure of a single fiber can also impact significantly the performance of their assembly. This was illustrated by an improvement in the lensless imaging system envisioned using integrated fiber devices.

Multimaterial fibers have a wide range of functionalities beyond light detection. In a combined and continuing effort with Nomadics Inc., an industrial project presented briefly in this work involved the use of fiber-based devices for explosive detection. The proof-of-principle that we demonstrated here could lead to a light-weight, practical, far-reaching and highly sensitive explosives detector. Thermal detection and mapping have also been demonstrated using fiber meshes [20]. In [19], group members have fabricated

and characterized an optical fiber that can predict its own failure. Omniguide Inc. has licensed the patent resulting from this discovery. Many other projects on multimaterials and multifunctional fiber devices are now ongoing in the Photonic Bandgap Fibers and Devices group. In particular, efforts are underway toward developing Piezoelectric and Photovoltaic fiber devices. These could have a major impact in sensing applications and in clean energy.

This thesis work created the solid ground for a new fiber technology platform that has the potential to impact a wide range of industries. Large area electronic and optoelectronic assemblies, functional fabrics, sensors with unprecedented functionalities, clean energy are among the most intriguing. Envisioned are fibers integrating thousands of devices and capable of even more complex functionalities in logic and detection operations. Development is underway to bring these concepts and devices to a higher level of maturity.

REFERENCES

1   K.T.V. Grattan and B.T. Meggit, *Optical fiber sensor technology* (Kluwer, 2000).

2   H. S. Nalwa, *Photodetectors and Fiber Optics*, (Academic Press, 2001).

3   Sze, S. M. Semiconductor Devices: Physics and Technology 2nd edn (John Wiley, New York, 2001).

4   Sedra, A. S. & Smith, K. C. Microelectronic Circuits (Oxford Univ. Press, Oxford, 2003).

5   Chuang, S. L. Physics of Optoelectronic Devices (John Wiley, New York, 1995).

6   Sanghera, J. S. & Aggarwal, I. D. (eds) Infrared Fiber Optics (CRC Press, New York, 1998).

7   Harrington, J. A. A review of IR transmitting, hollow waveguides. Fiber Integrated Opt. 19, pp 211–227 (2000).

8   Katagiri, T., Matsuura, Y. & Miyagi, M. Metal-covered photonic bandgap multilayer for infrared hollow waveguides. Appl. Opt. 41, pp 7603–7606 (2002).

9   Large, M. et al. Microstructured optical fibers:Why use polymers? Proc. 29th Eur. Conf. on Opt. Comm.(ECOC'03 Rimini), 1014–1017 (2003); available at khttp://www.oftc.usyd.edu.au/?section¼fibre&fibre¼mpof#2l

10 Broeng, J., Mogilevstev, D., Barkou, S. E. & Bjarklev, A. Photonic crystal fibers: A new class of optical waveguides. Opt. Fiber Technol. 5, pp 305–330 (1999).

11 Eggleton, B. J., Kerbage, C.,Westbrook, P. S.,Windeler, R. S. & Hale, A. Microstructured optical fiber devices. Opt. Express 9, pp 698–713 (2001).

12 van Eijkelenborg, M. A. et al. *Microstructured polymer optical fiber*. Opt. Express 9, pp 319–327 (2001).

13 Allan, D. C. et al. *in Photonic Crystal and Light Localisation in the 21st Century* (ed. Soukoulis, C. M.) 305–320 (Kluwer Academic, Dordrecht, 2001).

14 Knight, J. C. *Photonic crystal fibres*. Nature 424, 847–851 (2003).

15 Temelkuran, B., Hart, S. D., Benoit, G., Joannopoulos, J. D. & Fink, Y. *Wavelength-scalable hollow optical fibres with large photonic bandgaps for CO2 laser transmission*. Nature 420, pp 650–653 (2002).

16   S. D. Hart, G. R. Maskaly, B. Temelkuran, P. H. Prideaux, J. D. Joannopoulos, and Y. Fink, *External reflection from omnidirectional dielectric mirror fibers*, Science 296, 511-513 (2002).

17   M. Bayindir, F. Sorin, A. F. Abouraddy, J. Viens, S. D. Hart, J. D. Joannopoulos, and Y. Fink, *Metal-insulator-semiconductor optoelectronic fibers*, Nature 431, 826 (2004).

18   M. Bayindir, A. F. Abouraddy, F. Sorin, J. D. Joannopoulos, and Y. Fink, *Fiber photodetectors codrawn from conducting, semiconducting and insulating materials*, Opt. and Photon. News 15, 24 (2004).

19   M. Bayindir, O. Shapira, D. Saygin-Hinczewski, J. Viens, A. F. Abouraddy, J. D. Joannopoulos, and Y. Fink, *Integrated fibres for self-monitored optical transport*, Nature Materials (November, 2005).

20   M. Bayindir, A. F. Abouraddy, J. D. Joannopoulos, and Y. Fink, *Thermal-sensing mesoscopic fiber devices by composite-material processing*, Advanced Materials (October, 2005).

21   Y. Fink, J. N. Winn, S. Fan, C. Chen, J. Michel, J. D. Joannopoulos, E. L. Thomas, *A Dielectric omnidirectional reflector*, Science 282, 1979 (1998).

22   Yosomiya, R., Morimoto, K., Nakajima, A., Ikada, Y. & Suzuki, T. *Adhesion and bonding in composites* (Marcel Dekker, New York, 1990).

23   Z. U. Borisova , *Glassy semiconductors,* (Plenum Press, NY 1981)

24   Hilton, A.R. *Optical Properties of Chalcogenide Glasses*. J. Non-Cryst. Solids 2, 28 (1970).

25   King, W.A., Clare, A.G. & Lacourse, W.C. *Laboratory preparation of highly pure As$_2$Se$_3$ Glass,* J. Non-Cryst. Solids 181, 231 (1995).

26   B. Zhang,. D.Q. Zhao, M.X. Pan, W.H. Wang and A.L. Greer, *Amorphous Metallic Plastic*, Phys. Rev. Lett. 94, 205502 (2005).

27   MRS Bulletin, August 2007, Volume 32, No. 8.

28   N. F. Mott, *Electronic processes in non-crystalline materials,* (Oxford University Press, 1979)

29   D. Adler and E. J. Yoffa, *Electronic structure of amorphous semiconductors,* Phys. Rev. Lett. 36 (20) pp. 1197-1200. (1976)

30 A. F. Abouraddy, O. Shapira, M. Bayindir, J. Arnold, F. Sorin, D. Saygin-Hinczewski, J. D. Joannopoulos, and Y. Fink, *Large-scale Optical-field measurements with geometric fibre constructs*, Nature Materials 5 pp. 532-536 (2006).

31 Bayindir, A. F. Abouraddy, O. Shapira, J. Viens, D. Saygin-Hinczewski F. Sorin, J. Arnold, J. D. Joannopoulos, Y. Fink, IEEE J. Sel. Top. Quantum Electron. 2006, 12 (6), 1202.

32 A. F. Abouraddy, M. Bayindir, G. Benoit, S. D. Hart, K. Kuriki, N. Orf, O. Shapira, F. Sorin, B. Temelkuran, Y. Fink, Nature Materials 6 pp. 336-347 (2007)

33 A. C. Kak, and M. Slaney, "Principles of Computerized Tomographic Imaging" , IEEE Press, (1988).

34 H. Stark, "Image Recovery: Theory and applications", Academic Press (1987)

35 J. R. Fienup, "Phase-retrieval algorithms for a complicated optical system", Appl. Opt. 32, 1737-1746 (1993).

36 J. R. Fienup, "Phase retrieval for undersampled broadband images", J. Opt. Soc. Am. A 16, 1831-1837 (1999).

37 J. Miao, D. Sayre, and H. N. Chapman, "Phase Retrieval from the Magnitude of the Fourier Transforms of nonperiodic objects", J. Opt. Soc. Am. A, 15(6) 1662-1669 (1998)

38 R. H. T. Bates, and D. G. H. Tan, "Fourier Phase Retrieval when the Image is Complex", SPIE Vol. 558 Inverse Optics II, 54-59 (1985)

39 M. H. Hayes, "The Reconstruction of a Multidimensional Sequence from the Phase or Magnitude of its Fourier Transform", IEEE Trans. Acous. Speech, and Sig. Proc., ASSP-30(2) 140-154 (1982)

40 F. Sorin et al., Advanced Materials, in Press (2007).

41 E. Rosencher, B. Vinter, *Optoelectronics*, (Cambridge University Press 2002).

42 R. H. Kingston, *Detection of Optical and Infrared Radiation* (Springer 1978).

43 A. M. Andriesh, M. S. Iovu and S. D. Shutov, *Optical and Photoelectricacl properties of chalcogenide glasses*, Chalcogenide Glass II, Ch 4, 115-200 (Elsevier, 2004)

44   J. M. Marshall, *Carrier diffusion in amorphous semiconductors*, Rep. Prog. Phys. 46, pp 1235-1282 (1983)

45   D. Ritter, E. Zeldov, and K. Weiser, *Ambipolar transport in amorphous semiconductors in the lifetime and relaxation-time regimes investigated by the steady-state photocarrier grating technique*, Phys. Rev. B 38, 8296–8304 (1988)

46   S. Reynolds, C. Maine, M.J. Rose, *Noise and Modulated Photocurrents in amorphous semiconductors*, J. Non-Crust. Solids 227-230 pp. 233-237 (1998).

47   Orenstein J. and Kastner M., Time-resolved optical absorption and mobility of localized charge carriers in a-As2Se3, Phys. Rev. Lett, 43 (2) pp 161-165 (1979).

48   M. S. Iovu, S.D> Shutov, V. I. Arkhipov, S. Z. Rebeja, M. G. Bulgaru and E. P. Colomeyko, *Photocurrent transients in amorphous chalcogenides: evidence for trap-controlled recombination*, IEEE, Semiconductor Conference, 1997, 1, pp 53-56 (1997)

49   A. M. Andriesh, M. S. Iovu and S. D. Shutov, *Optical and Photoelectricacl properties of chalcogenide glasses*, Chalcogenide Glass II, Ch 4, 115-200 (Elsevier, 2004)

50   D. Monroe and M. A. Kastner, *Exactly exponential band tail in a glassy semiconductor*, Phys. Rev. B 33 (12) pp. 8881-8884 (1986)

51   Orenstein J. and Kastner M., *Photocurrent Transient Spectroscopy: Measurment of the density of localized states in a-As$_2$Se$_3$*, Phys. Rev. Lett, 46 (21) pp 1421-1424 (1981).

52   Hammam M., G. J. Adriesenssens and W. Grevendonk, *Steady-state photoconductivity in amorphous arsenic selenide compounds*, J. Phys. C.: Solid State Phys., 18 pp 2151-2160 (1985)

53   G. J. Adriaenssens, S. D. Baranovskii, W. Fuhs, Ö. Öktü, *Photoconductivity response time in amorphous semiconductors* Phys. Rev. B 51 (15), 9661–9667 (1995).

54   F. W. Schmidlin, Theory of trap-controlled transient photoconduction, Phys. Rev. B, 16 (6) pp 2362-2385 (1977)

55   A. Schulte, C. Rivero, K. Richardson, K. Turcotte, V. Hamel, A. Villeneuve, T. Galsitan, R. Vallee, Opt. Commun. 2001, 198, 125.

56   Ston R., Vlcek Mir., Jain H., *Structure and photoinduced changes in bulk and filmsof As-Ge-S system*, J. Non-Cryst. Solids, 326&327 pp 220–225 (2003).

57   D.V. Hinkley, Biometrika 56 (3), 635-639 (1969).

58   J. N. Cederquist, J. R. Fienup, J. C. Marron, and R. G. Paxman, "Phase retrieval from experimental far-field speckle data", Opt. Lett. 13, 619-621 (1988).

59   R. H. T. Bates, "Fourier phase problems are uniquely soluble in more then one dimension. I: Underlying theory", Optik 61, 247-262 (1982).

60   F. Sorin et al., Manuscript to be submitted (2008).

61   H. Fritzsche and S.R. Ovshinsky, J. Non-Cryst. Solids 2, 393 (1970)

62   R.F. Egerton, Appl. Phys. Lett. 19, 203 (1971)

63   A.W. Levy, M. Green and W. Gee, J. Phys. C 7, 352 (1974)

64   P. A. Tick and J.h.P. Watson, J. Non-Cryst. Solids 13, 229 (1973)

65   J.M. Marshall and A.E. Owen, Philos. Mag. 33, 457 (1976)

66   E. Mahan and R.H. Bube, J. Non-Cryst. Solids 24, 29 (1977)

67   N.A. Radjy and M. Green, Philos. Mag. 41, 497 (1980)

68   Mott N. F. , Davis E. A., *Electronic processes in non-crystalline materials*, (Oxford University Press 1979).

69   R. C. Frye and D. Adler, *Field effect in chalcogenide glasses*, Phys. Rev. B 24 (10), pp 5812-5834 (1981)

70   P.W. Anderson, Phys. Rev. Lett. 34, 953 (1975)

71   R.A. Street and N.F. Mott Phys. Rev. Lett. 35, 1293 (1975)

72   Mott N. F. , Davis E. A and R.A. Street, Philos. Lett. 32, 961 (1975)

73   M. Kastner, D. Adler and H. Fritzsche, Phys. Rev. Lett. 37, 1504 (1976)

74   D. Adler, J. Non Cryst. Solids 35/36, 819 (1980)

75   D. Adler Sol. Cell 2, 199 (1980)

76   D. Adler Sol. En. Mat. 8, 53 (1982), 199 (1980)

77   K.NG Kwok, *Complete guide to semiconductors devices*, (Wiley, 2002)

78   S. Danto, F. Sorin et. al. To be Published.